# Decoding Skin Aging Mechanisms through Systems-Level Analysis and Modulation by Retinoic Acid

システムレベルでの解析とレチノイン酸による調節を通じた

皮膚老化メカニズムの解明

**Masatoshi Haga**

羽賀 雅俊

Department of Biological Sciences

Graduate School of Science, Osaka University

大阪大学大学院理学研究科生物科学専攻

A Dissertation Submitted for the Degree of *Doctor of Philosophy*

博士学位論文

July 2024

令和 6 年 7月

# Contents

# ABSTRACT

During aging, maintaining skin homeostasis is essential for appearance and the biological defense of the human body. In this study, I identified thrombospondin-1 (THBS1) and fibromodulin (FMOD) as positive and negative regulators, respectively, of the transforming growth factor-β1 (TGF-β1)–SMAD4 signaling axis in human skin aging, based on *in vitro* and *in vivo* omics analyses and mathematical modeling. Furthermore, I analyzed the transcription factor (TF) network involved in dermal fibroblast senescence treatment with all-*trans*-retinoic acid (ATRA). Using transcriptomic and epigenetic analyses of replication-stress (RS) induced senescent dermal fibroblasts, I identified TGF-β1 as the key upstream regulator. Bifurcation analysis revealed a binary high-/low-TGF-β1 switch, with THBS1 as the main controller. Computational simulation of the TGF-β1 signaling pathway indicated that THBS1 expression was sensitively regulated, whereas FMOD was regulated robustly, suggesting THBS1 as a controllable molecule in skin aging. Furthermore, I identified ATRA as a potent THBS1 suppressor, regulating THBS1 transcription via a network involving retinoid X receptor (RXR), SMAD, and transcriptional enhanced associate domain (TEAD). The analysis of TF activity of the RS model indicated RXR inactivation and SMAD and TEAD activation in senescent dermal fibroblasts. TEAD inhibition increased THBS1 levels. Additionally, senescent dermal fibroblasts cultured on a soft substrate markedly reduced the number of senescence-associated-β-galactosidase-positive cells by activating TEAD. Therefore, the study demonstrates the potential of combining data-driven target discovery with mathematical approaches to determine the mechanisms underlying skin aging.

# ORIGINALITY

This doctoral dissertation is based on the results and descriptions of the following papers:

1) Haga M, Okada M. Systems approaches to investigate the role of NF-κB signaling in aging. **Biochem J**. 2022;479(2):161-183. doi:10.1042/BCJ20210547
2) Haga M, Iida K, Okada M. Positive and negative feedback regulation of the TGF-β1 explains two equilibrium states in skin aging. **iScience**. 2024;27(5):109708. Published 2024 Apr 10. doi:10.1016/j.isci.2024.109708

I am preparing a submission related to section 3.2 “Identification of Potent THBS1 Suppressor and its Mechanism Toward Senescence” as follows:

3) Haga M, Okada M. Data-driven multi-omics analysis and mathematical modeling to explore skin aging targets and the retinoic acid efficacy

# 1. INTRODUCTION

## 1.1 Research topic

**Aging and Skin Aging**

Aging is a universal and unavoidable process that significantly increases the risk of diseases, such as skin cancer, by disrupting health homeostasis [1,2]. In the recent revision of the International Classification of Diseases (ICD), the global multilingual catalog of human diseases, medical conditions, and mental disorders, the World Health Organization (WHO) replaced "senility" in ICD-11 with "ageing associated decline in intrinsic capacity" to standardize disease diagnosis, reduce age discrimination, and promote better health and quality of life for elderly people [3]. Over the past century, the age structure of developed countries, such as Japan has undergone a major aging transition. In 1950, over half of Japan's population was under 25, but by 2021, this share had declined, and the proportion of those over 65 had increased significantly, forming a substantial part of the population (Figure 1.1.1) [4]. In response to the population transition to an aging society, the third phase of Health Japan 21 (2023-2035), a national health promotion movement launched by the Japanese government, defines the extension of healthy life expectancy and reduction of health disparities as the basic direction of the policy [5]. The increasing proportion of the elderly population has led to a growing awareness of healthy life expectancy, and there is a growing demand for people to live longer and healthier lives, rather than simply live longer. Promoting research on aging will help seniors live long, healthy, and independent lives by increasing their healthy life expectancy, thereby reducing medical and long-term care costs. Simulation analysis indicates reducing the need for long-term care among elderly Japanese people can reduce healthcare costs [6]. Maintaining the health of the elderly and promoting their productive participation in society through aging research will contribute to the economic stability of society. This demographic shift underscores the need for research into age-related health issues.

As age has been reported as one of the major risks for skin aging [7], demographic changes in society have increased the impact of skin aging research. Maintaining skin homeostasis during aging is vital for biological protection, as thinner and more fragile skin is more susceptible to diseases [8]. Skin aging causes loss of elasticity, increased inflammation, and reduced mechanical resistance to skin damage, ultimately resulting in elasticity change such as skin sagging and wrinkles [8]. Aging skin homeostasis is important not only from the perspective of biological defense, but also for external beauty; how other people see you is important for self-affirmation and has social and psychological significance. As skin texture, color, facial radiance, and elasticity

change with aging, these factors greatly affect how people perceive themselves [9–12]. Approaches to addressing skin aging improve mental health by increasing self-esteem and decreasing social anxiety and isolation, and they may extend healthy life expectancy by promoting preventive health behaviors [13]. Therefore, this study aims to investigate specific interventions to extend healthy life expectancy in Japan's aging society through skin aging research.

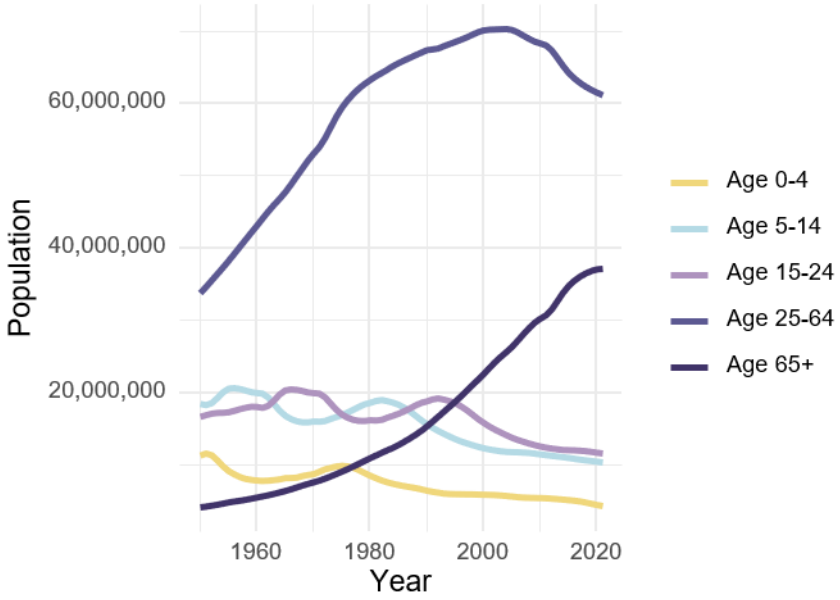


**Figure 1.1.1**: Population distribution by age group in Japan.
Illustration of the demographic shift in Japan's population from 1950 to 2021, highlighting the increasing proportion of the elderly population [4]. This demographic trend underscores the growing importance of research on aging and age-related diseases.

The skin is the largest organ of the human body exposed to the outside world; it acts as a barrier to external environments and protects against unwanted external stimuli [14]. Skin tissue mainly consists of the epidermis, dermis, and hypodermis (Figure 1.1.2). The epidermis acts as an interface with the environment as a barrier, the dermis provides structure and flexibility to the skin, and the hypodermis helps to insulate, store energy, and act as a shock absorber [15].

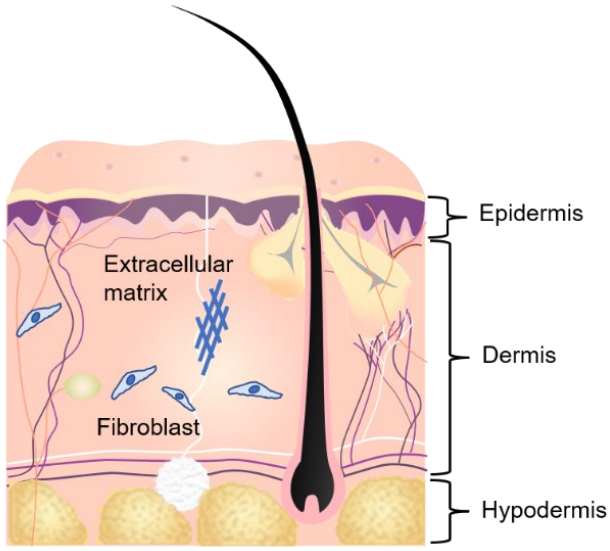


**Figure 1.1.2**: Structure of human skin tissue.

Skin mainly consists of the epidermis, dermis, and hypodermis tissue. The epidermis is composed primarily of keratinocytes and functions as a barrier to the external environment. The dermis provides elasticity to the skin through the extracellular matrix produced by dermal fibroblasts. The hypodermis is composed mainly of fat and plays a role in energy storage and shock absorption. The original of this image was obtained from TogoTV and modified (© 2016 DBCLS TogoTV, CC-BY-4.0).

Skin aging has been reported to cause both structural and functional changes. Structurally, the epidermis becomes thinner and the bonds between keratinocytes weaken [16,17]. The effects of reduced dermal fibroblast activity and changes in gene expression related to extracellular matrix (ECM) components are crucial factors in skin aging [18]. In the dermis, ECM, which are essential for maintaining the structural integrity of the skin components, such as collagen production and elastin decrease, as does the thickness and number of fibroblasts, mast cells and macrophages [16,19]. Aging also induces fragmentation and non-organization of dermal collagen fibers due to increased expression of major matrix metalloproteinase 1, leading to abnormal ECM homeostasis [20]. In certain areas, hypodermis fat is reduced, with noticeable changes in the face, shins, hands, and feet [17,21,22]. These structural changes result in the functional decline of aging skin.

Functionally, skin aging reduces the rate of epidermal, hair, and nail growth, and delays wound healing [17]. In addition, the skin's immune and inflammatory response are reduced and its resistance to infection is diminished [16,17]. The skin's barrier function is also compromised, along with its ability to retain moisture [16]. Hence, skin aging research is important not only for the aging society but also for individual biological defense.

**Cellular Senescence**

Skin aging is caused by both external factors (such as UV exposure, smoking, and environmental pollution) [23] and internal factors (such as impaired skin repair and hormonal imbalance) [24]. Specifically, seven notable risk factors for various skin aging phenotypes have been identified: age, gender, ethnicity, air pollution, nutrition, smoking, and sun exposure [7]. As hallmarks of skin aging, genomic instability and telomere attrition, epigenetic alterations and loss of proteostasis, deregulated nutrient-sensing, mitochondrial damage and dysfunction, stem cell exhaustion/dysregulation, altered intercellular communication, and cellular senescence have been identified [25].

The key internal factor in skin aging is cellular senescence [26,27], also a hallmark of aging in general [28]. Senescent cells increase with age in many mouse and human tissues, such as adipose tissue, liver, kidney, and skeletal muscle [29]. Cellular senescence was first reported in 1961 by L. Hayflick using human fibroblast cells to demonstrate the limitations of mitotic capacity with replication-stress (RS), known as the Hayflick limit [30]. Later, telomere shortening was identified as the cause of accelerated senescence under RS using retinal pigment epithelial cells and foreskin fibroblasts [31]. Currently, various stressors (e.g., replication-stress (RS), DNA double-strand breaks, oncogene activation, and reactive oxygen species (ROS)) are reported to induce cellular senescence [32].

Senescent cells are characterized by their stable and terminal growth arrest and exhibit a flat and large morphology, DNA damage, shortened telomeres, ROS production, loss of Lamin-B1, enhanced senescence-associated β-galactosidase (SA-β-gal) activity, and increased levels of cyclin-dependent kinase inhibitors p53/p21 and/or p16 [33]. The secretion of the senescence-associated secretory phenotype (SASP), consisting of inflammatory cytokines, such as interleukin (IL)-6 and IL-8, is also a well-known senescence marker [34,35]. Lamin-B1, a nuclear matrix protein, is used to quantify senescence in the skin. Immunohistochemistry of aged epidermal and dermal tissue indicated reductions in Lamin-B1 expression [36]. Reduced levels of Lamin-B1 induced by UVB radiation also indicate a relationship with cellular senescence and skin aging [37]. An increase in SA-β-gal positive cells in aging skin is one of the earliest established indicators of senescent cells in aging skin [38].

With the visualization of the accumulation of p16-expressing senescent cells *in vivo* using real-time imaging methods, research on cellular senescence due to aging has been vigorously conducted [39,40]. Moreover, the removal of p16-expressing senescent cells suppresses aging and extends the lifespan of mice, indicating the importance of cellular senescence in aging research [41,42]. The finding that senescent cell removal contributes to an extended lifespan has led to senolysis studies that selectively remove senescent cells in aging skin [43]. A combination of senolytic drugs, Dasatinib and Quercetin, selectively decreased p16 and p21 expression in human

epidermis [44]. Treatment with the senolytic drugs ABT-263 and ABT-737 selectively eliminates p16-expressing senescent dermal fibroblast cells in aged mice, increases collagen density and expression, and inhibits age-related epidermal thinning [45]. These results indicate that cellular senescence is a fundamental factor in skin aging. However, these senolytic compounds repurpose medical drugs or reagents and do not lend themselves to general topical or cosmetic use. Therefore, new approaches to targeting senescent cells are required in the industry.

Keratinocytes, which make up the epidermis, have less influence on senescence because they have a higher turnover than fibroblasts in the dermis [34]. In the dermis, skin aging results in the accumulation of senescent fibroblasts [38,46,47]. Fibroblasts orchestrate the development of a functional skin barrier through crosstalk between the dermis and epidermis [48]. Incorporating senescent fibroblasts into a 3D equivalent model of human skin can reproduce typical changes associated with skin aging [49,50]. Early or late passage fibroblasts can mimic young and aged skin, respectively; late passage fibroblasts thin the dermis and induce epidermal differentiation [49]. Another 3D skin model using oxidative stress-induced premature senescent fibroblasts caused progressive thinning of the epidermis, increasing premature senescent cells in the dermis [50]. These studies strongly suggest that regulation of fibroblast senescence is fundamental to maintaining the skin barrier and combating aging. However, a comprehensive systems-level analysis of skin aging and cellular senescence remains unclear. The identification of regulatory systems in skin fibroblast senescence will enable the identification of upstream factors in skin aging. Furthermore, elucidating mechanistic network enables us to simulate the progression of skin aging and identify potential intervention points. Thus, I utilized computational systems biology approaches toward skin aging.

**Computational Systems Biology Approaches Toward Skin Aging Research**

Aging and senescence are caused by various developmental signals and different types of stresses and are the results of a multistep process [51,52]. Although various induced *in vitro* senescent cell models [32] and *in vivo* aging animal models [53] have been reported to elucidate the complex system, an overall picture that recapitulates the cellular transmission and spatial interactions of aging is still lacking, which is necessary to understand and overcome the unfavorable effects of aging. Data-driven multi-omics approaches, such as epigenetics, bulk RNA sequencing (RNA-seq), and single-cell RNA-seq, are used to map the gene regulatory landscapes in skin aging [54–57]. RNA-seq, DNA methylation, histone methylation (histone H3 lysine 4 tri-methylation [H3K4me3] and histone H3 lysine 27 tri-methylation [H3K27me3]) from healthy skin fibroblasts of donors aged 35 to 75 years revealed an age-dependent decrease in the expression of genes involved in translation and ribosomal function [54]. An assay for transposase-accessible chromatin sequencing (ATAC-seq) and RNA-seq analyses of healthy and Hutchinson–

Gilford progeria syndrome (HGPS, a premature aging syndrome) skin fibroblasts revealed altered chromatin accessibility enriched in lamina-associated domains and HGPS-specific gene expression [55]. Single-cell RNA-seq of human skin from healthy individuals of various ages revealed the age-related change in the heterogeneity of dermal fibroblasts [56,57]. Despite these advancements, a comprehensive understanding of the regulatory networks governing these processes remains elusive.

Mathematical approaches have been used to infer skin disease modeling [58]. They have been also used to infer to skin aging phenotype such as facial wrinkles [59], length of each facial area [60], and skin barrier [61]. In terms of cellular senescence of dermal fibroblasts, RS-senescence-induced dermal fibroblasts were utilized to explain tissue heterogeneity with aging using a mathematical model of somatic mutations associated with cellular senescence [62]. A dynamical systems model was developed to model the proportion of dermal fibroblast cells in proliferating, growth-arrested, apoptotic, and senescent states during the transition from early culture to senescence by measuring senescence markers such as PDL, SA-β-gal, Ki-67, γH2AX, and TUNEL assays [63]. Despite these mathematical approaches to skin aging and senescence, most model use phenotypes of skin aging and do not mention gene regulatory networks as a biological context, making them insufficient models to actually intervene in skin aging. Furthermore, aging-related dynamic changes complicate the identification of key regulatory structures, making it difficult to understand the molecular mechanisms underlying skin aging and cellular senescence regulated by numerous genes.

Snapshot omics studies do not provide information on the underlying mechanistic regulatory structures; only the correlations between genes based on their expressions can be obtained. From these static datasets, we can construct only mathematical models (e.g., regression models [64]) based on the probability of correlation between genes (Figure 1.1.3A) [65]. In contrast, time-course omics data on skin aging, along with biological knowledge, show a directed graph between the gene regulatory network and the possible activity dynamics of each gene [65]. By integrating these data with mathematical models and performing numerical simulations, we can predict the mechanistic structure of biological systems and even manipulate them (Figure 1.1.3B) [65]. Here, I propose the integration of omics and mathematical modeling to offer a potential solution to deepen our understanding of the key mechanisms underlying skin aging regulated by genetic and environmental factors. Mathematical models have been used to represent human disease as a gene regulatory networks and stratify patients, identify key regulators, and predict drug targets [66–68]. As the use of animals in skin cosmetic research is prohibited in the industry [69], insights from simulations with mathematical models are important to studying skin aging.

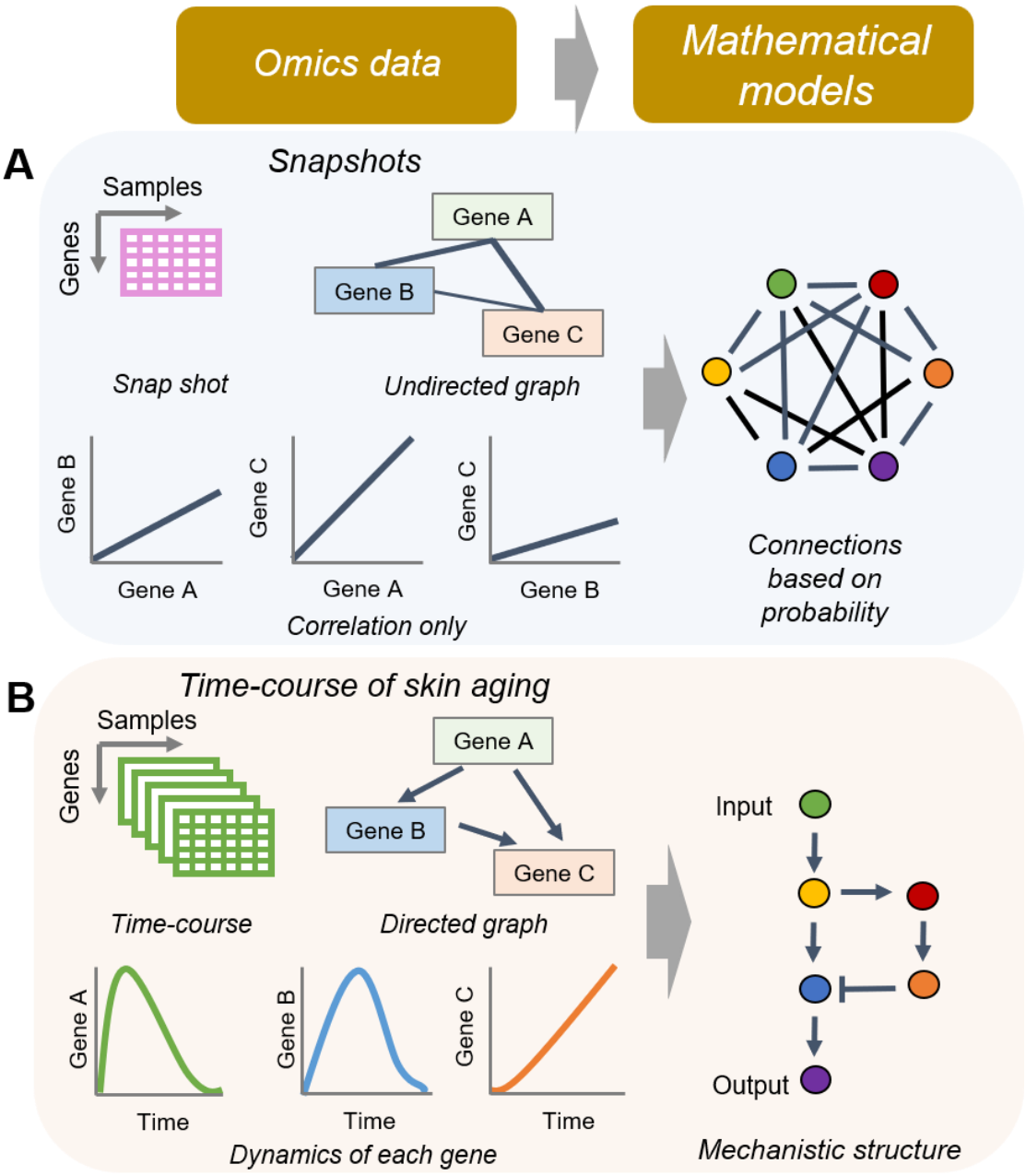


**Figure 1.1.3**: Differences between snapshot and time-course omics analysis [65].

A) Snapshot omics studies do not provide information on the underlying regulatory mechanisms; they only provide information regarding the correlations between genes. For these datasets, we can construct only mathematical models based on the probability of correlation among genes.

B) Time-course skin aging omics show a directed graph of the gene regulatory network and the dynamics of each gene. By integrating these data with mathematical models, mechanisms of biological functions can be elucidated.

Dynamic behaviors obtained from a mathematical simulation can also provide important insights into biological functions *in silico*, elucidating sensitivity and robustness of regulatory mechanisms and filling the gap between experimentally observable data and theoretical regulatory principles [70,71]. Biological systems can be represented using several networks, such as the ordinary differential equation (ODE) model [72]. ODE models are most commonly used to quantitatively understand biological systems [73,74]. The ODE model is said to be "ordinary" because it contains only one independent variable, which is basically time. It assumes that species are present in well-mixed compartments and that concentrations can be continuous [72], which generally makes the ODE model unsuitable for representing processes such as diffusion, spatial heterogeneity, and stochasticity [75]. Each variable represents the concentration of one component (e.g., gene, protein), and how it changes over time depends on the initial value of each variable, the concentrations of other variables, and fixed kinetic parameters. Hence, if we attempt to represent the biological system with the ODE model, we need to estimate the kinetic parameters that correspond to the time-series data.

Notably, skin aging is a physiological phenomenon that progresses over several decades. By contrast, cellular senescence can be induced by a variety of stimuli in a rather short time period [32]. In other words, time-series information on signal transduction is important for phenomena that change rapidly, such as cellular senescence, and a model that allows a structural understanding of signaling pathways, such as the ODE model, is considered suitable. Thus, I selected the ODE model as an appropriate model for my dataset to elucidate the system behind skin aging and senescence. Furthermore, the identification of regulatory systems in skin fibroblast senescence will enable the identification of upstream factors in skin aging. In this dissertation, by integrating omics and mathematical approaches, I identified important genes from the numerous genes and how they should be targeted to counteract skin aging.

## 1.2 Objective

In this dissertation, I hypothesize that specific genes and signaling pathways are crucial for elucidating the molecular mechanisms of skin aging and dermal fibroblast senescence. Therefore, the main objective is to address the challenges posed by an aging society by focusing on the regulatory mechanisms underlying skin aging and dermal fibroblast senescence. This study aims to:

1. Identify key molecular targets and pathways involved in skin aging and dermal fibroblast senescence through multi-omics analysis and mathematical modeling. This will provide a detailed understanding of the gene regulatory networks and signaling pathways that drive skin aging.
2. Develop and validate computational models to predict the dynamics of skin aging and dermal fibroblast senescence at the systems level. These models will integrate multi-omics data and time-course information to simulate the progression of skin aging and identify potential intervention points.
3. Investigate and identify natural compounds that can modulate key molecular targets to mitigate skin aging and dermal fibroblast senescence. This includes elucidating the mechanisms of action of these compounds through omics approaches, thereby offering potential therapeutic strategies for age-related skin conditions.

This research is structured into two main sections: the first focuses on the multi-omics analysis and mathematical modeling of skin aging, and the second explores the identification of natural compounds for therapeutic applications and their mode of action through an omics approach.

## 1.3 Contribution of this dissertation

The contributions of this dissertation are multifaceted and address significant gaps in the understanding of skin aging and cellular senescence. Specifically, this dissertation makes the following contributions:

1. Elucidation of Transcriptional Regulatory Mechanisms:
   This research elucidates the transcriptional regulatory mechanisms underlying dermal fibroblast senescence through multi-omics analysis of *in vitro* and *in vivo* data and mathematical modeling (Figure 1.3.1A). By integrating RNA-seq, chromatin immunoprecipitation (ChIP)-seq for H3K27Ac modifications, and ATAC-seq data from RS-induced senescent human dermal fibroblasts, key molecular targets and pathways, such as transforming growth factor β1 (TGF-β1), thrombospondin-1 (THBS1), and fibromodulin (FMOD), were identified. This provides a deeper understanding of the gene regulatory networks involved in skin aging.
2. Development of Predictive Computational Models:
   The dissertation develops and validates computational models to predict the dynamics of skin aging at the systems level. These models integrate multi-omics data and time-course information, allowing for the simulation of skin aging progression and identification of potential intervention points. This approach enhances the predictive power and utility of computational models in aging research.
3. Integration of Omics and Mathematical Modeling:
   This dissertation demonstrates the integration of omics data with mathematical modeling to offer a comprehensive understanding of the regulatory networks governing skin aging and senescence. This integrated approach not only advances the field of aging research but also provides a robust framework for studying other complex biological processes.
4. Identification and Mechanistic Elucidation of Natural Compounds:
   Through omics approaches, this research identifies natural compounds that can modulate key molecular targets to mitigate skin aging (Figure 1.3.1B). Specifically, all-*trans*-retinoic acid (ATRA) was found to effectively suppress THBS1 through nuclear transcriptional regulation involving the retinoid X receptor (RXR)/SMAD/transcriptional enhanced associate domain (TEAD) transcription factor network. This finding provides valuable insights for the development of therapeutic strategies for age-related skin conditions.

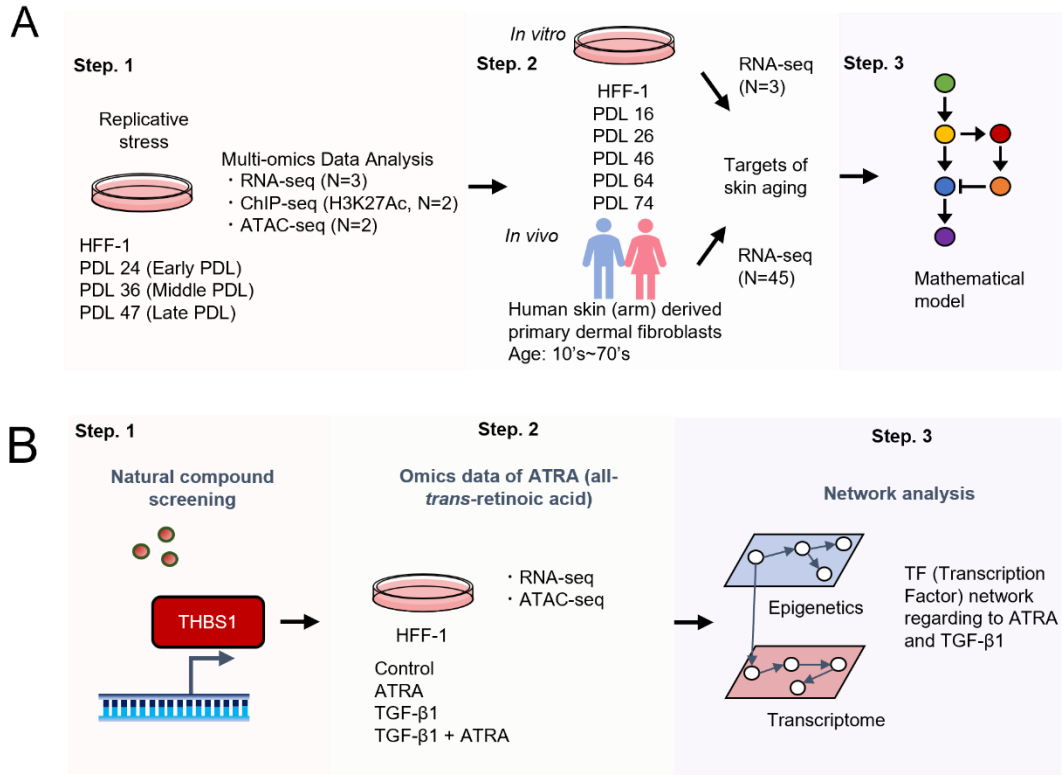


**Figure 1.3.1**: Workflow in this dissertation.

A) Workflow of skin aging and senescence analyses [76]. In the first step, replication-stress (RS) was induced by passage culturing using HFF-1 cells to prepare each population doubling level (PDL) and generate data on RNA sequencing (RNA-seq), assay for transposase-accessible chromatin sequencing (ATAC-seq), and chromatin immunoprecipitation sequencing (ChIP-seq) with an H3K27Ac antibody. In the second step, two independent public RNA-seq datasets were analyzed, one *in vitro* [77] and another *in vivo* [78]. In the third step, I constructed a mathematical model based on the multi-omics analysis and *in vitro* experimental results.

B) Workflow to investigate the potential of all-*trans*-retinoic acid (ATRA). In the first step, compound screening for THBS1 downregulation was performed. In the second step, I additionally generated RNA-seq and ATAC-seq data for ATRA with or without TGF-β1. In the third step, I elucidated the transcription factor (TF) network regarding ATRA and TGF-β1.

Through omics analysis, I found that TGF-β1 is the most enriched upstream regulator of senescence-related genes [76]. Among TGF-β-related genes, I found THBS1 and FMOD to be highly correlated with PDL or age both *in vitro* and *in vivo*. THBS1 is known to activate the latent form of TGF-β1 [79], while FMOD binds to TGF-β1 and inhibits its binding to the TGF-βR

receptor [80–82]. Using inhibitor and knockdown (KD) assays, I elucidated the signaling network for THBS1 and FMOD production. My mathematical modeling approach and bifurcation analysis revealed a regulatory network mechanism involving TGF-β1, THBS1, and FMOD in skin aging. Bifurcation analysis revealed a binary high-/low-TGF-β1 switch, with THBS1 as the primary controller. My computational simulation of the TGF-β1 signaling pathway indicated that THBS1 expression was sensitively regulated, whereas FMOD was regulated robustly, suggesting that THBS1 is a critical target of skin aging.

Combining omics and *in vitro* experiments, I found ATRA to be an effective natural compound exhibiting a mutual inhibitory relationship with SMAD signaling, involving the RXR/SMAD/TEAD TF network. Moreover, I found that TEAD, a TF enriched in senescence-associated chromatin regions and increased by ATRA, inhibits cellular senescence. Importantly, I found that senescent human dermal fibroblasts grown on a soft substrate significantly decreased the number of SA-β-gal-positive cells through the involvement of TEAD activity. My findings provide valuable insights into the potential therapeutic targets for age-related skin issues and highlight the importance of the TGF-β and Hippo signaling pathways in regulating skin aging and cellular senescence.

The findings of this dissertation are expected to provide a deeper understanding of the molecular mechanisms underlying skin aging, particularly the role of cellular senescence and the regulatory networks involved. Identifying key regulatory genes and pathways will contribute to the development of targeted therapeutic strategies. Integrating omics data with computational models offers a novel approach to studying complex biological processes, potentially leading to breakthroughs in the treatment and prevention of age-related skin conditions. This research could also inform the development of new cosmetic and medical products aimed at improving skin health and appearance.

# 2. MATERIALS AND METHODS

## 2.1 Material Details

See the KEY RESOURSE TABLE in Section 6 for the detailed information on materials used in this study.

## 2.2 Experimental Model and Study Participant Details

***Cell lines***

HFF-1 and BJ cells, human dermal fibroblasts derived from the normal foreskin tissue of neonatal males, were purchased from the American Type Culture Collection (ATCC). HFF-1 and BJ cells were maintained in Dulbecco's modified Eagle's medium (DMEM, ATCC) supplemented with 10% fetal bovine serum (FBS, Corning) and 1% antibiotic–antimycotic (Thermo Fisher Scientific) as described previously [76]. Unless otherwise noted, the population doubling level (PDL) of HFF-1 cells in the following experiments was kept at approximately 24, and that for BJ cells was approximately 36, which correspond with young cells. In the experiments, the cells were serum-starved with 0.1% FBS and tested under uniform 2% FBS conditions during stimulation. All cell lines were maintained at 37°C in a humidified atmosphere with 5% $CO_2$.

***Human dermal tissues***

Human full-thickness dermal tissues were purchased from Biopredic International via KAC and stored frozen at −20°C as described previously [76]. Skin samples were anonymized, and informed consent was obtained from all participants (see Table 2.2.1 for donor list). This study using human tissue samples was approved by the Ethics Committee of the Institute for Protein Research, Osaka University (clearance no. 2021-2).

**Table 2.2.1**: Detailed information on donors used to confirm protein expression in human dermal tissues.

| Donor ID | Age (years) | Part | Gender | Race | Frozen time (Count) | Body mass index |
|---|---|---|---|---|---|---|
| #1 | 23 | Breast | Female | Caucasian | 1 | 23 |
| #2 | 27 | Abdominal | Female | Caucasian | 1 | 24 |
| #3 | 31 | Breast | Female | Caucasian | 1 | 31 |
| #4 | 46 | Abdominal | Female | Caucasian | 1 | 21 |

| | | | | | | |
|---|---|---|---|---|---|---|
| #5 | 61 | Breast | Female | Caucasian | 1 | 29 |
| #6 | 63 | Abdominal | Female | Caucasian | 1 | 28 |

## 2.3 Resource Availability

***Data and Code Availability***

The sequence data regarding to replication-stress (RS) and TGF-β1 treatment have been deposited in the DNA Data Bank of Japan (DDBJ) and is available under accession number PRJDB15707 (Submission: DRA016119 and DRA017188). As for the sequence data regarding to all-*trans*-retinoic acid (ATRA), I am in the process of preparing a submission. The code for bioinformatics analysis and mathematical modeling for the section 3.1 "Identification of Skin Aging Target via Omics Analyses" is available on GitHub (https://github.com/okadalabipr/Haga2023).

## 2.4 Method Details

***Induction of RS in Dermal Fibroblasts***

RS was induced by passaging of HFF-1 and BJ cells. Briefly, cells were seeded in a cell culture flask and grown on DMEM supplemented with 10% FBS until reaching a sub-confluent condition as described previously [76]. Experiments were performed in triplicate flasks. After removing the medium, washing with PBS, and detaching using trypsin/EDTA (ATCC), cells were frozen in BAMBANKER® solution (NIPPON Genetics) at −80°C in a BICELL container (Nihon Freezer) and stored under liquid nitrogen. The PDL for each collection was calculated as follows: n = 3.32 (log A – log B) + X (n: final PDL of the cell line, A: yield of harvested cells, B: count of seeded cells, and X: initial PDL of the seeded cell population).

***Sample Preparation for RNA-seq and Genomic Alignment***

HFF-1 cells (PDL 24, PDL 36, and PDL 47) were used to prepare RNA sequencing (RNA-seq) libraries as described previously [76]. Briefly, each PDL was seeded in 6-well plates at 200,000 cells/well, treated with either control (DMEM with vehicle supplemented with 2% FBS) or 4 ng/mL TGF-β1 (R&D Systems), and total RNA (three wells per sample) was harvested after 48 h using a NucleoSpin RNA kit (Macherey-Nagel GmbH & Co.).

For treatment with ATRA, HFF-1 cells (PDL 24) were seeded in 6-well plates at 200,000 cells/well, serum-starved with 0.1% FBS for 24 h, and treated with 0.1% dimethyl sulfoxide (DMSO) or 5 μM ATRA (Selleck) in 0.1% FBS DMEM for 1 h before treatment. After the pretreatment, the cells were treated with either control (DMEM with 2% FBS and 0.1% DMSO vehicle), 4 ng/mL TGF-β1, or 5 μM ATRA with or without 4 ng/mL TGF-β1, and total RNA (three

wells per sample) was harvested after 48 h using the NucleoSpin RNA kit (Macherey-Nagel GmbH & Co.).

The quality of the total RNA was evaluated using a 2100 Bioanalyzer (Agilent), and RNA samples with RNA integrity > 9.0 were used for library preparation. cDNA libraries were prepared using a NEBNext® Poly(A) mRNA Magnetic Isolation Module (New England Biolabs) for PolyA selection and NEBNext® Ultra™ ll Directional RNA Library Prep Kit (New England Biolabs). Samples were prepared according to the manufacturer's protocol. The RNA-seq data were generated as paired-end 150 base reads on the NovaSeq 6000 (Illumina). The expression of specific genes was validated using qRT-PCR.

***Sequence Alignment for RNA-seq***

All RNA-seq data, including public RNA-seq data, were trimmed using Trim Galore! version 0.6.6 and aligned to human reference genome GRCh38 using hisat2 version 2.2.1 as described previously [76]. Mapped reads were extracted using samtools version 1.9 and a read count matrix was created using gene annotation (GRCh38.p13) with Subread version 2.0.1 for downstream analysis.

***Sample Preparation for Chromatin Immunoprecipitation Sequencing (ChIP-seq) and Sequence Alignment***

HFF-1 cells (PDL 24, PDL 36, and PDL 47) were used to prepare ChIP-seq libraries as described previously [76]. Briefly, the cells for each PDL were seeded in a 145-mm dishes at a density of 4,000,000 cells per dish. After 48 h of incubation, the cells were collected using the SimpleChIP Enzymatic Chromatin IP kit (9003, Cell Signaling Technology [CST]) to obtain the sheared chromatin. Briefly, two dishes per sample were fixed with fresh 1% formaldehyde (28908, Thermo Fisher Scientific) for 5 min. The cells were subjected to treatment with a micrococcal nuclease at 37°C for 20 min and the M220 Focused ultrasonicator (Covaris) for 10 min to obtain the chromatin in 150–900-bp DNA/protein fragments. Next, the H3K27Ac antibody (ab177178, Abcam) and the iDeal ChIP-seq kit for histones (Diagenode) were used to obtain ChIP-DNA. Using the SX-8G (Diagenode) platform, 2 μg of the anti-H3K27Ac antibody was incubated with 10 μL DiaMag ProteinA-coated magnetic beads for 3 h, and an IP reaction was performed for 12 h. Decross-linking was performed using 5 M NaCl and Proteinase K (Thermo Fisher Scientific) at 60°C for 4 h. ChIP-DNA was purified using MinElute® PCR Purification Kit (Qiagen). ChIP-seq libraries were prepared using NEBNext® Ultra II DNA Library Prep Kit for Illumina (New England Biolabs). All samples were prepared according to the manufacturer's protocol. ChIP-seq data were generated as paired-end 150-base reads on the NovaSeq 6000 (Illumina).

All ChIP-seq data were analyzed using the nfcore/chipseq pipeline version 1.2.2 with "nextflow

run nf-core/chipseq -r 1.2.2 -profile singularity –input samplesheet_ChIP.csv –genome GRCh38 –save_reference –max_cpus 16 –max_memory 256.GB." Briefly, reads were trimmed using Trim Galore! And aligned against the GRCh38 reference genome using BWA. MACS2 was used for broadPeak calling. Consensus peak sets across all samples were created using BEDTools version 2.30.0. The counts for consensus peaks were generated using FeatureCounts and differential chromatin accessibility was analyzed using DESeq2 version 1.36.0. For more details, see the nf-core/chipseq pipeline (https://nf-co.re/chipseq/1.2.2).

***Sample Preparation for Assay for Transposase-Accessible Chromatin Sequencing (ATAC-seq) and Sequence Alignment***

HFF-1 cells (PDL 24, PDL 36, and PDL 47) were used to prepare ATAC-seq libraries as described previously [76]. Cells for each PDL were seeded in 6-well plates at 200,000 cells/well. After treatment with either control (DMEM with vehicle supplemented with 2% FBS) or 4 ng/mL TGF-β1 (R&D Systems), the cells were washed with PBS and detached using trypsin/EDTA after 48 h. Using 200,000 cells of each PDL, ATAC-seq libraries were constructed using an ATAC-Seq Kit (Active Motif) according to the manufacturer's protocol. The ATAC-seq data were generated as paired-end 150 base reads on the NovaSeq 6000 (Illumina).

For treatment with ATRA, HFF-1 cells (PDL 24) were seeded in 6-well plates at a density of 200,000 cells/well, serum-starved with 0.1% FBS for 24 h, and pretreated with 0.1% DMSO or 5 μM ATRA in 0.1% FBS DMEM for 1 h. After pretreatment, the cells were exposed to one of the following conditions: control (DMEM with 2% FBS and 0.1% DMSO vehicle), 4 ng/mL TGF-β1 (R&D Systems), or 5 μM ATRA with or without 4 ng/mL TGF-β1. Next, the cells were washed with PBS and harvested using trypsin/EDTA after 48 h.

All ATAC-seq data were analyzed using the nfcore/atacseq pipeline version 1.2.1 with default parameters using the "nextflow run nf-core/atacseq -r 1.2.1 -profile singularity –input samplesheet_ATAC.csv –genome GRCh38 –save_reference –max_cpus 16 –max_memory 256.GB" arguments. The downstream procedure is similar to that for the ChIP-seq analysis (for more detail, see the nf-core/atacseq pipeline [https://nf-co.re/atacseq/1.2.1]).

***Transcription factor (TF) Network Analysis***

For the TF network analysis, the differentially expressed genes (DEGs) in each RNA-seq were used as input, and the associated TF network was constructed using Epigenetic Landscape In Silico deletion Analysis (Lisa) version 1.0. The FC and adj-p were calculated for PDL 24 vs. PDL 36, PDL 24 vs. PDL 47, and PDL 36 vs. PDL 47 (DEGs: $|FC| > 1.2$, adj-$p < 0.05$) using DESeq2 version 1.36.0 to extract DEGs of the associated TF network with increasing PDL. Next, to identify DEGs in HFF-1 cells treated with control, ATRA, TGF-β1, and TGF-β1 + ATRA, I

calculated FC and adj-p for control vs. ATRA, control vs. TGF-β1, TGF-β1 vs. TGF-β1 + ATRA (DEGs: |FC| > 1.2, adj-p < 0.05) using DESeq2 version 1.36.0. The DEG symbol name was used as input to identify the TF network controlling the DEGs using Lisa. The DEG symbol name was used as input to identify the TF network controlling the DEGs using Lisa with "time lisa model –clean=True –method="all" –web=True –new_rp_h5=None –new_count_h5=None –species hg38 –epigenome "['Dnase', 'H3K27ac']" –cluster=False –covariates=False –random=True –prefix first_run –background=None –stat_background_number=1000 –threads 30 upregulated_DEGs_SYMBOL.symbol downregulated_DEGs_SYMBOL.symbol".

***TF Enrichment***

The activity of the top 20 TFs was determined for the DEGs according to the FC value for RNA-seq data between PDLs and normalized transcripts per million (TPM) value for RNA-seq data using DoRothEA version 1.8.0 as described previously [76]. First, to identify the DEGs in RS induced HFF-1 cells, the FC and adj-p were calculated for PDL 24 vs. PDL 36, PDL 24 vs. PDL 47, and PDL 36 vs. PDL 47 (DEGs: |FC| > 1.2, adj-p < 0.05) using DESeq2. DEGs and FC values were used as input to identify the top 20 TFs regulating the DEGs using DoRothEA (confidence level A, B, and C). The top 20 TFs were identified by extracting the top 10 TFs for PDL 24 vs. PDL 36, PDL 24 vs. PDL 47, and PDL 36 vs. PDL 47, excluding duplicate TFs. Finally, a normalized enrichment score (based on DoRothEA) was calculated for the top 20 TFs using normalized TPM values for all genes greater than five.

To identify the TF activity in HFF-1 cells treated with control, ATRA, TGF-β1, and TGF-β1 + ATRA, I first calculated FC and adj-p for control vs. ATRA, control vs. TGF-β1, TGF-β1 vs. TGF-β1 + ATRA (DEGs: |FC| > 1.2, adj-p < 0.05) using DESeq2. Next, DEGs and FC values were used as input to identify TFs that regulated the DEGs using DoRothEA (confidence levels A, B, and C). Finally, a normalized enrichment score (based on DoRothEA) was calculated for SMAD3, SMAD4, TEAD1, TEAD4, RARA, and RXRA using normalized TPM values for all genes greater than five.

***Motif Analysis***

Motif analysis was performed using HOMER version 4.11 as described previously [76]. Briefly, I first calculated the gain peak region of ATAC-seq from the counts at the consensus peak using DESeq2. The region with $\log_2$FC > 0 and adj-p < 0.05 was defined as the gain peak that significantly increases with increasing PDL. Next, the gained peaks for PDL 24 vs. PDL 36, PDL 24 vs. PDL 47, and PDL 36 vs. PDL 47 were concatenated using the "cat" command, sorted and merged using "sortBed" and "mergeBed," respectively, in Bedtools version 2.30.0. The concatenated gained peak bed file was analyzed with "findMotifsGenome.pl hg38 -size given -p

8" in HOMER to output log (adj-p value) and percent of target sequences with motif from knownResults.html.

***Gene Annotation of ATAC-seq and ChIP-seq Peaks and Intersection with DEGs***

Peak annotation for ATAC-seq and ChIP-seq was performed using "annotatePeak" in the R package ChIPseeker version 1.32.1 as described previously [76]. First, the region with |log2FC| > 0 and adj-p < 0.05 was defined as the differential peak that changes significantly for PDL 24 vs. PDL 36, PDL 24 vs. PDL 47, and PDL 36 vs. PDL 47 using DESeq2. Next, differential peaks were concatenated using the "cat" command, sorted and merged using "sortBed" and "mergeBed" in Bedtools. The differential peaks were annotated as the nearest neighboring gene with the closest distance from the peak to the transcription start site (TSS). The TSS region occurred from –3kb to +3kb. The annotation package for hg38 (TxDb.Hsapiens.UCSC.hg38.knownGene) was used as the TxDb object[80]. Peak annotation was conducted with the "tssRegion=c (-3000, 3000), TxDb=TxDb.Hsapiens.UCSC.hg38.knownGene, annoDb='org.Hs.eg.db'" option. DEGs from the RNA-seq data were identified for PDL 24 vs. PDL 36, PDL 24 vs. PDL 47, and PDL 36 vs. PDL 47 using DESeq2 (DEGs: |FC| > 1.2, adj-p < 0.05). Venn diagrams were created using DEGs and annotated genes from differential peaks in both the ATAC-seq and ChIP-seq data.

***Ingenuity Pathway Analysis (IPA)***

IPA was performed for upstream analysis using IPA tool version 81348237 software as described previously [76]. The gene set was mapped to Ingenuity Knowledge Base using "core analysis." Molecule type, genes, RNAs, and proteins were used for the upstream analysis. A right-tailed Fisher's exact test was used to calculate a p-value of overlap determining the probability that the association between the gene set and the upstream regulators is explained by chance alone. The Benjamini–Hochberg (BH) method for multiple testing was used to calculate the adjusted p-value.

***Analysis of Public in vivo and in vitro RNA-seq Data***

All public RNA-seq data used the same genomic alignment and read count matrix pipeline as described in the "Sample preparation for RNA-seq and genomic alignment" as described previously [76].

*In vivo* RNA-seq data (GSE113957) of human arm skin was analyzed after filtering outliers and clustering. Since multiple ethnic and tissue sources were included, data for 55 samples were manually selected for skin fibroblasts derived from Caucasian individuals (11–71 years of age, see donor list in Table 2.4.1). The samples were manually divided into three clusters according to age (young: 10s to 20s; middle: 30s to 50s; aged: 60s to 70s). For each cluster, a robust principal component analysis (PCA) was performed using "rrcov" version 1.5.2 to detect outliers, resulting

in a final dataset with 45 samples. Spearman's correlation coefficient was calculated to evaluate the distance between each sample using normalized TPM values: distance =1 – Spearman's correlation coefficient. Using the distance calculated, samples were clustered using the "hclust" function in R with "distance, method='ward.D2'" (Figure 2.4.1). Finally, DEGs were identified by comparing each cluster using DESeq2 (DEGs: $|FC| > 1.5$, adj-$p < 0.05$). The BH method was used to calculate the adjusted p-value.

**Table 2.4.1**: Detailed information on donors in public *in vivo* expression data.

| **Run** | **Age (years)** | **Disease** | **Gender** | **Source** | **Ethnicity** | **Sample filtering** |
|---|---|---|---|---|---|---|
| SRR7093887 | 11 | Healthy | Female | Skin; Arm | Caucasian | Omitted |
| SRR7093888 | 11 | Healthy | Female | Skin; Arm | Caucasian | Used |
| SRR7093889 | 12 | Healthy | Male | Skin; Arm | Caucasian | Used |
| SRR7093897 | 19 | Healthy | Male | Skin; Arm | Caucasian | Used |
| SRR7093899 | 20 | Healthy | Female | Skin; Arm | Caucasian | Used |
| SRR7093811 | 24 | Healthy | Female | Skin; Arm | Caucasian | Used |
| SRR7093930 | 24 | Healthy | Male | Skin; Arm | Caucasian | Used |
| SRR7093812 | 25 | Healthy | Male | Skin; Arm | Caucasian | Used |
| SRR7093813 | 25 | Healthy | Female | Skin; Arm | Caucasian | Used |
| SRR7093928 | 25 | Healthy | Female | Skin; Arm | Caucasian | Used |
| SRR7093814 | 26 | Healthy | Male | Skin; Arm | Caucasian | Used |
| SRR7093815 | 26 | Healthy | Female | Skin; Arm | Caucasian | Used |
| SRR7093816 | 28 | Healthy | Male | Skin; Arm | Caucasian | Used |
| SRR7093817 | 29 | Healthy | Male | Skin; Arm | Caucasian | Used |
| SRR7093818 | 29 | Healthy | Male | Skin; Arm | Caucasian | Omitted |
| SRR7093819 | 30 | Healthy | Male | Skin; Arm | Caucasian | Used |
| SRR7093820 | 30 | Healthy | Female | Skin; Arm | Caucasian | Used |
| SRR7093821 | 30 | Healthy | Male | Skin; Arm | Caucasian | Omitted |
| SRR7093822 | 30 | Healthy | Male | Skin; Arm | Caucasian | Used |
| SRR7093908 | 37 | Healthy | Male | Skin; Arm | Caucasian | Used |
| SRR7093909 | 39 | Healthy | Male | Skin; Arm | Caucasian | Omitted |
| SRR7093825 | 41 | Healthy | Male | Skin; Arm | Caucasian | Used |
| SRR7093832 | 41 | Healthy | Female | Skin; Arm | Caucasian | Omitted |
| SRR7093830 | 42 | Healthy | Female | Skin; Arm | Caucasian | Used |

| | | | | | | |
|---|---|---|---|---|---|---|
| SRR7093823 | 43 | Healthy | Female | Skin; Arm | Caucasian | Used |
| SRR7093833 | 43 | Healthy | Male | Skin; Arm | Caucasian | Used |
| SRR7093824 | 44 | Healthy | Male | Skin; Arm | Caucasian | Used |
| SRR7093834 | 44 | Healthy | Male | Skin; Arm | Caucasian | Used |
| SRR7093835 | 45 | Healthy | Male | Skin; Arm | Caucasian | Used |
| SRR7093828 | 46 | Healthy | Male | Skin; Arm | Caucasian | Used |
| SRR7093836 | 46 | Healthy | Male | Skin; Arm | Caucasian | Omitted |
| SRR7093837 | 46 | Healthy | Male | Skin; Arm | Caucasian | Used |
| SRR7093826 | 47 | Healthy | Male | Skin; Arm | Caucasian | Used |
| SRR7093831 | 47 | Healthy | Male | Skin; Arm | Caucasian | Used |
| SRR7093838 | 47 | Healthy | Male | Skin; Arm | Caucasian | Used |
| SRR7093827 | 50 | Healthy | Female | Skin; Arm | Caucasian | Used |
| SRR7093829 | 50 | Healthy | Male | Skin; Arm | Caucasian | Used |
| SRR7093910 | 51 | Healthy | Male | Skin; Arm | Caucasian | Omitted |
| SRR7093912 | 55 | Healthy | Male | Skin; Arm | Caucasian | Omitted |
| SRR7093839 | 61 | Healthy | Male | Skin; Arm | Caucasian | Used |
| SRR7093840 | 62 | Healthy | Female | Skin; Arm | Caucasian | Used |
| SRR7093841 | 62 | Healthy | Female | Skin; Arm | Caucasian | Used |
| SRR7093842 | 63 | Healthy | Male | Skin; Arm | Caucasian | Used |
| SRR7093843 | 64 | Healthy | Male | Skin; Arm | Caucasian | Used |
| SRR7093844 | 66 | Healthy | Male | Skin; Arm | Caucasian | Used |
| SRR7093845 | 67 | Healthy | Male | Skin; Arm | Caucasian | Used |
| SRR7093846 | 67 | Healthy | Male | Skin; Arm | Caucasian | Used |
| SRR7093847 | 68 | Healthy | Male | Skin; Arm | Caucasian | Omitted |
| SRR7093848 | 68 | Healthy | Male | Skin; Arm | Caucasian | Used |
| SRR7093939 | 68 | Healthy | Male | Skin; Arm | Caucasian | Omitted |
| SRR7093849 | 69 | Healthy | Male | Skin; Arm | Caucasian | Used |
| SRR7093850 | 69 | Healthy | Female | Skin; Arm | Caucasian | Used |
| SRR7093941 | 69 | Healthy | Male | Skin; Arm | Caucasian | Used |
| SRR7093940 | 70 | Healthy | Male | Skin; Arm | Caucasian | Used |
| SRR7093915 | 71 | Healthy | Female | Skin; Arm | Caucasian | Used |

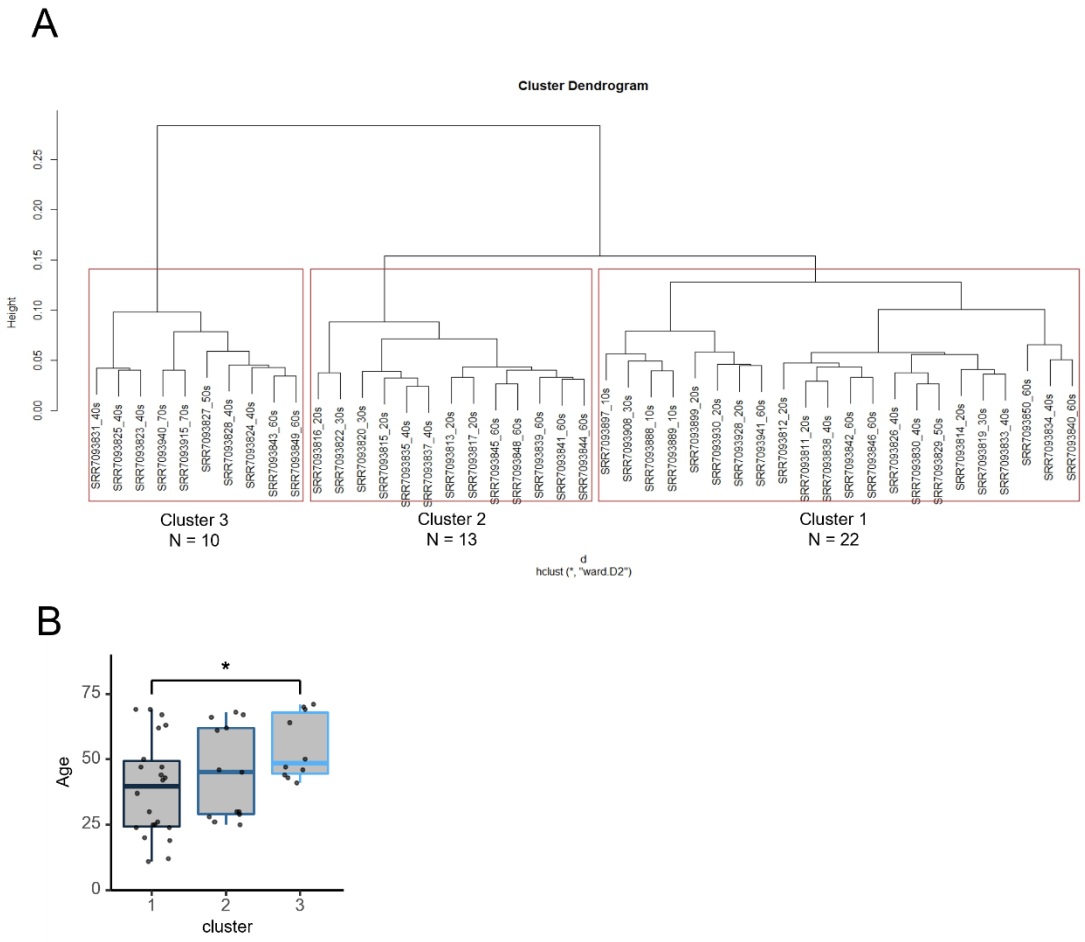


**Figure 2.4.1**: Analysis of public in vivo omics data on aging.

A) Clustering of public data on human skin fibroblast RNA-seq samples. Samples from human arm skin fibroblast (age: 11–71 years, n = 45) were clustered into cluster 1 (n = 22), cluster 2 (n = 13), and cluster 3 (n = 10) using the "hclust" function of R with "method = ward.D2."

B) Age distribution of the clustered human skin fibroblast samples. The median (cluster 1: 39.5 years; cluster 2: 45.0 years; cluster 3: 48.5 years) and average (cluster 1: 38.9 years; cluster 2: 44.8 years; cluster 3: 54.5 years) of each cluster increased with the cluster number; n = 3, *p < 0.05 (Wilcoxon rank sum test).

*In vitro* RNA-seq data (GSE63577) for the human dermal fibroblast HFF-1 cell line was compared for each PDL (PDL 16, PDL 26, PDL 46, PDL 64, and PDL 74). DEGs were identified for PDL 16 vs. PDL 26, PDL 16 vs. PDL 46, PDL 16 vs. PDL 64, PDL 16 vs. PDL 74, PDL 26 vs. PDL 46, PDL 26 vs. PDL 64, PDL 26 vs. PDL 74, PDL 46 vs. PDL 64, PDL 46 vs. PDL 74, and PDL 64 vs. PDL 74 using DESeq2 (DEGs: |FC| > 2.0, adj-p < 0.01) and intersected. The BH method was used to calculate the adjusted p-value.

RNA-seq data for skin fibroblasts from healthy subjects (age: 1–9 years, n = 12) and Hutchinson–Gilford progeria syndrome (HGPS) patients (age: 2–8 years, n = 10) were downloaded from GSE113957 (see donor list in Table 2.4.2).

**Table 2.4.2**: Detailed information on donors in public *in vivo* expression data.

| Run | Age (years) | Disease | Gender | Source | Ethnicity |
|---|---|---|---|---|---|
| SRR7093809 | 1 | Healthy | Male | Skin; Foreskin | Asian |
| SRR7093874 | 1 | Healthy | Male | Skin; Unspecified | Caucasian |
| SRR7093875 | 2 | Healthy | Female | Skin; Unspecified | Caucasian |
| SRR7093876 | 3 | Healthy | Male | Skin; Inguinal area | Latino/Hispanic |
| SRR7093877 | 3 | Healthy | Male | Skin; Unspecified | NA |
| SRR7093878 | 5 | Healthy | Male | Skin; Umbilical cord area | Black |
| SRR7093879 | 6 | Healthy | Male | Skin; Inguinal area | Black |
| SRR7093880 | 7 | Healthy | Male | Skin; Inguinal area | Black |
| SRR7093881 | 7 | Healthy | Male | Skin; Unspecified | Caucasian |
| SRR7093882 | 8 | Healthy | Male | Skin; Unspecified | Caucasian |
| SRR7093883 | 8 | Healthy | Male | Skin; Inguinal area | Caucasian |
| SRR7093884 | 9 | Healthy | Female | Skin; Unspecified | Black |
| SRR7093942 | 8 | HGPS | Female | Skin; Leg | Caucasian |
| SRR7093943 | 8 | HGPS | Male | NA | NA |
| SRR7093944 | 2 + 3 months | HGPS | Female | NA | NA |
| SRR7093945 | 3 + 9 months | HGPS | Female | NA | NA |

| | | | | | |
|---|---|---|---|---|---|
| SRR7093946 | 4 + 8 months | HGPS | Female | NA | NA |
| SRR7093947 | 8 + 6 months | HGPS | Male | NA | NA |
| SRR7093948 | 6 + 11 months | HGPS | Female | NA | NA |
| SRR7093949 | 5 | HGPS | Female | NA | NA |
| SRR7093950 | 8 + 10 months | HGPS | Male | NA | NA |
| SRR7093951 | 3 | HGPS | Female | NA | NA |

***Kyoto Encyclopedia of Genes and Genomes (KEGG) Analysis of Public RNA-seq***

KEGG enrichment was compared using the "comparecluster" function in the R package clusterProfiler version 4.4.4 with "fun"=enrichKEGG, "organism"=I, "keyType"= 28 eg, "pAdjustMethod"=BH, "minGSSize"=10, "maxGSSize"=500, "pvalueCutoff"=0.05, "qvalueCutoff"=0.05, and "use_internal_data"="FALSE" as described previously [76]. The BH method was used to calculate the adjusted p-value.

***Correlation Analysis of TGF-β Pathway-Enriched Genes Using Public RNA-seq Data***

Spearman's correlation between age and gene expression was calculated for the *in vivo* data or PDL and gene expression for the *in vitro* data using "cor" (method = "spearman") in R as described previously [76]. The genes associated with KEGG term "TGF-beta signaling pathway" in Figure 3.1.3D are plotted.

***Integrated Analysis of ATAC-seq and RNA-seq of TGF-β1 Treatment***

Peak annotation for ATAC-seq was performed using "annotatePeak" in the R package ChIPseeker version 1.32.1 as described previously [76]. Briefly, the region with adj-p < 0.05 was defined as the differential peak that changes significantly for control vs. 4 ng/mL TGF-β1 using DESeq2. The differential peaks were annotated as the nearest neighboring gene with the closest distance from the peak to the TSS. The TSS region occurred from –3 kb to +3 kb. The annotation package for hg38 (TxDb.Hsapiens.UCSC.hg38.knownGene) was used as the TxDb object [83]. Peak annotation was conducted with the "tssRegion = c (-3000, 3000), TxDb = TxDb.Hsapiens.UCSC.hg38.knownGene, annoDb = 'org.Hs.eg.db'" option. DEGs from the RNA-seq data were identified for control vs. 4 ng/mL TGF-β1 using DESeq2 (adj-p < 0.05).

***Visualization of the Genomic Location of THBS1***

Integrative Genomics Viewer version 2.8.0 was used as the genome browser to view THBS1 genomic locations. Briefly, I defined the region with |FC| > 1.2 as the differential peak that changed significantly for control vs. ATRA, control vs. TGF-β1, TGF-β1 vs. TGF-β1 + ATRA

using DESeq2. The differential peaks were annotated as the nearest neighboring gene with the closest distance from the peak to the transcription start site (TSS) using ChIPseeker version 1.32.1. The TSS region was defined as the region from −3 kb to +3 kb. The annotation package for hg38 (TxDb.Hsapiens.UCSC.hg38.knownGene) was used as the TxDb object [83]. Peaks annotated as THBS1 were defined as variable regions of open chromatin near THBS1.

***Enrichment Analysis of TF Near THBS1 Genomic Loci***

The enrichment analysis of ChIP-Atlas (https://chip-atlas.org) was performed to identify the common epigenetic features of fluctuating ATAC-seq-derived genomic loci annotated as the variable regions of the open chromatin near THBS1. The enrichment analysis was performed with the following options: Experiment type = ChIP: TFs and others, cell type class = epidermis, and threshold for significance = 500. The ATAC-seq-derived genomic loci annotated as the variable regions of the open chromatin near THBS1 were obtained as described in the previous section.

The list of TFs annotated as THBS1-related TFs in the Signaling Pathways Project (https://signalingpathways.org) was obtained with the following options: Type = cistromic, gene(s) of interest = single gene, THBS1, signaling pathway category = all, signaling pathway class = all, signaling pathway family = all, and biosample category = all species.

***Extraction of Genes to which RARA/RXRA Bind in the Vicinity Using ChIP-Atlas***

To extract the neighboring genes to which RARA/RXRA bind, I used ChIP-Atlas to obtain the DNA regions to which RARA and RXRA bind, followed by obtaining a list of the neighboring genes. Initially, I identified DNA regions bound by RARA and RXRA using the peak browser function of ChIP-Atlas with the following conditions: experiment type = ChIP: TFs and others, cell type class = all cell types, threshold for significance = 500, and ChIP antigen = RARA or RXRA. Next, the peaks were annotated to neighboring genes using HOMER with the "annotatePeaks.pl Input.bed hg38" option. Finally, I counted the annotated genes from each peak of RARA and RXRA, constructed two clusters based on these counts, and extracted the common genes from the peaks.

***Extraction of Human Skin Tissue Protein***

Skin tissue proteins were extracted after dividing full thickness skin into dermis and epidermis [84]. In detail, a biopsy punch (tip diameter: 3 mm ø) was used to collect a full-layer skin sample (see donor list in Table 2.2.1), from which hypodermis tissue was physically removed. After washing in 70% ethanol and HBSS (Thermo Fisher Scientific), samples were treated with 25 UI/mL Dispase II (Roche) HBSS solution for 15 h at 4°C. Enzymatic digestion was inactivated with HBSS supplemented with 10% FBS and the dermis and epidermis were separated with

tweezers. Each dermis and epidermis were separately homogenized in RIPA buffer (Thermo Fisher Scientific) supplemented with Halt™ Protease and Phosphatase Inhibitor (Thermo Fisher Scientific) for 10 min using a Powermasher II (Nippi) and centrifuged (13,000 rpm, 20 min, 4°C) to generate protein extracts for western blot (WB) analysis.

***Time-Course Cell Proliferation Analysis (Trypan Blue)***

HFF-1 cells were seeded in 6-well plates with DMEM at 200,000 cells/well. After serum starvation for 16 h, cells were treated with either control (DMEM with vehicle supplemented with 2% FBS) or 4 ng/mL TGF-β1 (R&D Systems) and collected at 0 h, 8 h, 12 h, 24 h, and 48 h. Reconstitution buffer (0.1% bovine serum albumin [BSA] in 4 mM HCl PBS; R&D Systems) was used as vehicle and to dissolve TGF-β1. At each time-point, cells were washed with PBS and detached using trypsin/EDTA to count cells positive for trypan blue (Thermo Fisher Scientific) using a cell counter (WakenBtech) according to the manufacturer's protocol.

***Cell Viability Analysis (WST-8)***

HFF-1 cells were seeded in 96-well plates with DMEM at 10,000 cells/well. After serum starvation for 16 h, cells were treated with each treatment. After 24 h, 10 μL Cell Counting Kit-8 solution (DOJINDO) was added, incubated for 1 h, and cell viability was calculated at an absorbance wavelength of 450 nm using a Multiskan FC system (Thermo Fisher Scientific).

***5-Bromo-2-Deoxyuridine (BrdU) Incorporation Assay***

The inhibition of DNA synthesis was measured using a CycLex Cellular BrdU enzyme-linked immunosorbent assay (ELISA) Kit Ver.2 (Medical & Biological Laboratories) according to the manufacturer's instructions. Briefly, HFF-1 cells were seeded in 96-well plates with DMEM at 10,000 cells/well. After 16 h of serum starvation, cells were treated with either control (DMEM with vehicle supplemented with 2% FBS), 4 ng/mL TGF-β1 (R&D Systems), or 1 μg/mL THBS1 (R&D Systems). After 8 h, the cells were incubated with anti-BrdU antibody and substrate for 16 h, and absorbance was measured at 450 nm with 540 nm as a reference using the Multiskan FC system (Thermo Fisher Scientific).

***Senescence-Associated β-galactosidase (SA-β-gal) Staining***

The rate of positive SA-β-gal staining was calculated using a SA-β-gal Detection Kit (BioVision) according to the manufacturer's protocol. Briefly, cells were seeded in 12-well plates at 100,000 cells/well, treated with each stimulant, and fixed for 10 min with fixative solution after 48 h. The cells were stained with Staining Solution Mix at 37°C overnight. After washing with PBS, cells were treated with Hoechst® 33342 (DOJINDO) for 10 min and washed with PBS before

observation (BZ-9000, KEYENCE). SA-β-gal-positive rates were calculated as follows: SA-β-gal-positive rate (%) = (number of SA-β-gal-positive cells per image/total number of cells per image) × 100. For each treatment, 12 images were randomly analyzed. The number of SA-β-gal-positive cells was determined using thresholds for each experiment using ImageJ Fiji software (The National Institutes of Health). All image files were split into red, blue, and green channels. The red channels were subtracted from the green channels, and thresholds of 20 and 30 were set to identify SA-β-gal-positive cells. The total number of cells per image was counted as Hoechst® 33342-positive cells using ImageJ Fiji software.

***siRNA Transfection***

HFF-1 cells were transfected with siRNA oligomer (Dharmacon/Horizon Discovery) mixed with Lipofectamine RNAiMAX reagent (Thermo Fisher Scientific) in Opti-MEM™ I (Thermo Fisher Scientific) according to the manufacturer's instructions as described previously [76]. Briefly, cells were seeded in 6-well plates with DMEM at 200,000 cells/well. After transfection for 24 h in serum-starved conditions, cells were treated with either control (DMEM with vehicle supplemented with 2% FBS) or 4 ng/mL TGF-β1 (R&D Systems) and the lysates or its supernatants were collected for further quantification. KD efficacy of c-Fos and c-Jun at 50 nM siRNA are shown in Figure S5B. In addition, KD efficacy at 48 h post-stimulation of SMAD2, SMAD3, and SMAD4 at 25 nM siRNA is shown in Figure S13B.

***Inhibitor Screening for FMOD Regulatory Pathway***

HFF-1 cells were seeded in 96-well plates with DMEM at 10,000 cells/well. Cells were treated with control (DMEM with 2% FBS-added vehicle) or 4 ng/mL TGF-β1(R&D Systems) with or without each inhibitor, and supernatants were collected for FMOD ELISA. The following inhibitors were used: Akt inhibitor VIII (14870, Cayman Chemical) and LY294002 (440202, Calbiochem). The other inhibitors used were dispensed from a Tocriscreen Kinase Inhibitor Toolbox (3514, Tocris Bioscience).

***Inhibitor Treatment for THBS1 Regulatory Pathway***

HFF-1 cells were seeded in 6-well plates with DMEM at 200,000 cells/well. Cells were treated with control (DMEM with 2% FBS-added vehicle) or 4 ng/mL TGF-β1 (R&D Systems) with or without each inhibitor, and the lysates were collected after 48 h for quantification by WB. The following inhibitors were used: LY364947 (123-05981, Fujifilm), SB431542 (dispensed from a Tocriscreen Kinase Inhibitor Toolbox [3514, Tocris Bioscience]), and T-5224 (S28966, Selleck).

***Bifurcation Model Analysis***

Dr. Keita Iida contributed to the bifurcation analyses as described previously [76]. Based on the experimental expression of THBS1 and FMOD upon treatment with different concentrations of TGF-β1 (Figure 3.1.6A), we constructed a core transcription factor network consisting of TGF-β1, THBS1, and FMOD. A double positive feedback loop (between THBS1 and TGF-β1) and double negative feedback loop (between FMOD and TGF-β1) can be described by the following nonlinear ordinary differential equations (ODEs):

$$\frac{\mathrm{d}[\mathrm{THBS1}]}{\mathrm{d}t} = a\left(\frac{[\mathrm{TGF\beta1}]^{n_a}}{[\mathrm{TGF\beta1}]^{n_a} + K_a}\right) - d_1[\mathrm{THBS1}], \tag{1}$$

$$\frac{\mathrm{d}[\mathrm{FMOD}]}{\mathrm{d}t} = b\left(\frac{K_b}{[\mathrm{TGF\beta1}]^{n_b} + K_b}\right) - d_2[\mathrm{FMOD}], \tag{2}$$

$$\frac{\mathrm{d}[\mathrm{TGF\beta1}]}{\mathrm{d}t} = c\left(\frac{[\mathrm{THBS1}]}{[\mathrm{THBS1}] + K_1}\right)\left(\frac{K_2}{[\mathrm{FMOD}] + K_2}\right) - d_3[\mathrm{TGF\beta1}], \tag{3}$$

where $a/d_1$, $b/d_2$, and $c/d_3$ are maximal values of $[\mathrm{THBS1}]$, $[\mathrm{FMOD}]$, and $[\mathrm{TGF\beta1}]$, respectively; $K_a$, $K_b$, $K_1$, and $K_2$ are the half saturation constants; and $n_a$ and $n_b$ are Hill coefficients. Setting the left-hand sides of Eqs. (1)–(3) to zero, the steady state solutions can be obtained as follows:

$$\overline{[\mathrm{THBS1}]} = \frac{a}{d_1}\left(\frac{\overline{[\mathrm{TGF\beta1}]}^{n_a}}{\overline{[\mathrm{TGF\beta1}]}^{n_a} + K_a}\right), \tag{4}$$

$$\overline{[\mathrm{FMOD}]} = \frac{b}{d_2}\left(\frac{K_b}{\overline{[\mathrm{TGF\beta1}]}^{n_b} + K_b}\right), \tag{5}$$

$$\overline{[\mathrm{TGF\beta1}]} = \frac{c}{d_3}\left(\frac{\overline{[\mathrm{THBS1}]}}{\overline{[\mathrm{THBS1}]} + K_1}\right)\left(\frac{K_2}{\overline{[\mathrm{FMOD}]} + K_2}\right). \tag{6}$$

Substituting (4) and (5) into (6), $\overline{[\mathrm{TGF\beta1}]}$ can be computed using Newton's method and stability can be determined by the sign of the derivative. Note that $\overline{[\mathrm{THBS1}]} \equiv 0$, $\overline{[\mathrm{FMOD}]} \equiv b/d_2$, and $\overline{[\mathrm{TGF\beta1}]} \equiv 0$ are stable steady state solutions for $K_1 > 0$ and $K_2 > 0$. By fitting (4) and (5) to the experimental data (Figure 3.1.6A), the parameters were inferred using a nonlinear least-squares method with Gnuplot (version 5.4); $a/d_1 = 2.36$, $b/d_2 = 0.33$, $K_a = 0.016$, $K_b = 0.002$, $n_a = 1.6$, and $n_b = 1.7$ (Figure 3.1.9B).

To understand the roles of endogenous TGF-β1, THBS1, and FMOD, we extended (6) to incorporate the effects of PDL and endogenous TGF-β1 production as described below:

$$\overline{[\mathrm{THBS1 \cdot PDL}]} = \alpha\left(\frac{\mathrm{PDL}}{\mathrm{PDL} + K_\alpha}\right), \tag{7}$$

$$\overline{[\mathrm{FMOD \cdot PDL}]} = \beta\left(\frac{K_\beta}{\mathrm{PDL} + K_\beta}\right), \tag{8}$$

$$\overline{[\mathrm{TGF\beta1}]} = \gamma\left(\frac{\overline{[\mathrm{THBS1 \cdot PDL}]}}{\overline{[\mathrm{THBS1 \cdot PDL}]} + \widetilde{K_1}}\right)\left(\frac{\widetilde{K_2}}{\overline{[\mathrm{FMOD \cdot PDL}]} + \widetilde{K_2}}\right), \tag{9}$$

where $\overline{[\mathrm{THBS1}\cdot\mathrm{PDL}]}$, $\overline{[\mathrm{FMOD}\cdot\mathrm{PDL}]}$, and $\overline{[\mathrm{TGF\beta1}]}$ are endogenous concentrations of THBS1, FMOD, and TGF-β1, respectively, $\alpha$, $\beta$, and $\gamma$ are the maximal values of $[\mathrm{THBS1}\cdot\mathrm{PDL}]$, $[\mathrm{FMOD}\cdot\mathrm{PDL}]$, and $[\mathrm{TGF\beta1}]$, and $K_\alpha$, $K_\beta$, $\widetilde{K_1}$, and $\widetilde{K_2}$ are the half saturation constants, respectively. In particular, $\gamma$ represents the endogenous TGF-β1 production rate. In the same manner as before, we fitted (7)-(9) to the experimental data (Figure 3.1.9C) to identify all the parameter values: $\alpha = 3$, $\beta = 5$, $\gamma = 3.5$, $K_\alpha = 10.1$, $K_\beta = 5$, $\widetilde{K_1} = 0.46$, and $\widetilde{K_2} = 0.62$. The bifurcation diagram is depicted using (4)-(6) by replacing $c/d_3$, $K_1$, and $K_2$ with $\gamma$, $\widetilde{K_1}$, and $\widetilde{K_2}$ (Figure 3.1.9E).

Moreover, for simulating the immunostaining experiment (Figure 3.1.12), we extended the model (4)–(6) to a stochastic model by computing probability distributions of $[\mathrm{THBS1}]$ and $[\mathrm{FMOD}]$ for a given $[\mathrm{TGF\beta1}]$. Using an Ornstein–Uhlenbeck process as a model of gene expression[82], we formulated the dynamics of $[\mathrm{THBS1}]$ and $[\mathrm{FMOD}]$ by the following stochastic differential equations:

$$\mathrm{d}[\mathrm{THBS1}] = \left(f_{\mathrm{THBS1}}\left(\overline{[\mathrm{TGF\beta1}]}\right) - [\mathrm{THBS1}]\right)\mathrm{d}t + \sigma_1 \mathrm{d}B_1(t), \tag{10}$$

$$\mathrm{d}[\mathrm{FMOD}] = \left(f_{\mathrm{FMOD}}\left(\overline{[\mathrm{TGF\beta1}]}\right) - [\mathrm{FMOD}]\right)\mathrm{d}t + \sigma_2 \mathrm{d}B_2(t), \tag{11}$$

where $\mathrm{d}B_1(t)$ and $\mathrm{d}B_2(t)$ are standard Gaussian white noises (mean 0 and variance 1), $\sigma_1$ and $\sigma_2$ are constant parameters, and $f_{\mathrm{THBS1}}$ and $f_{\mathrm{FMOD}}$ are given by the following functions:

$$f_{\mathrm{THBS1}}\left(\overline{[\mathrm{TGF\beta1}]}\right) = \frac{a}{d_1}\left(\frac{\overline{[\mathrm{TGF\beta1}]}^{n_a}}{\overline{[\mathrm{TGF\beta1}]}^{n_a} + K_a}\right),$$

$$f_{\mathrm{FMOD}}\left(\overline{[\mathrm{TGF\beta1}]}\right) = \frac{b}{d_2}\left(\frac{K_b}{\overline{[\mathrm{TGF\beta1}]}^{n_b} + K_b}\right).$$

In our immunostaining experiment, $\overline{[\mathrm{TGF\beta1}]}$ is assumed as a control parameter. Hence, we computed $\overline{[\mathrm{TGF\beta1}]}$ as a time limit of $[\mathrm{TGF\beta1}]$ using the following ODE:

$$\frac{\mathrm{d}[\mathrm{TGF\beta1}]}{\mathrm{d}t} = f_{\mathrm{TGF\beta1}}([\mathrm{TGF\beta1}]) - [\mathrm{TGF\beta1}], \tag{12}$$

where $f_{\mathrm{TGF\beta1}}([\mathrm{TGF\beta1}])$ is given by the following equation:

$$f_{\mathrm{TGF\beta1}}([\mathrm{TGF\beta1}])$$

$$= \frac{c}{d_3}\left(\frac{[\mathrm{TGF\beta1}]^{n_a}}{[\mathrm{TGF\beta1}]^{n_a} + \frac{K_1 d_1}{a}([\mathrm{TGF\beta1}]^{n_a} + K_a)}\right)\left(\frac{\frac{K_2 d_2}{b}([\mathrm{TGF\beta1}]^{n_b} + K_b)}{K_b + \frac{K_2 d_2}{b}([\mathrm{TGF\beta1}]^{n_b} + K_b)}\right).$$

Note that $\overline{[\mathrm{TGF\beta1}]}$ corresponds with (6).

I numerically computed (10) and (11) using Euler-Maruyama method and (12) using Euler method with the following initial conditions:

$$[\mathrm{THBS1}](0) = 0, \tag{12}$$

$$[\mathrm{FMOD}](0) = 0, \tag{13}$$

$$[\mathrm{TGF\beta1}](0) \sim U(0, [\mathrm{TGF\beta1}]_{\max}), \tag{14}$$

where (14) means that the initial value of $[\mathrm{TGF\beta1}]$ is randomly sampled from a uniform distribution $U(0, [\mathrm{TGF\beta1}]_{\max})$. Note that (10) and (11) may yield negative values. In such a case, we addressed it numerically by constraining them to zero. The resulting bias from this adjustment, however, proved to be negligible. I set the parameter values as follows: $\sigma_1 = \sigma_2 = 0.2$ and $[\mathrm{TGF\beta1}]_{\max} = 0.2$ in Figure 4C, and $\sigma_1 = \sigma_2 = 0.05$ and $[\mathrm{TGF\beta1}]_{\max} = 1.0$ in Figure 3.1.11B. I simulated independent 10,000 sample paths for long time enough and obtained a steady state distribution of $[\mathrm{THBS1}]$ and $[\mathrm{FMOD}]$.

***TGF-βR Inhibitor Treatment for Endogenous TGF-β Signaling***

HFF-1 cells (PDL 24, PDL 36, PDL 47, and PDL 53) were seeded in 6-well plates with DMEM at 200,000 cells/well. Cells were treated with control (DMEM with 2% FBS-added vehicle) or 5 μM LY364947 (123-05981, Fujifilm), and the lysates were collected after 48 h for quantification by WB.

***Time-Course Datasets for Mathematical Model Training***

I used the time-course data for phosphorylated SMAD3, c-Fos, THBS1, phosphorylated Akt (Ser473), and FMOD activity with or without 4 ng/mL TGF-β1 (eight time-points up to 48 h) treatment in HFF-1 cells for data-fitting of the comprehensive model as described previously [76]. Briefly, HFF-1 cells were seeded in 6-well plates at 200,000 cells/well and maintained in DMEM supplemented with 10% FBS. After serum starvation for 16 h, the cells were treated with either control (DMEM with vehicle supplemented with 2% FBS) or 4 ng/mL TGF-β1 (R&D Systems) and the lysate and supernatant were collected at 0 min, 15 min, 30 min, 60 min, 120 min, 8 h, 24 h, and 48 h. Reconstitution buffer (0.1% BSA in 4 mM HCl PBS, R&D Systems) was used as vehicle. The cells were lysed with RIPA buffer (Thermo Fisher Scientific) supplemented with Halt™ Protease and Phosphatase Inhibitor (Thermo Fisher Scientific) and used in the western blot analysis for analyzing anti-phosphorylated SMAD3 (Ser423/425; 9520, CST), anti-c-Fos (2250, CST), anti-THBS1 (37879, CST), and anti-phosphorylated Akt (Ser473; 9271, CST) expression. Supernatants were centrifuged (13,000 rpm, 15 min, 4 °C) to remove cell debris and used for the FMOD ELISA (ab275895, Abcam). In addition, anti-phosphorylated SMAD2 data (Ser465/467; 3108, CST) were obtained for model validation and not used in data-fitting. The data were normalized between the minimum (0) and maximum (1) values.

***Model Simulation and Parameter Estimation***

I constructed the comprehensive mathematical model linking the TGF-β and VEGF signaling pathways (Figure 2.3.3) by integrating two mathematical models using a Python framework for Modeling and Analysis of Signaling Systems (BioMASS) as described previously [76].

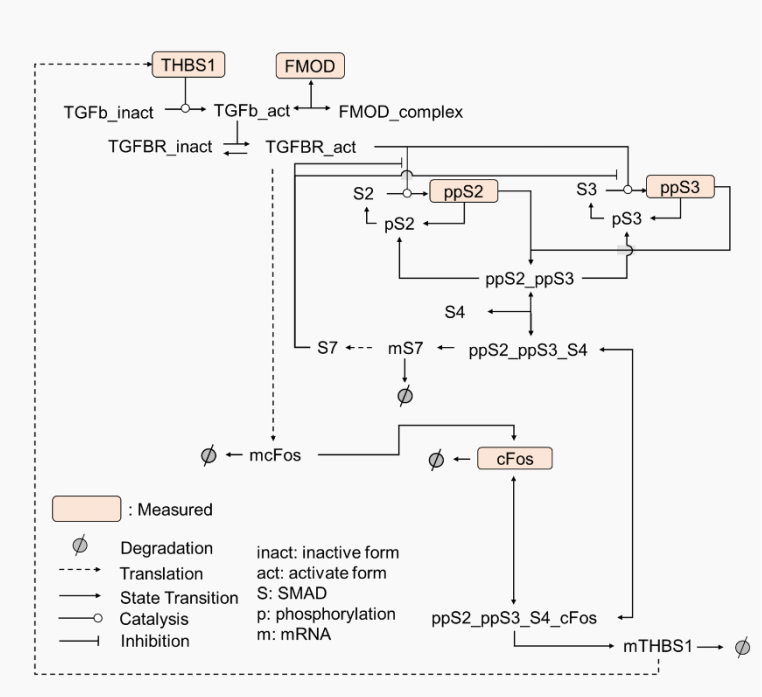


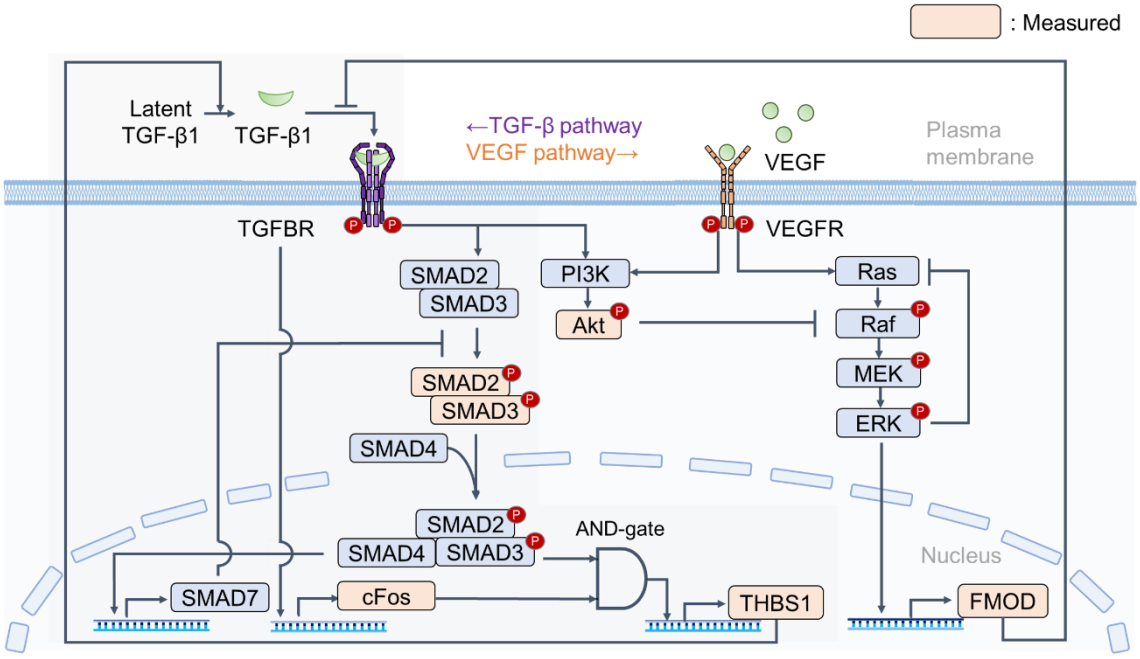


**Figure 2.3.3**: Mathematical model diagram of the TGF-β–VEGF integrated signaling pathway [76].

TGF-β and VEGF signaling pathways in an ordinary differential equation model. (Upper panel) Diagram of molecular interactions in the TGF-β signaling model. A model of TGF-βR activation, SMAD phosphorylation, and SMAD complex formation was developed for the TGF-β pathway. (Lower panel) In addition to the TGF-β signaling model, the process

of VEGFR activation to ERK phosphorylation was described using the Imoto model [68].

Parameter estimation was conducted in two steps. In step one, parameters related to the TGF-β signaling network, modified based on the Lucarelli model [86], were trained using normalized phosphorylated SMAD3, c-Fos, and THBS1 time-course expression. The resulting model had 27 rate equations, 22 species, and 42 parameters, of which 34 were to be estimated. By minimizing the objective function, i.e., the sum of residual squares between simulation and experimental values, 30 fitting parameter sets were obtained that reproduce the experimental results with/without TGF-β1 stimulation in HFF-1 cells. In step two, an additional 30 parameter sets for the rest of the model, including the Raf-ERK cascade and PI3K-Akt pathway, were trained using normalized phosphorylated SMAD3, c-Fos, THBS1, phosphorylated Akt, and FMOD time-course expression. The best fitting parameters in the TGF-β signaling network were adapted from step one. The resulting integrated model had 79 rate equations, 83 species, and 194 parameters. An additional 30 fitting parameter sets were obtained that reproduce the experimental results of TGF-β1 stimulation in HFF-1 cells (parameter range: Figure 2.3.4; objective function trace: Figure 2.3.5).

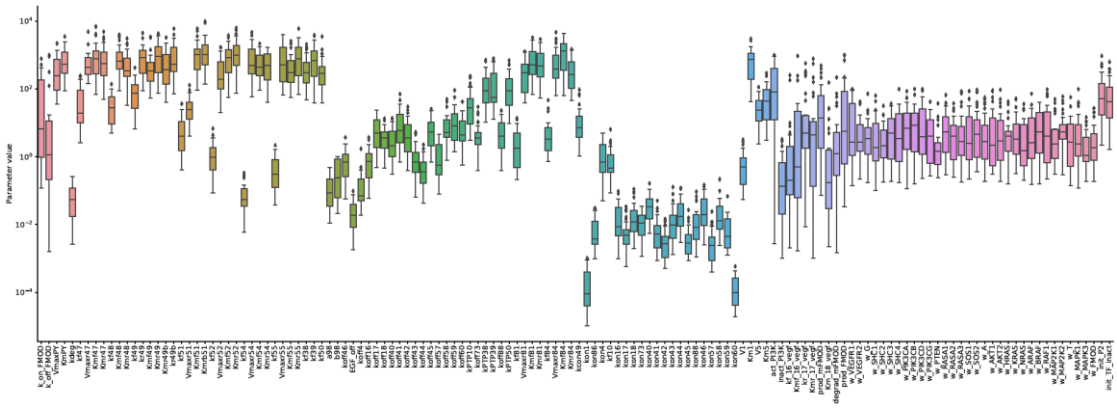


**Figure 2.3.4**: Parameter range [76].
Estimated parameter values of 30 parameter sets for integrated TGF-β–VEGF signaling model.

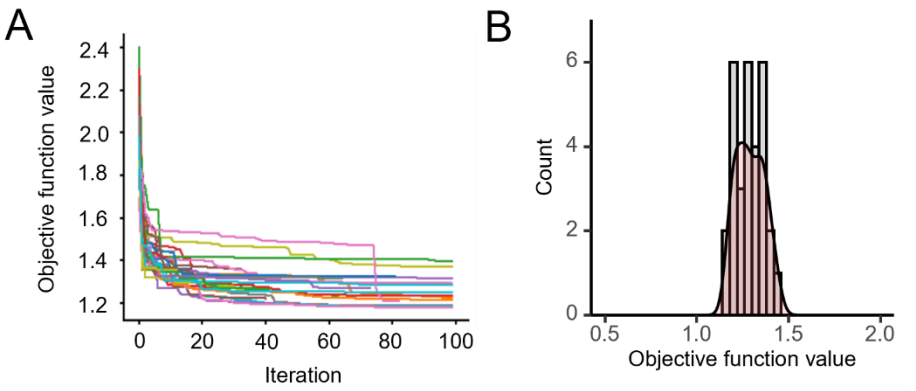


**Figure 2.3.5**: Objective function trace [76].

A) Objective function traces from 30 optimization runs for the integrated TGF-β–VEGF signaling model.

B) Distribution of objective function value of 30 parameter sets. Bar graph: histogram of the count. Shade: density of the count.

For the TGF-β pathway, I developed an original model of TGF-βR activation, SMAD phosphorylation, and SMAD complex formation. This model activates the transcription of c-Fos at the same time and forms a logical AND gate with SMAD complexes to regulate THBS1 expression. THBS1 forms positive feedback and activates latent TGF-β1. I modified the Imoto model [68] to describe the process from VEGFR receptor activation to ERK phosphorylation. ERK phosphorylation results in the activation of TFs for FMOD transcription. FMOD then forms a complex with activated TGF-β1 and inhibits its binding to TGF-βR. The TGF-β and VEGF signaling pathway models crosstalk via the PI3K-Akt pathway.

All related files to execute the TGF-β and TGF-β VEGF model using BioMASS can be found at https://github.com/okadalabipr/Haga2023. I described each biochemical reaction using ODEs. To train model parameters, I used time-series expression data for HFF-1 cells. For the global parameter estimation, I minimized the sum of squared differences between the experimental observations and simulated values using Differential Evolution 87.

***Initial value for mathematical model***

Values measured by ELISA and RNA-seq were used to determine the initial values of the model [76].

The initial value for SMAD2, SMAD3, and SMAD4 were quantified using the respective ELISA kits (SMAD2: 0.060 nM, SMAD3: 0.38 nM, SMAD4: 0.0044 nM). Briefly, HFF-1 cells were seeded in 6-well plates with DMEM at 200,000 cells/well. Cell lysates were collected using the lysate buffer provided with the ELISA kits after serum starvation for 16 h, centrifuged (13,000

rpm, 15 min, 4°C), and used for SMAD2 (ab260065, Abcam), SMAD3 (ab264624, Abcam), and SMAD4 ELISAs (ab253211, Abcam).

For other nonzero species, I used RNA-seq data obtained from non-stimulated HFF-1 cells to determine the initial value. Briefly, HFF-1 cells were seeded in 6-well plates with DMEM at 200,000 cells/well. Total RNA (three wells per sample) was collected after serum starvation for 16 h. RNA purification, sequencing library preparation, and downstream analysis was conducted as described in the "Sample preparation for RNA-seq and genomic alignment" section. Initial protein levels of the model species (total of 37 genes) were inferred from RNA-seq data, where the maximal transcription rate or translated protein level were estimated from the mRNA level68,88. I estimated protein amounts from one or more genes belonging to the same gene family (isoforms) and employed weighting factors to convert the TPM value of the gene corresponding to the protein to the appropriate initial protein value. The TPM values are shown in Table 2.3.4.

**Table 2.3.4**: The list of genes used to estimate the initial protein value in the mathematical model and the corresponding transcripts per million (TPM) values.

| Gene symbol | TPM (mean) | TPM (SD) |
|---|---|---|
| TGFBR1 | 64.76 | 2.24 |
| TGFBR2 | 95.81 | 4.21 |
| SMAD7 | 20.62 | 3.33 |
| FOS | 1.17 | 0.62 |
| THBS1 | 4522.39 | 40.42 |
| FMOD | 20.88 | 0.66 |
| FLT1 | 101.53 | 1.82 |
| KDR | 0.02 | 0.02 |
| GRB2 | 128.45 | 0.34 |
| SHC1 | 401.13 | 8.79 |
| SHC2 | 1.16 | 0.49 |
| SHC3 | 4.28 | 0.38 |
| SHC4 | 1.26 | 0.30 |
| PIK3CA | 16.36 | 0.80 |
| PIK3CB | 15.10 | 0.89 |
| PIK3CD | 32.27 | 1.57 |
| PIK3CG | 0.00 | 0.00 |

| | | |
|---|---|---|
| PTEN | 51.20 | 1.38 |
| RASA1 | 85.47 | 4.19 |
| RASA2 | 26.93 | 0.49 |
| RASA3 | 92.99 | 3.57 |
| GAB1 | 7.09 | 0.54 |
| SOS1 | 25.34 | 1.14 |
| SOS2 | 20.01 | 0.81 |
| AKT1 | 84.62 | 2.25 |
| AKT2 | 41.27 | 0.82 |
| HRAS | 101.55 | 4.41 |
| KRAS | 42.43 | 1.21 |
| NRAS | 113.71 | 3.80 |
| ARAF | 85.60 | 1.46 |
| BRAF | 4.73 | 0.20 |
| RAF1 | 79.97 | 1.25 |
| MAP2K1 | 73.15 | 1.57 |
| MAP2K2 | 114.17 | 3.90 |
| PTPN1 | 84.13 | 3.12 |
| MAPK1 | 78.20 | 1.11 |
| MAPK3 | 75.96 | 5.75 |

***Sensitivity Analysis***

The sensitivity coefficient Sy was calculated using the following equation [68,88]:

$$\mathrm{Sy} = \partial \ln \mathrm{M} / \partial \ln y_j$$

where M is the signaling metric, i.e., the integral expression level of THBS1 with TGF-β1 stimulation, and $y_j$ is each nonzero species in the mechanistic model. The sensitivity coefficients were calculated by finite difference approximations with 1% changes in the biochemical reactions. To calculate the sensitivity coefficients, I used BioMASS with run_analysis = (target="reaction", metric="integral", style="heatmap").

***Time-course PI3K-Akt Inhibitor Treatment***

I validated the model results using HFF-1 cell experiments with additional inhibitors at each time-point (four time-points, up to 48 h) as previously described [76]. Briefly, HFF-1 cells were seeded in 96-well plates with DMEM at 10,000 cells/well. The cells were treated with either control

(DMEM with 0.1% DMSO supplemented with 2% FBS) or 4 ng/mL TGF-β1 (R&D Systems). Inhibitors for TGF-β1-treated samples were added at 0 h, 8 h, 24 h, and 32 h. Supernatants were collected at 48 h for quantification. Reconstitution buffer (0.1% BSA in 4 mM HCl PBS, R&D Systems) was used as vehicle. Supernatants were centrifuged (13,000 rpm, 15 min, 4°C) to remove cell debris and used for FMOD ELISA (Abcam). The following inhibitors were used: LY364947 (123-05981, Fujifilm) and Akt inhibitor VIII (14870, Cayman Chemical)

***Sample preparation for THBS1 and FMOD quantification with TGF-β family***

HFF-1 cells were used to prepare recombinant human TGF-β family treated lysates and supernatants for quantification as previously described [76]. Briefly, cells for were seeded in 6-well plates at 200,000 cells/well. After treatment with either control (DMEM with vehicle supplemented with 2% FBS), TGF-β1 (R&D Systems), TGF-β2 (ProteinTech), or TGF-β3 (ProteinTech), cell lysates and supernatants were collected after 48 h for quantification by WB or FMOD ELISA (Abcam).

***Sample Preparation for FMOD Quantification with VEGF, EGF, b-FGF, or PDGF-BB***

HFF-1 cells were used to prepare recombinant human VEGF, EGF, b-FGF, or PDGF-BB supernatants for FMOD ELISA as previously described [76]. Briefly, cells for were seeded in 12-well plates at 100,000 cells/well. After treatment with either control (DMEM with vehicle supplemented with 2% FBS), VEGF (ProteinTech), EGF (PeproTech), b-FGF (R&D Systems), or PDGF-BB (ProteinTech), cell supernatants were collected after 48 h for quantification by FMOD ELISA (Abcam).

***Time-Course TGF-β1 Washout Experiment***

TGF-β1-stimulated HFF-1 cells was washed with PBS at seven time-points (i.e., 1 h, 2 h, 4 h, 8 h, 12 h, 24 h, and 48 h or 15 min, 30 min, 1 h, 4 h, 12 h, 24 h, and 48 h) to confirm the effects of transient and sustained TGF-β1 stimulation on the expression of THBS1, FMOD, and phosphorylated Akt (Ser473) as previously described [76]. Briefly, HFF-1 cells were seeded in 6-well plates with DMEM at 200,000 cells/well. After serum starvation for 16 h, cells were treated with control (DMEM with 2% FBS-added vehicle) or 4 ng/mL TGF-β1. Cells were washed with PBS and replaced with control medium at each time-point from the TGF-β1 stimulation condition, and all lysate was recovered at 48 h for western blot analysis.

***Natural Compound Screening for THBS1 Regulation***

HFF-1 cells (PDL 24) were seeded in 96-well plates with DMEM at a density of 10,000 cells/well. The cells were treated with control (DMEM with 2% FBS and 0.1% DMSO vehicle), 4 ng/mL

TGF-β1, or 4 ng/mL TGF-β1 combined with compounds from a natural bioactive substance library (S990043-NAT1 to 4, Sigma, 268 compounds in total) as previously described [76]. After 48 h of the treatment, the cells were treated with the Cell Counting Kit-8 solution (DOJINDO), followed by incubation for 1 h. Cell viability was calculated at an absorbance wavelength of 450 nm using the Multiskan FC system (Thermo Fisher Scientific). Additionally, the supernatants were collected to perform the ELISA of THBS1 (DTSP10-1, R&D Systems) according to the manufacturer's protocol. Briefly, the supernatants were centrifuged (1, 000 rpm, 4 min, and 4°C) to remove cell debris and used for each measurement (n = 1). Relative protein levels were shown relative to TGF-β1 as indicated by (1) value. Natural compounds showing >80% cell viability were tested for THBS1 ELISA.

***THBS1 ELISA for Retinol and ATRA***

HFF-1 cells (PDL 24) were seeded in 6-well plates with DMEM at a density of 200,000 cells/well. The cells were pretreated with 0.1% DMSO or each retinoid (retinol or ATRA) in 0.1% FBS DMEM for 1 h before each treatment. The cells were treated with control (DMEM with 2% FBS and 0.1% DMSO vehicle), 4 ng/mL TGF-β1, 5 μM LY36494 with or without 4 ng/mL TGF-β1, 0.5 μM or 5 μM retinol (LKT Labs) with or without 4 ng/mL TGF-β1, or 0.5 μM or 5 μM ATRA with or without 4 ng/mL TGF-β1. After 48 h of the treatment, the supernatants were collected for THBS1 ELISA (R&D Systems), and ELISA was performed according to the manufacturer's protocol. Briefly, the supernatants were centrifuged (1, 000 rpm, 4 min, and 4°C) to remove cell debris and used for each measurement (n = 3). Relative protein levels were shown relative to TGF-β1 as indicated by (1) value.

***Sample Preparation for THBS1 and Lamin-B1 Quantification with TEAD Inhibitor Treatment***

HFF-1 cells (PDL 47) were seeded at a density of 200,000 cells/well in 6-well plates supplemented with 10% FBS/DMEM. The cells were serum-starved with 0.1% FBS for 24 h and pretreated with 0.1% DMSO or 5 μM ATRA for 1 h before each treatment. The cells were treated with control (DMEM with 2% FBS and 0.1% DMSO vehicle), 1 μM K-975 (Selleck) with or without 5 μM ATRA, cultured for 48 h, and lysates were collected after 48 h for quantification by western blotting.

***THBS1 Immunofluorescence Imaging***

The distribution of THBS1 expression in HFF-1 was examined by immunofluorescence imaging as previously described [76]. Briefly, HFF-1 cells were seeded in 24-well plates with DMEM at 20,000 cells/well. After serum starvation for 16 h, cells were treated with control (DMEM with 2% FBS-added vehicle), 0.04 ng/mL, or 0.2 ng/mL TGF-β1 for 48 h and fixed with fresh 4%

paraformaldehyde (Thermo Fisher Scientific) in PBS for 15 min (n = 6). After rinsing with PBS, the cells were subjected to a 0.2% TritonX-100 (Nakalai Tesque) in PBS for 10 min and blocked using 1% goat serum (Thermo Fisher Scientific) in PBS overnight. Next, cells were incubated with THBS1 antibodies (ab85762, Abcam) diluted in 1% goat serum in PBS overnight and washed with PBS. Finally, cells were incubated with Alexa Fluor® 594 conjugated secondary antibodies (Abcam), CellMask™ (Thermo Fisher Scientific) for cell body staining, and Hoechst® 33342 (DOJINDO) for nuclear staining for 1 h at 25 °C in the dark. Fluorescence images of 96 fields (16 fields per well) under each condition were acquired using IN Cell Analyzer 2500HS (Cytiva). CellProfiler (ver. 4.2.1) was used to segment nuclear regions from Hoechst® 33342 images and cytoplasmic regions by excluding nuclear regions from CellMask™ images. The THBS1 signal intensity of each cell was then quantified in the cytoplasmic region; THBS1 signal intensity was calculated based on the integrated and mean signal density in each image.

***SMAD4 Immunofluorescence Imaging***

SMAD4 expression distribution in HFF-1 cells was examined by immunofluorescence imaging. Briefly, HFF-1 cells (PDL 24) were seeded in 24-well plates with DMEM at a density of 20,000 cells/well. After serum starvation for 24 h, the cells were treated with control (DMEM with 2% FBS and vehicle), 4 ng/mL TGF-β1, 5 μM LY36494 with or without 4 ng/mL TGF-β1, or 5 μM ATRA with or without 4 ng/mL TGF-β1 for 15 min and fixed with fresh 4% paraformaldehyde (15710, Electron Microscopy Science) in PBS for 15 min. After rinsing with PBS, the cells were subjected to 0.2% Triton X-100 (Nakalai Tesque) in PBS for 10 min and blocked with 1% goat serum (Thermo Fisher Scientific) in PBS overnight. Next, the cells were incubated with SMAD4 antibodies (CST), diluted with 1% goat serum in PBS overnight, and washed with PBS. Finally, the cells were incubated with anti-rabbit Alexa Fluor® 488-conjugated secondary antibodies (Abcam). CellMaskTM (Thermo Fisher Scientific) was used for cell body staining, whereas Hoechst® 33342 (DOJINDO) was used for nuclear staining for 1 h at 25°C in the dark. Fluorescence images of 30 fields under each condition were acquired using the IN Cell Analyzer 2500HS (Cytiva). CellProfiler was used to segment nuclear regions from the Hoechst® 33342 images. The SMAD4 signal intensity of each cell was quantified in the nuclear region and calculated based on the integrated signal density in each image.

***Effect of Surface Stiffness on Drug Sensitivity***

CytoSoft® 6-well plates (Advanced BioMatrix) were purchased for culturing on substrates of various stiffnesses (0.5, 2, 8, 16, and 32 kPa). Following the manufacturer's instructions, 100 μg/mL of PureCol Atelocollagen Solution (Advanced BioMatrix), a type I collagen, was prepared by diluting with degassed PBS (37°C). The collagen solution was added to each well and

incubated at RT for 1 h. After washing with PBS, the cells were seeded and used in further experiments. Briefly, HFF-1 cells (PDL 47) were seeded in 6-well plates with 10% FBS DMEM at a density of 150,000 cells/well. The cells were serum-starved with 0.1% FBS for 24 h, followed by their treatment with control (DMEM with 2% FBS and 0.1% DMSO vehicle), 5 μM ATRA, or 1 μM K-975 for 48 h and processed for SA-β-gal staining as previously described in the SA-β-gal Staining subsection.

***Western Blot Analysis***

All immunoblots are representative images of three biological replicates as previously described [76]. Attached cells were washed with PBS and lysed in RIPA buffer (Thermo Fisher Scientific) supplemented with Halt™ Protease and Phosphatase Inhibitor (Thermo Fisher Scientific). Cell lysates were centrifuged (13,000 rpm, 15 min, 4°C) to unify protein concentrations between samples, and a BCA protein assay kit (Thermo Fisher Scientific) was used according to the manufacturer's protocol. Proteins were separated by SDS-PAGE and transferred to nitrocellulose membranes using iBlot2 (Thermo Fisher Scientific). After blocking with EveryBlot blocking buffer (Bio-Rad), the following antibodies were used for blotting: anti-THBS1 (37879, CST), anti-FMOD (60108-1-Ig, ProteinTech), anti-LAMIN-B1 (12987-1-AP, ProteinTech), anti-p53 (2524, CST), anti-p21 (2946, CST), anti-c-Fos (2250, CST), anti-c-Jun (9165, CST), anti-SMAD2 (5339, CST), anti-phosphorylated SMAD2 (Ser465/467; 3108, CST), anti-SMAD3 (9523, CST), anti-phosphorylated SMAD3 (Ser423/425; 9520, CST), anti-SMAD4 (46535, CST), anti-phosphorylated Akt (Ser473; 9271, CST), anti-pan Akt (2920, CST), anti-USP11 (ab109232, Abcam), anti-GAPDH (M171-3, Medical & Biological Laboratories), and anti-GAPDH (10494-1-Ap, ProteinTech). Primary antibodies were reacted at 4°C overnight, while secondary antibodies were reacted at room temperature for 1 h. For protein detection, Clarity Istern ECL Substrate (Bio-Rad) or Clarity Max Istern ECL Substrate (Bio-Rad) was used with an Amersham Imager 680 (GE Healthcare). Relative protein quantification was performed with ImageJ Fiji. Expression values (n = 3) were normalized using GAPDH as loading control and the ratio against the control was calculated. Molecular weights are indicated on the left of each image.

***ELISA***

All ELISAs were conducted according to the manufacturer's protocol as previously described [76]. Cell supernatants were used as samples for ELISAs for THBS1, FMOD, TGF-β1, VEGF, EGF, b-FGF, PDGF, IL-6, and IL-8. Briefly, supernatant samples were centrifuged (1,000 rpm, 4 min, 4°C) to remove cell debris and used for each measurement. Cell lysates were used as samples for the ELISA for SMAD2, SMAD3, and SMAD4. Lysate samples were collected using lysis buffer included in the kits, cell lysates were centrifuged (13,000 rpm, 15 min, 4°C) and used for

each ELISA. Relative expression levels are displayed with the control (1) value. The following ELISA kits were used for quantification: THBS1 (DTSP10-1, R&D Systems), FMOD (ab275895, Abcam), TGF-β1 (DB100B, R&D Systems), VEGF (DVE00, R&D Systems), IL-6 (D6050, R&D Systems), IL-8 (ab214030, Abcam), SMAD2 (ab260065, Abcam), SMAD3 (ab264624, Abcam), and SMAD4 (ab253211, Abcam).

***Quantitative RT-PCR (qRT-PCR) Analysis***

Total RNA from HFF-1 cells was prepared using the NucleoSpin RNA kit (Macherey-Nagel GmbH & Co.) and subjected to complementary DNA (cDNA) synthesis using ReverTra Ace® qPCR RT Master Mix (Toyobo Life Science) as follows: 15 min at 37°C, 5 min at 50°C, and 5 min at 98°C [76]. Quantitative PCR using cDNA was conducted using a KOD SYBR qPCR kit (Toyobo Life Science) with a CFX96 Real-Time PCR System (Bio-Rad) according to the manufacturer's protocol. PCR cycling conditions were as follows: 40 cycles of 10 s at 98°C, 10 s at 60°C, and 30 s at 68°C. The primers used for qRT-PCR were as follows: THBS1 (5′-TCCCCATCCAAAGCGTCTTC-3′ and 5′-ACCACGTTGTTGTCAAGGGT-3′); FMOD (5′-GGACGTGGTCACTCTCTGAA-3′ and 5′-GGCTCGTAGGTCTCATACGG-3′); GAPDH (5′-GTCTCCTCTGACTTCAACAGCG-3′ and 5′-ACCACCCTGTTGCTGTAGCCAA-3′). Gene expression was quantified using the ΔΔCq method. Expression values (n = 3) were normalized using GAPDH and the ratio against the PDL 24 value was calculated.

***Quantification and Statistical Analysis***

Statistical data are presented as the mean with standard deviation (SD), calculated using the "sd" function in R. The horizontal line in the center of the box plot is the median, the lower and upper borders indicate the 25$^{th}$ and 75$^{th}$ percentiles, respectively, and all measurements are shown as point plots. For detection of upstream regulators, the right-tailed Fisher's exact test was used in IPA. Comparisons of more than two groups were made using one-way Dunnett's or Tukey's multiple comparisons test. Comparisons of two groups were evaluated by Student's *t*-test, Ilch's *t*-test, or Wilcoxon rank sum test. The Silverman test was used to test for multimodality. I considered $p < 0.05$ to be statistically significant. Unless otherwise noted, p-values were calculated using the multcomp package in R. The statistical details of each experiment can be found in the figure legends.

# 3. RESULTS

## 3.1 Identification of Skin Aging Target Through Omics Analyses and Mathematical Modeling

### 3.1.1 Cellular Senescence Induced by Replication-Stress (RS) Using HFF-1 and BJ Cells

To identify global transcriptional signatures and their regulatory mechanisms in dermal fibroblast senescence, I performed RNA-seq, ChIP-seq (for H3K27Ac modification), and ATAC-seq of RS induced HFF-1 cells from different PDLs – early (PDL 24), middle (PDL 36), and late (PDL 47) [76]. First, HFF-1 and BJ, a different cell line of human dermal fibroblasts, were maintained from early (HFF-1: PDL 13, BJ: PDL 23) to late (HFF-1: PDL 53, BJ: PDL 61) PDL to induce RS (Figure 3.1.1A). I examined the activities of p53, p21, and SA-β-gal for different PDLs of fibroblast cells (HFF-1: Figure 3.1.1B, 3.1.1C; BJ: Figure 3.1.1D, 3.1.1E). Slower cell proliferation was observed with increased PDL in HFF-1 cells (Figure 3.1.1F). RS-induced cellular senescence was promoted by increased PDL in both cell lines. To explain the decline of p21 in PDL 53 in HFF-1 cells (Figure 3.1.1B), I focused on USP11—a deubiquitylase that stabilizes p21 protein and prevents its degradation [89]—and observed a significant decrease in USP11 expression with increased PDL in HFF-1 cells (Figure 3.1.1G). This result suggests that the stability of the p21 protein may decrease due to the decrease in USP11.

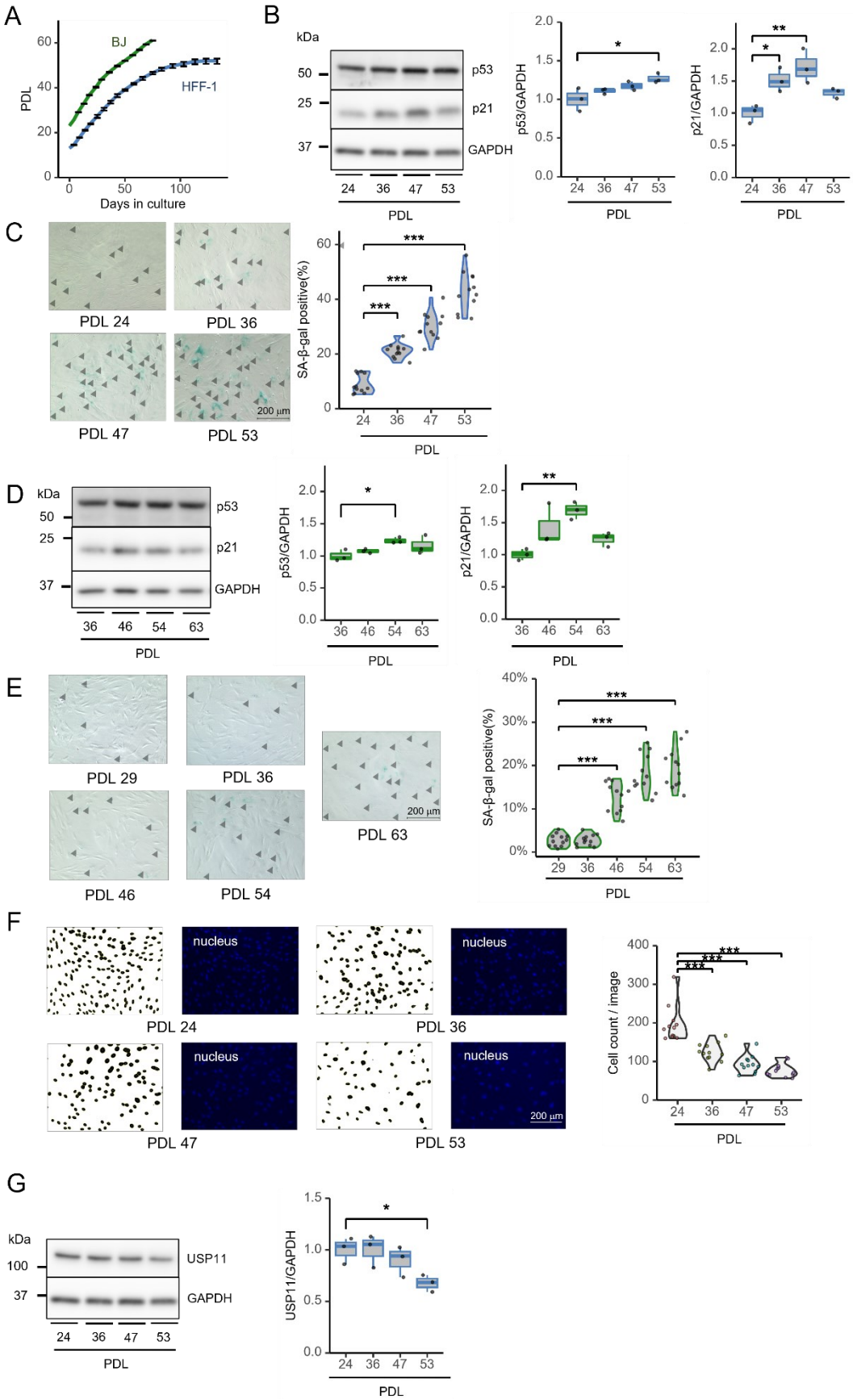
A
BJ
HFF-1
PDL
Days in culture
B
kDa
p53
p21
GAPDH
PDL
p53/GAPDH
p21/GAPDH
C
PDL 24
PDL 36
PDL 47
PDL 53
200 μm
SA-β-gal positive(%)
D
E
PDL 29
PDL 46
PDL 54
PDL 63
F
nucleus
Cell count / image
G
USP11
USP11/GAPDH

**Figure 3.1.1**: Cellular senescence induced by RS using HFF-1 and BJ cells [76].

A) Growth curve of HFF-1 (blue line) and BJ cells (green line); n = 3, mean ± SD.

B) Western blot (WB) of p53 and p21 in RS-induced HFF-1 cells. Cells were cultured for 48 h, and lysates were analyzed. (Left panel) Representative image. (Middle panel) Quantification of p53 expression; n = 3, *p < 0.05 (Dunnett's test). (Right panel) Quantification of p21 expression; n = 3, *p < 0.05, **p < 0.01 (Dunnett's test).

C) (Left panel) SA-β-gal staining of RS-induced HFF-1 cells. Representative images. SA-β-gal-positive cells are indicated by black arrowheads; scale bar: 200 μm. (Right panel) Quantification of SA-β-gal: SA-β-gal-positive rate (%) = number of SA-β-gal positive cells / total number of cells × 100. Four images per well were randomly analyzed from three wells (total of 12 images/PDL), ***p < 0.001 (Dunnett's test).

D) WB of p53 and p21 in RS-induced BJ cells. Cells of each PDL (PDL 36, PDL 46, PDL 54, PDL 63) were cultured for 48 h and the lysates were analyzed. (Left panel) Representative image. (Middle panel) Quantification of p53 expression; n = 3, *p < 0.05. (Dunnett's test). (Right panel) Quantification of p21 expression; n = 3, **p < 0.01 (Dunnett's test).

E) (Left panel) SA-β-gal staining of RS-induced BJ cells. Representative image. SA-β-gal-positive cells for each PDL (PDL 29, PDL 36, PDL 46, PDL 54, PDL 63) are indicated with black arrowheads; scale bars: 200 μm. (Right panel) Quantification of SA-β-gal: SA-β-gal-positive rate (%) = number of SA-β-gal-positive cells / total number of cells × 100. Four images from each of the three wells were analyzed (total 12 images/condition), ***p < 0.001 (Dunnett's test).

F) Cell counting with Hoechst® 33342 in RS-induced HFF-1 cells. Cells from each PDL (PDL 24, PDL 36, PDL 47, PDL 53) were cultured for 48 h and the number of nuclei were counted. (Left panel) Representative image. Each image was processed using Image J. (Right panel) Quantification of cell count per image of each PDL. Four images from each of the three wells were analyzed (total of 12 images/PDL), ***p < 0.001 (Dunnett's test).

G) WB of USP11 in RS-induced HFF-1 cells. Cells of each PDL (PDL 24, PDL 36, PDL 47, PDL 53) were cultured for 48 h, and lysates were analyzed. (Left panel) Representative image. (Right panel) Quantification of USP11 expression; n = 3, *p < 0.05 (Dunnett's test).

### 3.1.2 Multi-omics analysis reveals TGF-β1 as a potential regulator of skin aging

To identify transcription factors (TFs) that regulate senescence in HFF-1 cells, the TF enrichment score was calculated from the gene expression of each PDL using DoRothEA analysis [90], and the top 20 TFs were determined based on the enrichment score (Figure 3.1.2A) [76]. The downstream TFs of the TGF-β pathway, SMAD3 (PDL 24 vs. PDL 36: $p < 0.01$, PDL 24 vs. PDL 47: $p < 0.05$) and SMAD4 (PDL 24 vs. PDL 36: $p < 0.05$, PDL 24 vs. PDL 47: $p=0.057$), were

enriched with increasing PDL. I also identified known senescence-associated TFs, including JUNB [91], GATA6 [92], TP53 [93], TEAD1 [91], and E2F4 [91]. To elucidate the TF network of DEGs related to the cellular senescence of skin fibroblasts, I also identified TFs regulating upregulated and/or downregulated DEGs with increasing PDLs using Lisa [94] (Figure 3.1.2B). SMAD3 was identified as a highly enriched TF that regulates genes whose expression was altered (upregulated or downregulated) with increasing PDLs. These results suggest that SMAD is an important factor in cellular senescence in dermal fibroblasts in passaging culture. When the TGF-β ligand binds to type I and type II serine/threonine kinase receptors on the cell surface, the TGF-β signaling pathway is activated [95]. The type II receptor phosphorylates and activates the type I receptor, which then phosphorylates SMAD2 or SMAD3, thereby forming a complex with SMAD4 that translocates to the nucleus and regulates gene transcription [95].

To confirm whether SMAD motifs indeed played an important role with cellular senescence, I performed a TF motif enrichment analysis using HOMER [96], by assessing the gained ATAC peaks—the open chromatin regions specifically enriched for late PDL (Figure 3.1.2C) [76]. As a result, I found that SMAD2 (–log[adj-p]: 15.8) and SMAD4 (–log[adj-p]: 10.3) were associated with the gained ATAC peaks. Next, I analyzed whether TGF-β is the upstream regulator of cellular senescence in dermal fibroblasts from 93 overlapping differentially expressed genes (DEGs) identified in the RNA-seq, differential ATAC peaks, and differential H3K27Ac peaks (Figure 3.1.2D) between PDL 24, PDL 36, and PDL 47. TGF-β1 was identified as the top regulator among the overlapping DEGs. From the 294 common DEGs between ChIP-seq of H3K27Ac, a histone marker indicating active promoter and enhancer regions, and RNA-seq, TGF-β1 was identified as the most enriched upstream regulator of DEGs associated with cellular senescence (Figure 3.1.2E). These results indicate that the TGF-β1–SMAD axis with epigenetic changes can be activated in RS-induced dermal fibroblasts.

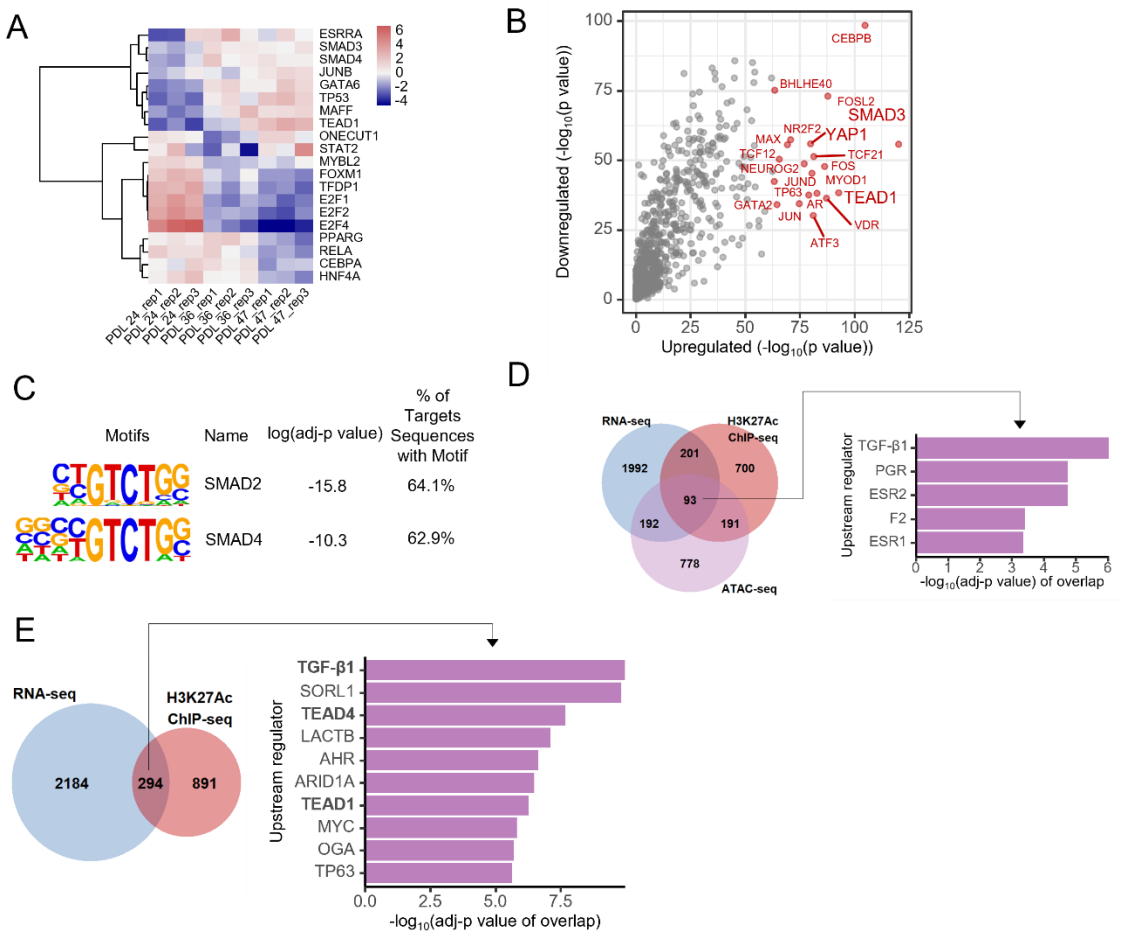


**Figure 3.1.2**: Multi-omics analysis reveals TGF-β1 as a potential regulator of skin aging [76].

A) Transcription factor (TF) enrichment analysis of RNA-seq data derived from RS-induced HFF-1 cells of top 20 TFs (see details in Methods section). Heatmap shows the normalized TF enrichment scores calculated using the DoRothEA analysis.

B) TF network analysis of differentially expressed genes (DEGs; |fold change (FC)| > 1.2, adj-p < 0.05) between PDL 24, PDL 36, and PDL 47 using Lisa. The top 20 TFs are highlighted in red.

C) Enriched motifs in the gained ATAC-seq peaks with increase of PDL. Log (adj-p value) and proportion of target sequences with motif was calculated using the "findMotifsGenome.pl" function of HOMER.

D) (Upper panel) Venn diagram showing RNA-seq differentially expressed genes (DEGs; blue sphere; |FC| > 1.2, adj-p < 0.05), genes annotated from ATAC differential peaks (purple sphere; $|\log_2 FC| > 0$, adj-p < 0.05), and genes annotated from H3K27Ac differential peaks (red sphere; $|\log_2 FC| > 0$, adj-p < 0.05) between PDL 24, PDL 36, and PDL 47. The number of genes in each condition is shown in the Venn diagram. (Lower panel) The top five upstream regulators found using Ingenuity Pathway Analysis (IPA) are shown with

epigenetic-linked DEGs (93 genes). A right-tailed Fisher's exact test and the Benjamini–Hochberg (BH) method were used to calculate $-\log_{10}$(adj-p) of the overlap.

E) (Left panel) Venn diagram showing RNA-seq of DEGs (blue sphere; $|FC| > 1.2$, adj-p $< 0.05$) and genes annotated from H3K27Ac differential peaks (red sphere; $|\log_2 FC| > 0$, adj-p $< 0.05$) between PDL 24, PDL 36, and PDL 47. The number of genes in each condition is shown in the Venn diagram. (Right panel) The top ten upstream regulators found by performing the ingenuity pathway analysis are shown with epigenetic-linked DEGs (294 genes). A right-tailed Fisher's exact test and the BH method were used to calculate $-\log_{10}$(adj-p) of the overlap.

### 3.1.3 TGF-β1 is an upstream factor in aging and cellular senescence, affecting THBS1 and FMOD expression, positive and negative regulators of TGF-β signaling, through epigenetic changes

To further confirm the involvement of TGF-β1 in skin aging and senescence, two additional independent public RNA-seq datasets were analyzed [76]: *in vivo* data for primary human dermal fibroblasts [78] representing a wide age range (11–71 years of age, see donor list in Table 2.3.1), to analyze external factors, and *in vitro* data for HFF-1 cells over a long-term passage [77], to analyze internal factors (PDL 16–74, five PDL points). For *in vivo* data, I obtained three clusters of donors based on whole gene expression data and identified DEGs among the clusters (Figure 2.3.1). For *in vitro* data, DEGs between each PDL were identified. The number of overlapping DEGs in both datasets corresponded to 592 downregulated and 502 upregulated genes (Figure 3.1.3A). Functional analysis of overlapping gene sets using the Kyoto Encyclopedia of Genes and Genomes (KEGG) database [97] revealed that the cell cycle and TGF-β signaling pathways were enriched in both datasets. In addition, TGF-β1 was identified as the top regulator for the upregulated gene set by upstream analysis of the overlapping gene sets (Figure 3.1.3B). In fact, the RNA-seq expression of *TGFB1* was upregulated with the increase in PDL (Figure 3.1.3C). Comparisons between gene expression and *in vivo* age or *in vitro* PDL revealed that *THBS1* and *FMOD* expression were strongly correlated with skin aging (*in vivo*) and senescence (*in vitro*) ($R^2$=0.29) (Figure 3.1.3D). In both data, THBS1 and FMOD show the same time-course dynamics with *in vivo* age and *in vitro* PDL (Figure 3.1.3E, 3.1.3F). Further, the expression of the TGF-β receptor, *TGFBR1*, and *TGFB3* was also correlated with gene expression levels both *in vivo* and *in vitro*, indicating that TGF-β signaling is more likely to be activated in skin aging. As THBS1 has been associated with aging in other organs [98] and FMOD is responsible for cross-linking of collagen [99]—which decreases with age in skin tissue [8]—I focused on TGF-β1, THBS1, and FMOD for further analysis. Note that, while my RNA-seq data using HFF-1 cells showed a decrease in FMOD with senescence and TGF-β1 treatment (Figure 3.1.3G), public *in vitro* RNA-

seq77 using the same HFF-1 cell line showed an opposite trend, i.e., increase of FMOD with senescence (Figure 3.1.3F). To investigate the effects of modulation of TGF-β1, THBS1, and FMOD, I obtained RNA-seq and ATAC-seq of TGF-β1 treated HFF-1 cells (Figure 3.1.3H). Altered expression levels and peak changes in THBS1 and FMOD were observed in the datasets. These results indicated that TGF-β1 is an upstream factor in aging and cellular senescence, affecting THBS1 and FMOD expression through epigenetic changes.

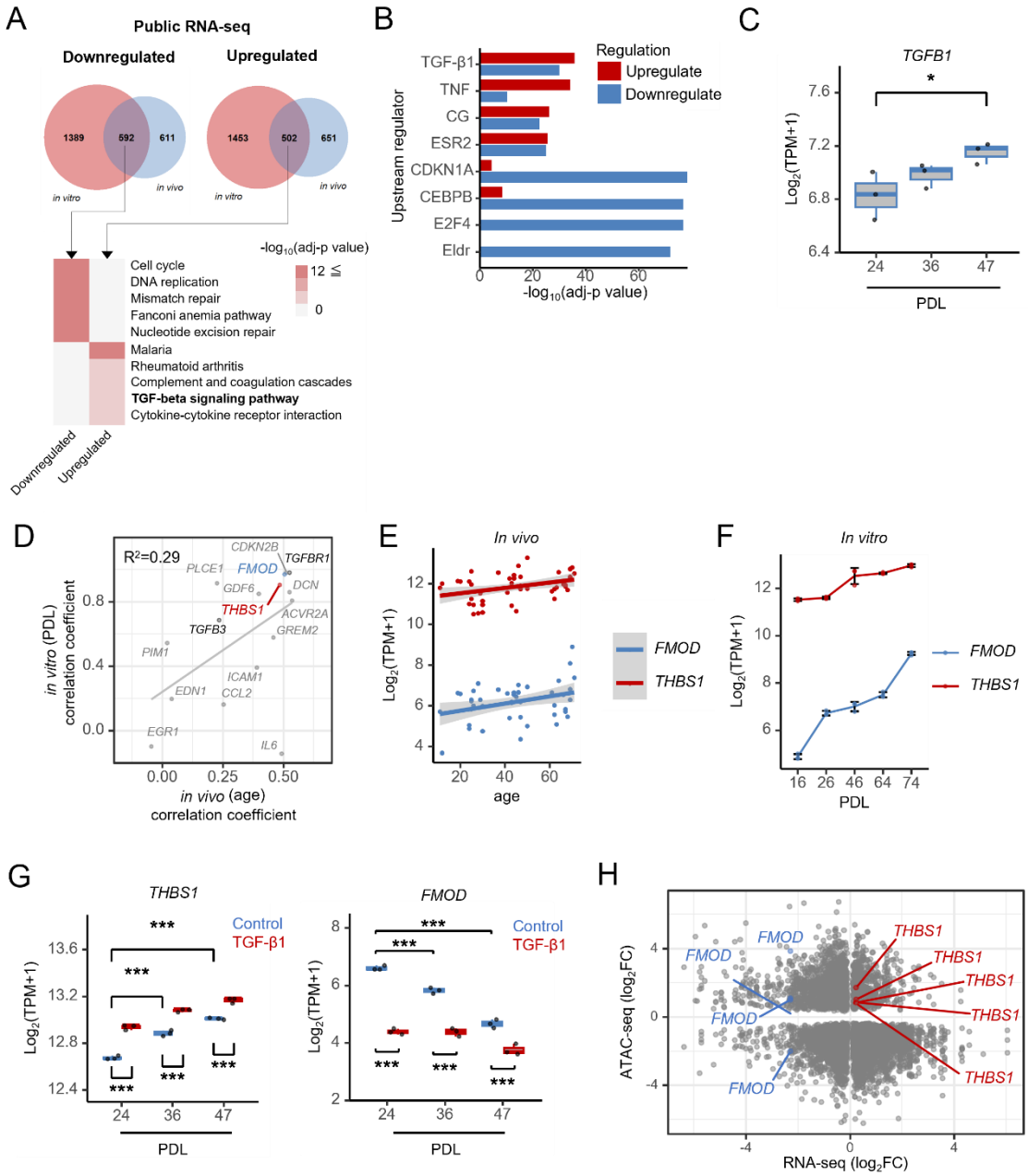


**Figure 3.1.3**: Positive and negative regulators of TGF-β signaling, THBS1 and FMOD, identified as critical factors regulating skin aging and dermal fibroblast senescence [76].

A) (Upper panel) Venn diagram showing the public *in vitro* DEGs (blue sphere) and *in vivo*

DEGs (red sphere). (Lower panel) Heat map showing top five pathways annotated in the pathway enrichment analysis (Kyoto Encyclopedia of Genes and Genomes [KEGG]). The adj-p was calculated using "compareCluster" of clusterProfiler.

B) Upstream regulators in common genes between the public *in vitro* and *in vivo* datasets. The top four upstream regulators of 592 downregulated (blue) and 502 upregulated (red) genes are shown with colored bars. A right-tailed Fisher's exact test and the Benjamini–Hochberg (BH) method were used to calculate $-\log_{10}$(adj-p) of the overlap.

C) Quantification of RNA-seq expression data from RS-induced HFF-1 cells (blue) for *TGFB1*. Gene expression was normalized to $\log_2$(transcripts per million [TPM] + 1); n = 3, ***p < 0.001 (Dunnett's test).

D) Correlation coefficient between the public *in vitro* (PDL), public *in vivo* (age), and gene expression data. The genes associated with KEGG term "TGF-beta signaling pathway" in Figure 1H are plotted. Spearman correlations were calculated using the "cor" function of R software; *THBS1* (red) and *FMOD* (blue). $R^2$ was calculated using the "ggpmisc::stat_poly_eq" function.

E) Public *in vivo* time-course expression data[27] for *THBS1* and *FMOD*. Gene expression was normalized to $\log_2$(TPM + 1); n = 45 (age: 11–71 years; see donor list in Table S1). Linear regression lines were added using 'geom_smooth' (method = "lm").

F) Public *in vitro* time-course expression data[26] for *THBS1* and *FMOD*. Gene expression was normalized to $\log_2$(TPM + 1); n = 3, mean ± SD.

G) RNA-seq expression data for *THBS1* and *FMOD* in RS-induced and TGF-β1-stimulated HFF-1 cells (control: blue; 4 ng/mL TGF-β1: red). Gene expression was normalized to $\log_2$(TPM + 1). (Left panel) Quantification of THBS1; n = 3, ***p < 0.001 (Tukey's multiple comparisons). (Right panel) Quantification of FMOD; n = 3, ***p < 0.001 (Tukey's multiple comparisons).

H) Correlation between the expression FC (control vs. 4 ng/mL TGF-β1; adj-p < 0.05) of RNA-seq and peak FC (control vs. 4 ng/mL TGF-β1; adj-p < 0.05) of ATAC-seq; *THBS1* (red) and *FMOD* (blue). FC and adj-p were calculated using DESeq2.

### 3.1.4 THBS1 and FMOD identified as critical factors regulating skin aging and dermal fibroblast senescence

The percentage of TGF-β1-positive fibroblasts in the human dermis increases with age [100]. Higher PDL corresponded with higher TGF-β1 expression in HFF-1 cells (Figure 3.1.4A). Istern blot (Figure 3.1.4B), qPCR (Figure 3.1.4C), and enzyme-linked immunosorbent assay (ELISA) analyses (Figure 3.1.4D) revealed an increased and decreased expression of THBS1 and FMOD, respectively, in higher cell passages of dermal fibroblasts. The expression of THBS1 was

confirmed to increase with age in human dermal tissue isolated from female donors (23–63 years of age; Figure 3.1.4E, see Table 2.2.1 for donor list) [76]. From the same donors, p21 expression was also confirmed to increase with age, suggesting that my model of cellular senescence induced by long-term passaged culturing accurately captured changes in human skin-factors associated with aging. It is worth noting that THBS1 was not detected in the epidermis, suggesting that THBS1 functions in the dermis during skin aging. Interestingly, using publicly available transcriptome data [78] (see Table 2.3.2 for donor list), *THBS1* expression was found to be increased in patients with HGPS (2–8 years of age) compared to that in healthy donors (1–9 years of age) of the same age (Figure 3.1.4F). The results from my data-driven analysis identified the TGF-β1–SMAD signaling pathway along with THBS1 and FMOD expression as critical factors regulating skin aging and dermal fibroblast senescence.

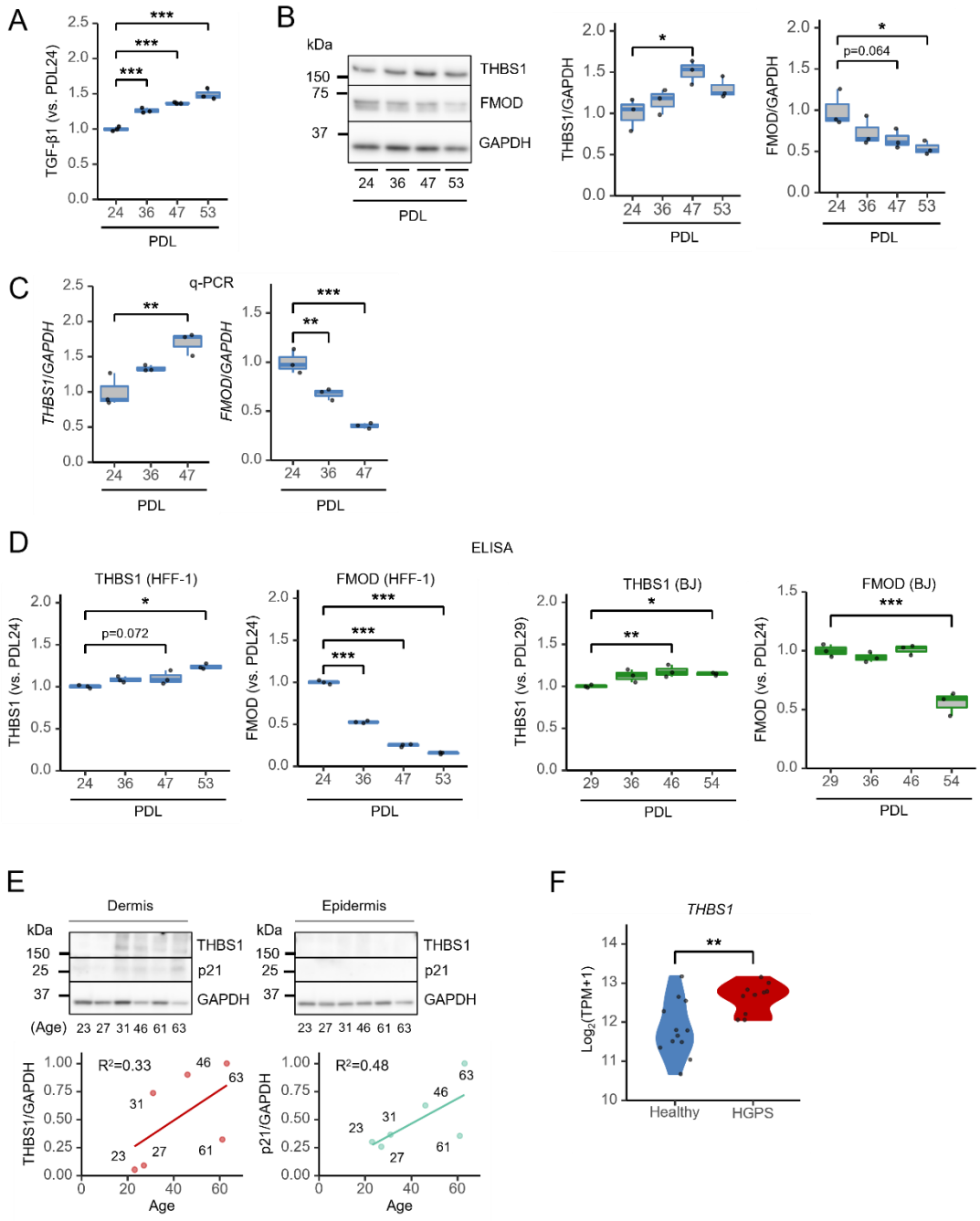


**Figure 3.1.4**: THBS1 and FMOD identified as critical factors regulating skin aging and dermal fibroblast senescence [76].

A) TGF-β1 enzyme-linked immunosorbent assay (ELISA) in RS-induced HFF-1 cell supernatants. Cells were cultured for 48 h, and supernatants were analyzed; n = 3, ***p < 0.001 (Dunnett's test).

B) WB analysis of THBS1 and FMOD in RS-induced HFF-1 cells. Cells were cultured for 48 h, and lysates were analyzed. (Left panel) Representative image. (Middle panel)

Quantification of THBS1 expression; n = 3, *p < 0.05 (Dunnett's test). (Right panel) Quantification of FMOD expression; n = 3, *p < 0.05 (Dunnett's test).

C) q-PCR analysis of RS-induced HFF-1 cells. (Left panel) Quantification of THBS1; n = 3, **p < 0.01 (Dunnett's test). (Right panel) Quantification of FMOD; n = 3, **p < 0.01, ***p < 0.001 (Dunnett's test).

D) THBS1 and FMOD ELISA of RS-induced HFF-1 (blue) and BJ (green) cell supernatants. Cells were cultured for 48 h and supernatants were analyzed. (Left) Quantification of THBS1 in HFF-1 cells; n = 3, *p < 0.05 (Dunnett's test). (Middle left) Quantification of FMOD in HFF-1 cells; n = 3, ***p < 0.001 (Dunnett's test). (Middle right) Quantification of THBS1 in BJ cells; n = 3, *p < 0.05, **p < 0.01 (Dunnett's test). (Right) Quantification of FMOD in BJ cells; n = 3, ***p < 0.001 (Dunnett's test).

E) WB analysis of THBS1 and p21 in human dermal and epidermal tissues (n = 6). Data were normalized to the maximum (1) value. $R^2$ was calculated using the "stat_poly_eq" function of R. (Upper panel) Age of each donor is displayed at the bottom of the image (see donor list in Table 2.2.1). (Lower left panel) Quantification of THBS1 expression in dermis. (Lower right panel) Quantification of p21 expression in dermis.

F) *THBS1* expression between healthy participants and patients with Hutchinson–Gilford progeria syndrome (HGPS). Public RNA-seq data27 for healthy participants (age: 1–9 years, n = 12) and patients with HGPS (age: 2–8 years, n = 10) derived from dermal fibroblasts. Gene expression was normalized to $\log_2(TPM + 1)$. **p < 0.01 (Ilch's t-test).

### 3.1.5 TGF-β1 and THBS1 induce senescence of human dermal fibroblasts

Next, I investigated the biological functions of TGF-β1 and THBS1 in terms of the senescence of human dermal fibroblasts [76]. I first assessed the proliferation of HFF-1 cells (Figure 3.1.5A) and found that TGF-β1 treatment suppressed HFF-1 growth over time (8 h, 12 h, 24 h, and 48 h) compared to that of untreated cells. As with TGF-β1, THBS1 treatment resulted in a concentration-dependent decrease in cell viability (Figure 3.1.5B). TGF-β1 and THBS1 treatments were confirmed to inhibit DNA synthesis by BrdU incorporation experiments (Figure 3.1.5C). The levels of the senescence markers Lamin-B1 decreased and p21 increased in a TGF-β1 dose-dependent manner (Figure 3.1.5D). Like the TGF-β1 treatment, THBS1 enhanced p21 expression (Figure 3.1.5E), confirming that TGF-β1- or THBS1-dependent suppression of cell proliferation is caused by cellular senescence. TGF-β1 or THBS1 treatment of HFF-1 cells induced the production of the pro-inflammatory SASPs IL-6 and IL-8 (Figure 3.1.5F). TGF-β1 treatment also decreased Lamin-B1 expression (Figure 3.1.5G) and increased IL-6, IL-8 (Figure 3.1.5H) in BJ cells. Moreover, treatment with TGF-β1 or THBS1 significantly increased the number of SA-β-gal-positive cells (Figure 3.1.5I). Interestingly, FMOD alone did not affect SA-

β-gal activity; however, in combination treatments, FMOD suppressed the effects of TGF-β1 or THBS1 on SA-β-gal activation. In addition, TGF-β1 treatment also increased SA-β-gal activity in BJ cells (Figure 3.1.5J). These results strongly suggest that TGF-β1 and THBS1 promote the senescence of skin fibroblasts and this effect is suppressed by FMOD.

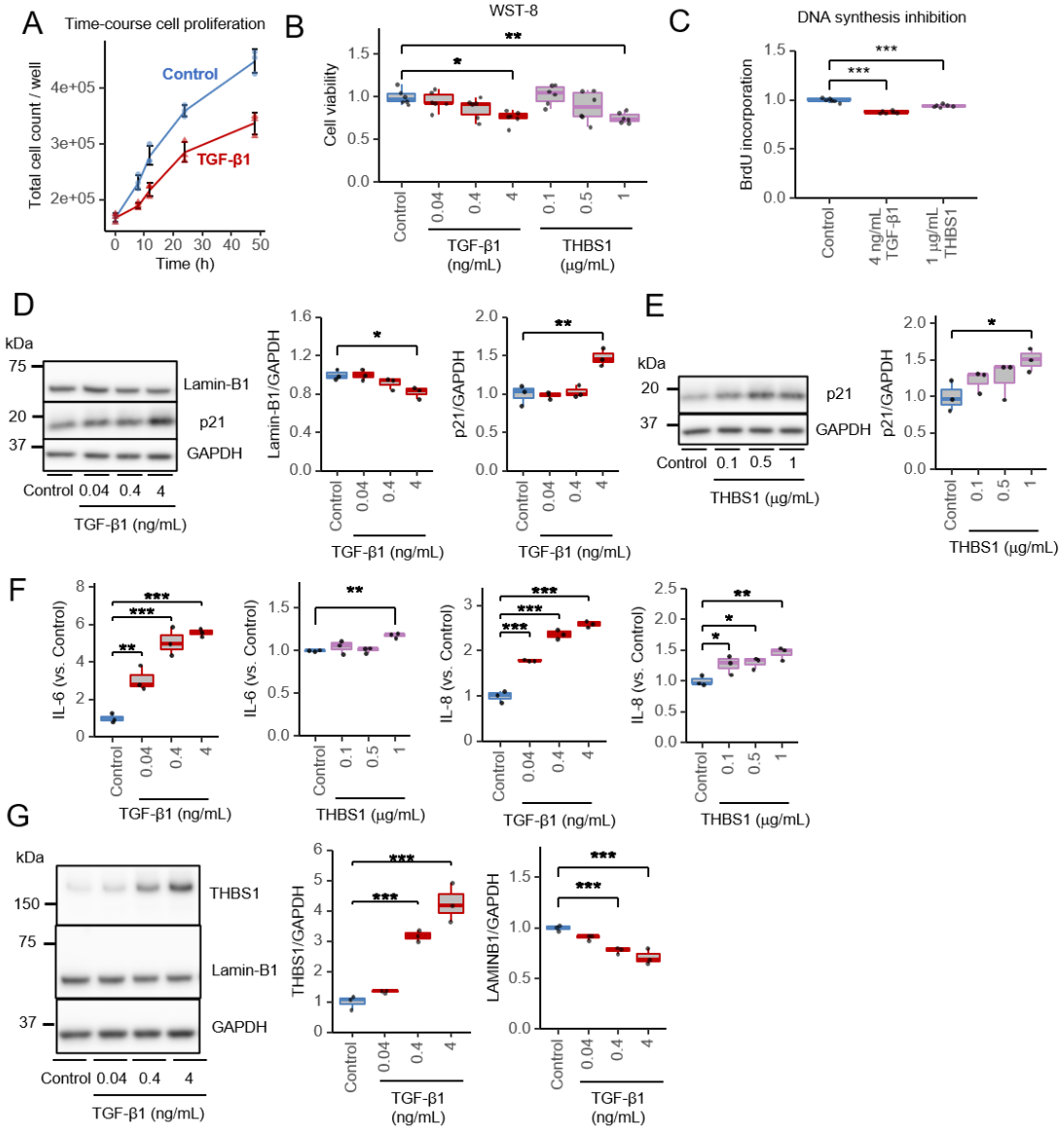

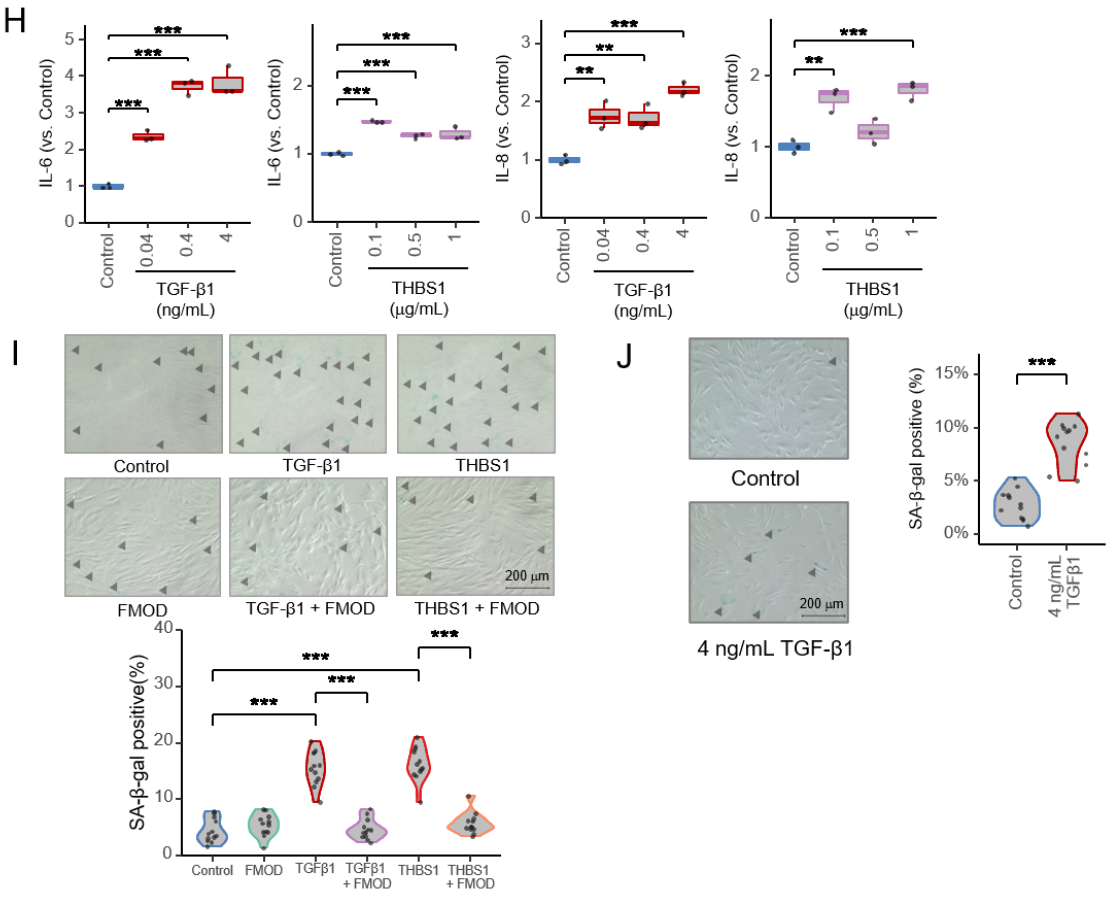


**Figure 3.1.5**: TGF-β1 and THBS1 induce senescence of human dermal fibroblasts [76].

A) Time-course cell proliferation analysis of control (blue-circled dots) or 4 ng/mL TGF-β1-treated (red triangular dots) cells stained with trypan blue; n = 3, mean ± SD.

B) Cell viability analysis of TGF-β1- and THBS1-stimulated HFF-1 cells. After 24 h of treatment (control: blue, TGF-β1: red, THBS1: purple), cell viability was measured using the tetrazolium salt WST-8; n = 6, *p < 0.05, **p < 0.01 (Tukey's multiple comparisons).

C) BrdU incorporation assay: control (blue), 4 ng/mL TGF-β1 (red), or 1 μg/mL THBS1 (purple); n = 6, ***p < 0.001 (Dunnett's test)

D) WB analysis of Lamin-B1 and p21 in TGF-β1-stimulated HFF-1 cells. Cell lysates were collected 48 h after control (blue) or TGF-β1 (red) treatment. (Left panel) Representative image. (Middle panel) Quantification of Lamin-B1; n = 3, *p < 0.05 (vs. control, Dunnett's test). (Right panel) Quantification of p21; n = 3, ***p < 0.001 (Dunnett's test).

E) Istern blot of p21 in THBS1-stimulated HFF-1 cells. Cell lysates were collected 48 h after control (blue) or THBS1 (purple) treatment. (Left panel) Representative image. (Right panel) Quantification of p21; n = 3, *p < 0.05 (Dunnett's test).

F) IL-6 and IL-8 ELISA in TGF-β1- or THBS1-stimulated HFF-1 cells. Cell supernatants

were collected 48 h after TGF-β1 (red) or THBS1 (purple) treatment. (First panel) Quantification of IL-6 ELISA with TGF-β1 treatment; n = 3, **p < 0.01, ***p < 0.001 (Dunnett's test). (Second panel) Quantification of IL-6 ELISA with THBS1 treatment; n = 3, **p < 0.01 (Dunnett's test). (Third panel) Quantification of IL-8 ELISA with TGF-β1 treatment; n = 3, **p < 0.01, ***p < 0.001 (Dunnett's test). (Fourth panel) Quantification of IL-8 ELISA with THBS1 treatment; n = 3, **p < 0.01 (Dunnett's test).

G) WB of THBS1 and Lamin-B1 in TGF-β1-stimulated BJ cells. Cell lysates were collected 48 h after control (blue) or TGF-β1 (red) treatment. (Left panel) Representative image. (Middle panel) Quantification of THBS1; N=3, ***p<0.001 (Dunnett's test). (Right panel) Quantification of Lamin-B1; N=3, ***p<0.001 (Dunnett's test).

H) IL-6 and IL-8 ELISA in TGF-β1- or THBS1-stimulated BJ cells. Cell supernatants were collected at 48 h after control (blue), TGF-β1 (red), or THBS1 (purple) treatment. (First panel) Quantification of IL-6 ELISA with TGF-β1 treatment; N=3, ***p<0.001 (Dunnett's test). (Second panel) Quantification of IL-6 ELISA with THBS1 treatment; N=3, ***p<0.01 (Dunnett's test). (Third panel) Quantification of IL-8 ELISA with TGF-β1 treatment; N=3, **p<0.01, ***p<0.001 (Dunnett's test). (Fourth panel) Quantification of IL-8 ELISA with THBS1 treatment; N=3, **p < 0.01, ***p < 0.001 (Dunnett's test).

I) Effect of TGF-β1 or THBS1 treatment and inhibition by FMOD on SA-β-gal activity. HFF-1 cells were treated with control, 4 ng/mL TGF-β1, 0.5 μg/mL THBS1, or 8 ng/mL FMOD. Combinations of 4 ng/mL TGF-β1 and 8 ng/mL FMOD as well as 0.5 μg/mL THBS1 and 8 ng/mL FMOD were performed alongside stand-alone treatments. (Left panel) Representative images. SA-β-gal-positive cells are shown with black arrowhead; scale bars: 200 μm. See Figure S4E for processed images. (Right panel) Quantification of SA-β-gal: SA-β-gal-positive rate (%) =number of SA-β-gal-positive cells / total number of cells × 100. Four images per well were randomly analyzed from three wells (total 12 images/condition), ***p < 0.001 (Tukey's multiple comparisons).

J) Effect of TGF-β1 simulation on SA-β-gal activity in BJ cells. (Left panel) Representative images. SA-β-gal-positive cells are shown with black arrowheads; scale bar: 200 μm. (Right panel) Quantification of SA-β-gal: SA-β-gal-positive rate (%) =number of SA-β-gal-positive cells / total number of cells × 100. Four images from each of the three wells were analyzed (total 12 images/condition), ***p<0.001 (vs. control, Student's t-test).

### 3.1.6 THBS1 and FMOD expression is controlled by the TGF-β signaling pathway

THBS1 is known to activate latent TGF-β1 [79], while FMOD reportedly binds to TGF-β1 to inhibit its binding to the TGF-βR [80–82]. THBS1 is also known to be induced by TGF-β1 stimulation in human dermal fibroblasts [101]. Consistently, I found that THBS1 expression was

induced by TGF-β1 in HFF-1 cells (Figure 3.1.6A) [76]. However, the same TGF-β1 treatment decreased FMOD expression. These results were also confirmed in BJ cells (Figure 3.1.5G, 3.1.6B). Next, the effect of FMOD on THBS1 expression was examined in HFF-1 cells (Figure 3.1.6C). While TGF-β1 alone increased THBS1 expression, the addition of FMOD completely suppressed THBS1 levels. In contrast, THBS1 treatment downregulated FMOD expression in a dose-dependent manner (Figure 3.1.6D). These findings suggest a mutual inhibitory role for THBS1 and FMOD. Interestingly, stimulation of BJ cells with THBS1 enhanced its own expression (Figure 3.1.6E), suggesting the positive-feedback regulation of the TGF-β pathway by THBS1 in dermal fibroblasts. I additionally investigated the effects of other TGF-β family members, particularly TGF-β2 and TGF-β3, on the expression of THBS1 and FMOD, and found that THBS1 expression was promoted (Figure 3.1.6F) and FMOD expression was suppressed (Figure 3.1.6G) in all members of the TGF-β family. Therefore, TGF-β2 and TGF-β3 may also be involved in skin aging, but they were found to regulate THBS1 and FMOD via a common mechanism as TGF-β1.

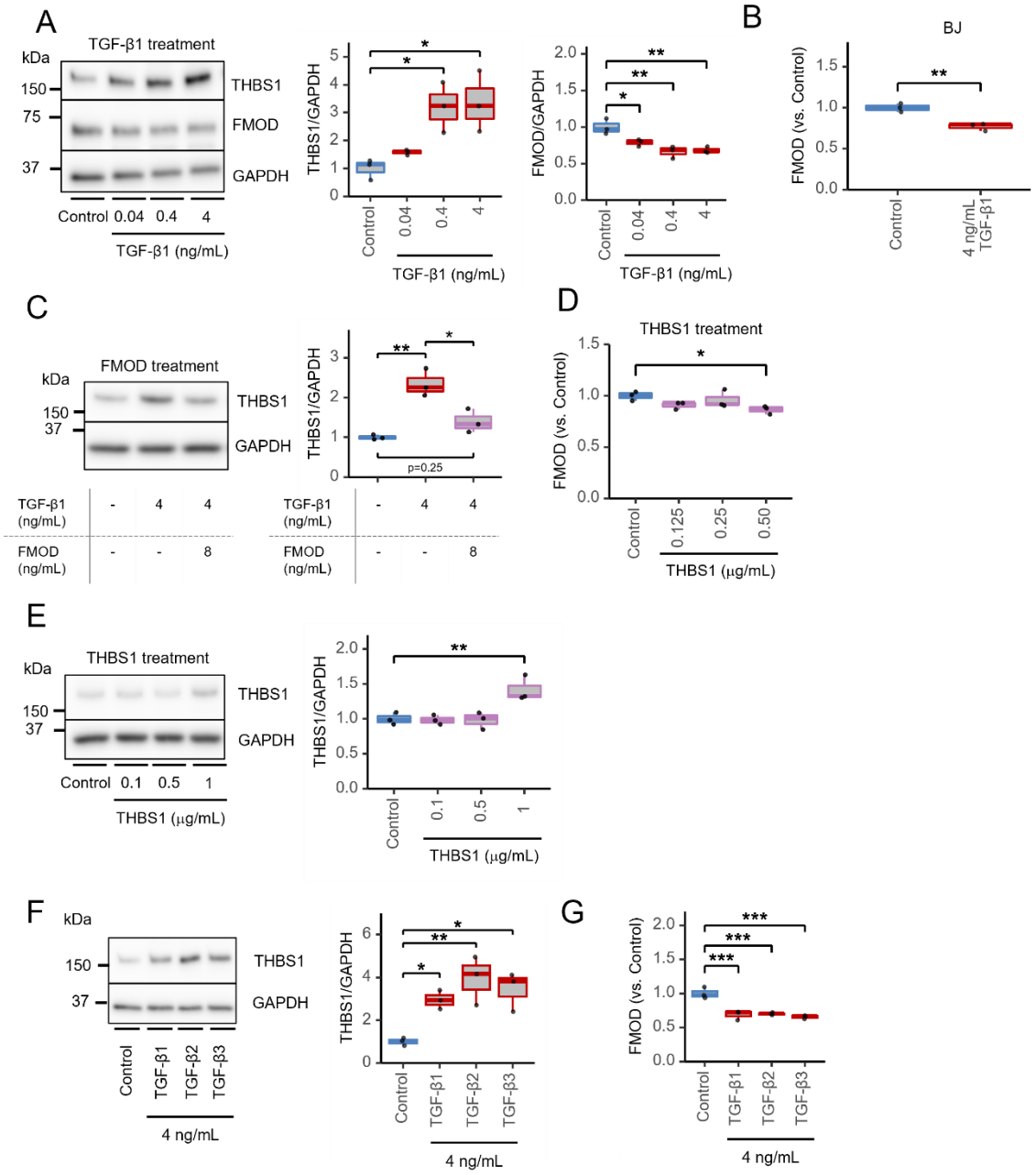


**Figure 3.1.6**: THBS1 and FMOD expression is controlled by the TGF-β signaling pathway [76].

A) WB of THBS1 and FMOD in TGF-β1-stimulated HFF-1 cells. Cell lysates were collected 48 h after control (blue) or TGF-β1 (red) treatment. (Left panel) Representative image. (Middle panel) Quantification of THBS1; n = 3, *p < 0.05 (vs. control, Dunnett's test). (Right panel) Quantification of FMOD; n = 3, *p < 0.05, **p < 0.01 (Dunnett's test).

B) FMOD ELISA in TGF-β1-stimulated BJ cells. Cells were treated with control (blue) or 4 ng/mL TGF-β1 (red) for 48 h and their supernatants were analyzed; N=3, **p<0.01 (Student's t-test).

C) WB analysis of THBS1 in TGF-β1- and FMOD-stimulated HFF-1 cells. Cell lysates were collected 48 h after treatment with control (blue), 4 ng/mL TGF-β1 (red), or a combination of 4 ng/mL TGF-β1 and 8 ng/mL FMOD (purple). (Left panel) Representative image. (Right panel) Quantification of THBS1; n = 3, *p < 0.05, **p < 0.01 (Tukey's multiple comparisons).

D) FMOD ELISA of THBS1-stimulated HFF-1 cells. Cells were treated with THBS1 (purple) for 48 h and their supernatants were analyzed; n = 3, *p < 0.01 (Dunnett's test).

E) WB analysis of THBS1 in THBS1-stimulated BJ cells. Cell lysates were collected 48 h after control (blue) or THBS1 (purple) treatment. (Left panel) Representative image. (Right panel) Quantification of THBS1; n = 3, **p < 0.01 (Dunnett's test).

F) WB analysis of TGF-β family-stimulated HFF-1 cells. Cell lysates were collected 48 h after control (blue) or 4ng/mL TGF-β family (red; with TGF-β1, TGF-β2, TGF-β3) treatment and the lysates were analyzed. (Left panel) Representative image. (Right panel) Quantification of THBS1 expression; N=3, *p<0.05, **p<0.01 (Dunnett's test).

G) FMOD ELISA in TGF-β family-stimulated HFF-1 cells. Cells were treated with control (blue) or 4 ng/mL TGF-β family (red; with TGF-β1, TGF-β2, TGF-β3) for 48 h and their supernatants were analyzed; N=3, ***p<0.001 (Dunnett's test).

### 3.1.7 THBS1 regulation requires SMAD activation and c-Fos/c-Jun DNA binding

I investigated the regulation of THBS1 and FMOD by TGF-β1 and related signaling pathways using small molecule inhibitors and small interfering (si) RNA KD experiments [76]. TGF-β1-dependent induction of THBS1 and phosphorylation of SMAD2 and SMAD3 were inhibited by LY364947 (TGF-βRI/TGF-βRII inhibitor) and SB431542 (TGF-βRI inhibitor; Figure 3.1.7A). Because both SMAD3 and SMAD4 cooperate with c-Fos/c-Jun of the activator protein-1 (AP1) family to mediate TGF-β-induced transcription [102–104], I tested the involvement of c-Fos/c-Jun in the regulation of THBS1 using siRNA. C-Fos/c-Jun KD significantly reduced the TGF-β1-induced expression of THBS1 compared to that with non-targeted KD (Figure 3.1.7B). The siRNA of c-Fos/c-Jun showed downregulation of c-Fos/c-Jun expression without affecting the activation of SMAD2, SMAD3, and SMAD4 (Figure 3.1.7C). The AP-1 DNA binding inhibitor, T-5224, was also tested for its effect on THBS1 regulation in HFF-1 cells (Figure 3.1.7D). While T-5224 alone had no effect on THBS1 expression compared to TGF-β1 alone, the combination of TGF-β1 and T-5224 reduced THBS1 expression. I also confirmed that T-5224 of c-Fos/c-Jun did not affect the activation of SMAD2, SMAD3, and SMAD4 (Figure 3.1.7E). These findings suggest that regulation of THBS1 in dermal fibroblasts requires the formation of AND-gated networks through the activation of SMAD and binding of c-Fos/c-Jun to DNA, both of which are activated by TGF-β stimulation.

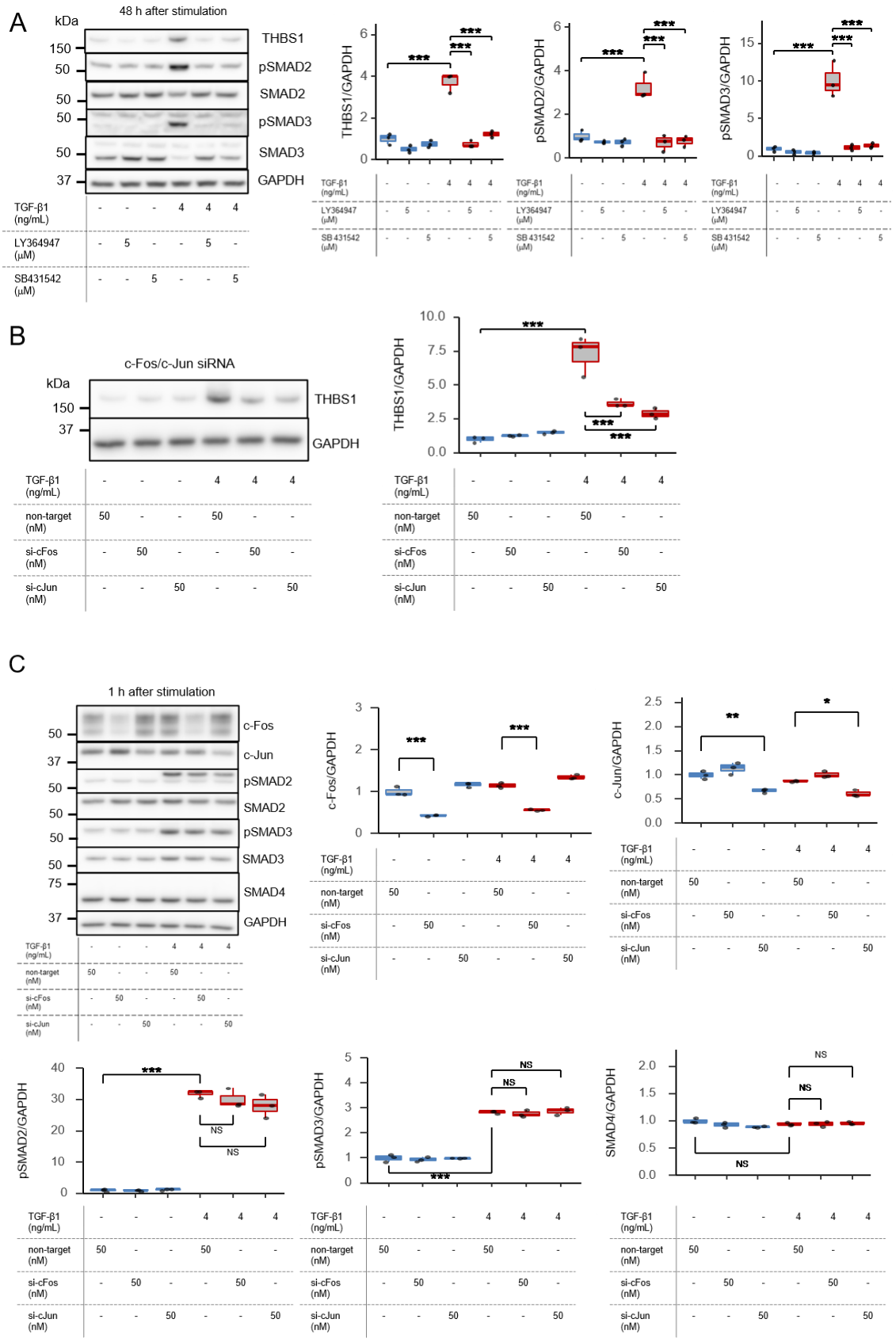
A
48 h after stimulation
kDa
150
50
50
50
50
37
THBS1
pSMAD2
SMAD2
pSMAD3
SMAD3
GAPDH
THBS1/GAPDH
pSMAD2/GAPDH
pSMAD3/GAPDH
TGF-β1 (ng/mL)
LY364947 (μM)
SB431542 (μM)
B
c-Fos/c-Jun siRNA
kDa
150
37
THBS1
GAPDH
THBS1/GAPDH
non-target (nM)
si-cFos (nM)
si-cJun (nM)
C
1 h after stimulation
50
37
50
50
50
50
75
37
c-Fos
c-Jun
pSMAD2
SMAD2
pSMAD3
SMAD3
SMAD4
GAPDH
c-Fos/GAPDH
c-Jun/GAPDH
pSMAD2/GAPDH
pSMAD3/GAPDH
SMAD4/GAPDH
NS
TGF-β1 (ng/mL)
non-target (nM)
si-cFos (nM)
si-cJun (nM)

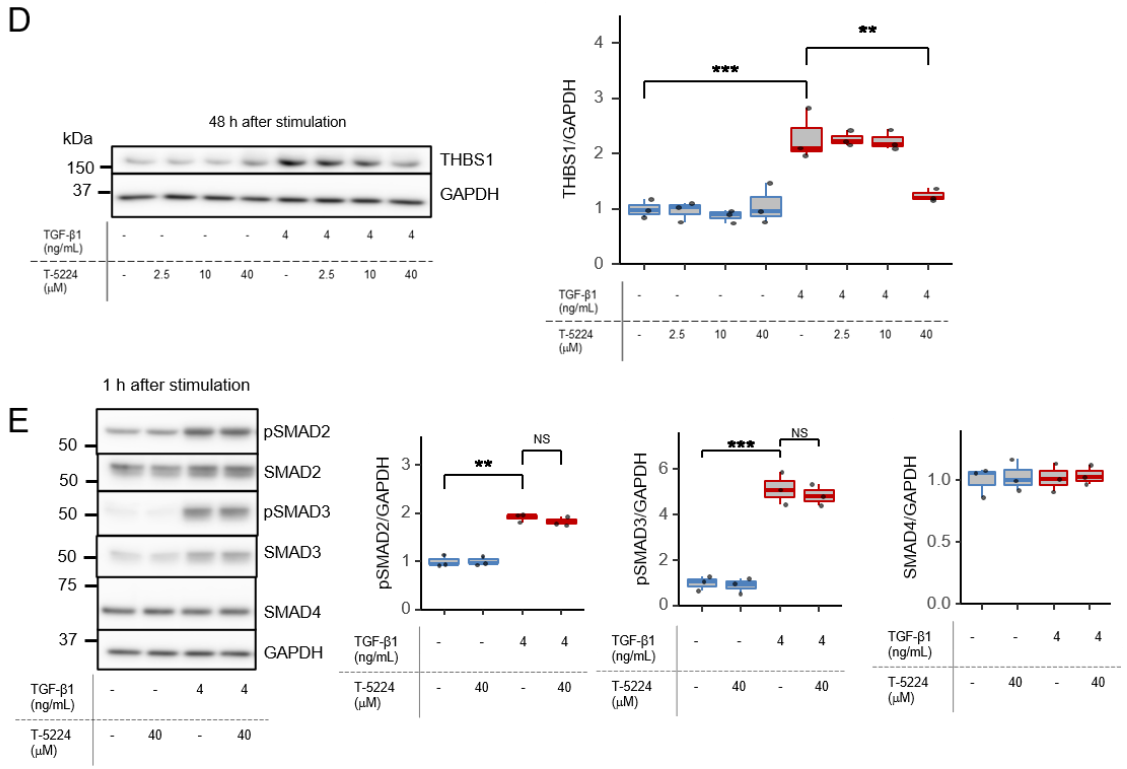


**Figure 3.1.7**: THBS1 regulation requires SMAD activation and c-Fos/c-Jun DNA binding [76].

A) WB analysis of TGF-β1-stimulated HFF-1 cells treated with TGF-βR inhibitors. Cells were treated with LY364947 and SB431542 with/without TGF-β1 for 48 h and the lysates were analyzed. (Left panel) Representative image. (Right panel) Quantification of THBS1, pSMAD2, and pSMAD3 expression following TGF-βR inhibitor treatment; N=3, ***p<0.001 (Tukey's multiple comparisons).

B) WB analysis of THBS1 with c-Fos/c-Jun knockdown (KD) using HFF-1 cells. Cells were pretreated with each siRNA (50 nM) and collected 48 h after control (blue) or 4 ng/mL TGF-β1 (red) treatment. (Left panel) Representative image. (Right panel) Quantification of THBS1; n = 3, **p < 0.01 (Tukey's multiple comparisons).

C) WB analysis of c-Fos/c-Jun KD in HFF-1 cells. C-Fos/c-Jun KD cell lysates were collected at 1 h after control (blue) or TGF-β1 (red) treatment. (Left panel) Representative image. (Right panel) Quantification of c-Fos, c-Jun, pSMAD2, pSMAD3, and SMAD4; N=3, *p<0.05, **p<0.01, ***p<0.001, NS: not significant (Tukey's multiple comparisons).

D) WB analysis of TGF-β1-stimulated HFF-1 cells treated with T-5224. Cells were treated with/without T-5224, and TGF-β1 for 48 h and the lysates were analyzed. (Left panel) Representative image. (Right panel) Quantification of THBS1; N=3, **p<0.01, ***p<0.001 (Tukey's multiple comparisons).

E) WB analysis of TGF-β1-stimulated HFF-1 cells treated with T-5224. Cells were treated with/without T-5224, and TGF-β1 for 1 h and lysates were analyzed. (Left panel) Representative image. (Right panel) Quantification of pSMAD2, pSMAD3, and SMAD4; N=3, **p<0.01, ***p<0.001, NS: not significant (Tukey's multiple comparisons).

### 3.1.8 Impact of Kinase Inhibitors on FMOD Expression in Dermal Fibroblasts

To investigate the regulatory mechanism of FMOD in dermal fibroblasts, I conducted a compound screening using various kinase inhibitors (Figure 3.1.8A) [76]. The candidates in the screening included Ki8751 (VEGFRII inhibitor), GW5074 (c-Raf1 inhibitor), and U0126 (MEK1/2 inhibitor). Alongside these compounds, ZM306416 (VEGFRI inhibitor) was also selected to validate the effect on FMOD expression, which was found to be significantly suppressed (Figure 3.1.8B). Further supporting this, the expression of FMOD was found to be significantly increased with higher concentrations of VEGF (Figure 3.1.8C). Additionally, other growth factors, such as epidermal growth factor (EGF), basic-fibroblast growth factor (b-FGF), and platelet derived growth factor-BB (PDGF-BB), which also activate c-Raf and MEK, were found to reduce FMOD expression (Figure 3.1.8D). These results collectively suggest that FMOD is regulated by the VEGF signaling pathway in dermal fibroblasts.

To determine the mechanism of FMOD suppression by TGF-β1, I tested whether the combination of kinase inhibitor and TGF-β1 would restore FMOD expression (Figure 3.1.8E) [76]. Akt inhibitor VIII (Akt inhibitor) or LY294002 (PI3K inhibitor) significantly restored FMOD expression in the presence of TGF-β1. These results indicate that THBS1 and FMOD expression is regulated by the TGF-β and VEGF-Raf-ERK signaling pathway, respectively (Figure 3.1.8.F), and that the TGF-β1-dependent suppression of FMOD is mediated by the PI3K-Akt pathway.

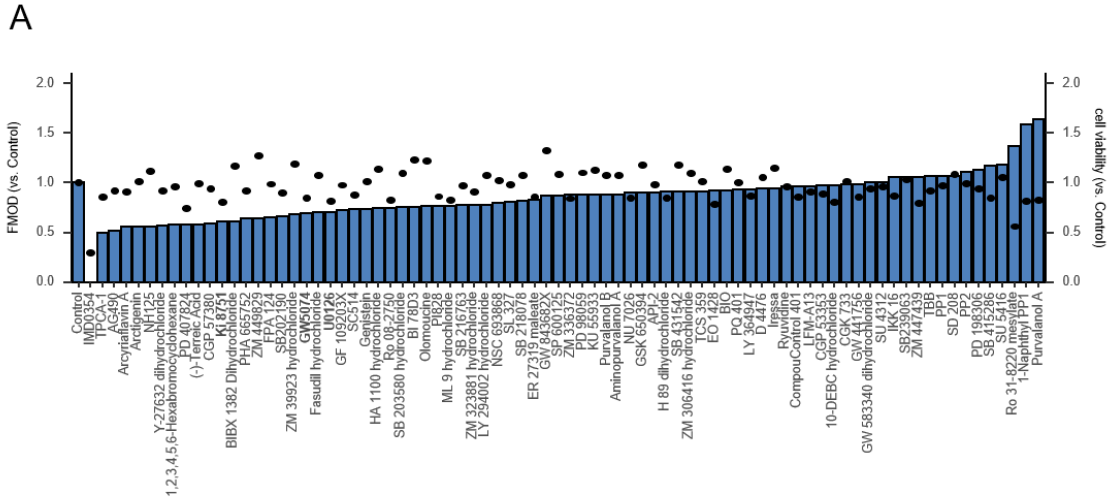

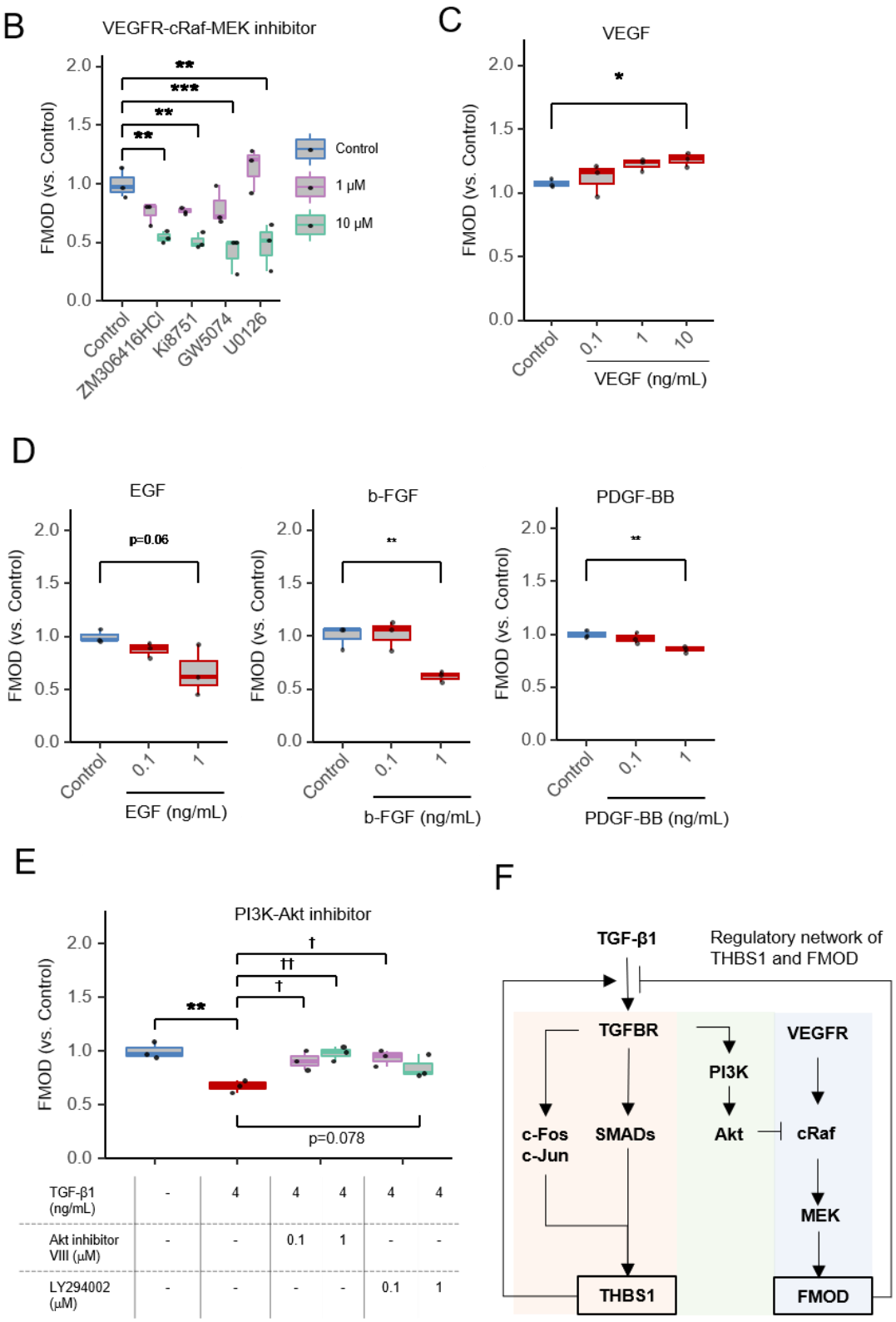


**Figure 3.1.8**: Impact of kinase inhibitors on FMOD expression in dermal fibroblasts [76].

A) FMOD ELISA in kinase inhibitors-screening of HFF-1 cells. Cells were treated with

various kinase inhibitors for 48 h and their supernatants were analyzed. (Left axis) Quantification of FMOD (vs. control). (Right axis) Cell viability (vs. control) measured using the tetrazolium salt WST-8; n = 1.

B) FMOD ELISA of kinase inhibitor-treated HFF-1 cells. Cells were treated with ZM306416HCl, Ki8751, GW5074, or U0126 for 48 h and their supernatants were analyzed; n = 3, **p < 0.01, ***p < 0.001 (Dunnett's test).

C) FMOD ELISA of VEGF165 treated HFF-1 cells. Cells were treated with VEGF165 for 48 h and the supernatants were analyzed; n = 3, *p < 0.05 (Dunnett's test).

D) FMOD epidermal growth factor (EGF), basic-fibroblast growth factor (b-FGF), or platelet derived growth factor-BB (PDGF-BB) treatment of HFF-1 cells. Cells were treated with each ligand for 48 h and their supernatants were analyzed; N=3, **p<0.01 (Dunnett's test).

E) FMOD ELISA in kinase inhibitor- and TGF-β1-treated HFF-1 cells. Cells were treated with Akt inhibitor VIII or LY294002 combined with 4 ng/mL TGF-β1 for 48 h and their supernatants were analyzed; n = 3, **p < 0.01 (Student's *t*-test), $^{\dagger}$p < 0.05, $^{\dagger\dagger}$p < 0.01 (Dunnett's test).

F) Regulatory network of THBS1 and FMOD. In human dermal fibroblasts, TGF-β1 induced THBS1 production occurs via TGF-βR–SMAD activation (red shade). FMOD was regulated via activation of the VEGFR–cRaf–MEK pathway (blue shade). Crosstalk between these pathways occurred with the TGF-β pathway inhibiting the VEGF pathway via the PI3K-Akt pathway (green shade).

### 3.1.9 Bifurcation Analysis of Dermal Senescence

A nonlinear ordinary differential equation (ODE) model of the core network consisting of TGF-β1, THBS1, and FMOD was constructed to qualitatively elucidate the behavior of the system (Figure 3.1.9A, see details in the Methods section) [76]. Fitting against the datasets of THBS1 and FMOD levels at different TGF-β1 concentrations yielded parameters that reproduced the experimental results (Figure 3.1.9B), while the parameters for regulation of TGF-β1 by THBS1 ($K_1$) and FMOD ($K_2$) are yet to be identified. I examined which parameter is more influential for controlling the steady state, and found that both parameters can induce a bistable switch for TGF-β1 (Figure 3.1.9C). Since the expression levels of THBS1 and FMOD were upregulated and downregulated with the increase of TGF-β1expressions, respectively, changing these parameters simulates the transition from low- to high-TGF-β1 states (Figure 3.1.6A). For the purpose of this study, we defined 'high-TGF-β1' as the state with high-THBS1 and low-FMOD expressions, and 'low-TGF-β1' as the state with low-THBS1 and high-FMOD expressions, respectively. Importantly, the bistable region was quite asymmetric with respect to $K_1$ and $K_2$: changes in $K_1$

always induced a transition from the current state, whereas changes in $K_2$ induced the transition only for a small parameter range of $K_1$ (Figure 3.1.9C). Moreover, we extended the core model to a stochastic model to simulate the probability distributions of THBS1 (see details in the Methods section) (Figure 3.1.9D). As a result, we found that the bimodal distribution of THBS1 expression becomes relatively unimodal when the value of $K_1$ is changed from 14 (near the bifurcation point) to 10, which corresponds to increasing TGF-β1 levels. In contrast, changing the value of $K_2$ ($K_1 = 16$) does not produce bifurcation. Taken together, we concluded that $K_1$ has more influence on state transitioning.

To better understand the roles of endogenous TGF-β1, THBS1, and FMOD, we extended the above-mentioned model as an endogenous core model to incorporate the effects of PDL and endogenous TGF-β1 production for simulating the system behavior in an endogenous condition (Figure 3.1.9E) [76]. By fitting the steady state values of THBS1, FMOD, and TGF-β1 against the corresponding *in vitro* experimental values for different PDLs (Figures 3.1.4A, 3.1.4B), we estimated the endogenous TGF-β1 normalized production rate as $\gamma \approx 3.5$ (Figure 3.1.9F). I found that the endogenous core model also shows binary high-/low-TGF-β1 states. Moreover, it was observed that THBS1 is sensitive against $\gamma < 1$ (bifurcation point: $\gamma \approx 0.07$), where endogenous TGF-β1 production rate is low. Consequently, the nonlinear model was shown to provide a core network for assessing the molecular contributions to both skin aging and dermal fibroblast senescence.

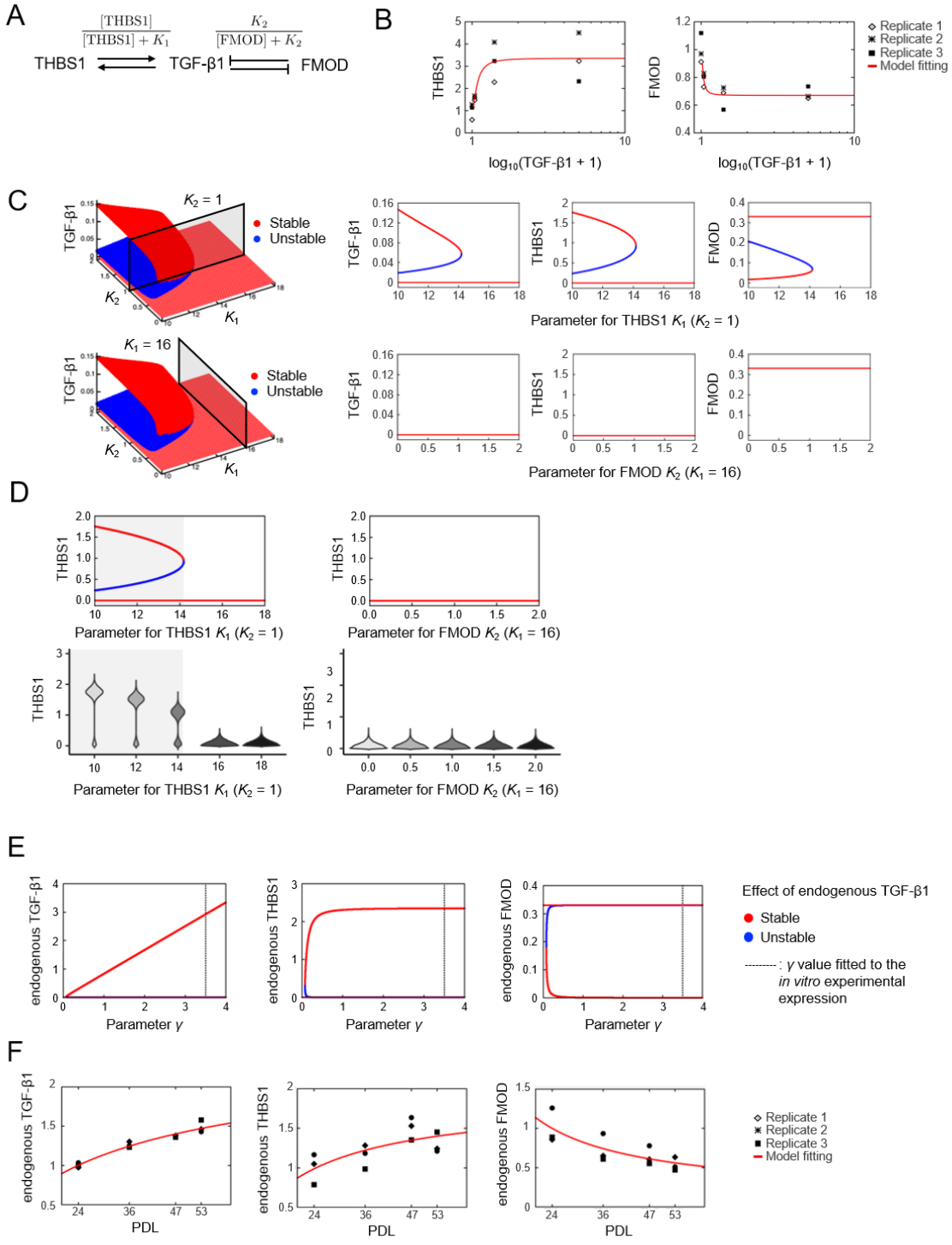


**Figure 3.1.9**: Bifurcation analysis of dermal senescence [76].

A) Core network consisting of TGF-β1, THBS1, and FMOD. Arrows and barred lines represent positive and negative regulations, respectively.

B) Model parameters for the core network consisting of TGF-β1, THBS1, and FMOD were trained on the experimental expressions of THBS1 and FMOD upon treatment with

different concentrations (0.04, 0.4, or 4 ng/mL) of TGF-β1 (Figure 3.1.6A). The x- and y-axes represent steady state expressions of TGF-β1 and THBS1 (left panel) or FMOD (right panel). The points (◇: Replicate 1, ※: Replicate 2, ■: Replicate 3) indicate experimental data, and red solid lines indicate model fitting results.

C) Bifurcation diagrams of steady state expressions of TGF-β1, THBS1, and FMOD, with respect to $K_1$ (upper panel) and $K_2$ (bottom panel), which correspond to the cut surfaces shown in left panels, respectively. Note that $[\mathrm{TGF\beta1}] \equiv 0$ is a stable solution for $K_1 > 0$ and $K_2 > 0$. Red and blue colors represent stable and unstable points on the surface, respectively. Solutions with high TGF-β1 expression levels indicate a high-THBS1 (low-FMOD) state, while those with low TGF-β1 expression levels indicate a low-THBS1 (high-FMOD) state.

D) Bifurcation diagrams (upper panel) and probability distributions (bottom panel) for the expression level of THBS1 with respect to $K_1$ (left panel) and $K_2$ (right panel), which correspond to the cut surfaces shown in Figure 3.1.9C. Stable (red) and unstable (blue) fixed points are computed using a deterministic model, while distributions are computed using a stochastic model with 10,000 independent simulations. Gray shade indicates the change in $K_1$ from 14 (near the bifurcation point) to 10, which corresponds to an increase in TGF-β1.

E) Bifurcation diagrams of the steady state expressions of endogenous TGF-β1, THBS1, and FMOD with respect to γ, computed from the extended model. Red and blue points represent stable and unstable points, respectively, and vertical broken line at γ≈3.5 represent the fitted value to the *in vitro* experimental expression upon RS with different PDL.

F) Model parameters for the core network consisting of endogenous effects of TGF-β1, THBS1, and FMOD were trained on the experimental expression of THBS1, FMOD, and TGF-β1 upon RS with different PDL (PDL 24, PDL 36, PDL 47, PDL 53) (Figures 3.1.4A, 3.1.4B). The x- and y-axes represent steady state expressions of PDL and THBS1 (upper panel), FMOD (right panel), or TGF-β1 (bottom panel). The points (◇: Replicate 1, ※: Replicate 2, ■: Replicate 3) indicate experimental data, and red solid lines indicate model fitting results.

### 3.1.10 Irreversibility of THBS1 in Dermal Senescence

Here, we demonstrated a binary high-/low-TGF-β1 switch through bifurcation analysis. To validate the conclusions drawn from the mathematical approaches, I conducted additional experiments [76]. Firstly, I performed time-course washout experiments of TGF-β1 treatment to confirm the irreversibility of the regulatory system, which was suggested by the existence of

stable and unstable states. TGF-β1 was washed out at various time-points (i.e., 1 h, 2 h, 4 h, 8 h, 12 h, 24 h, and 48 h) and replaced with only the medium, which served as the control (Figure 3.1.10A, 3.1.10B). Interestingly, I found that both transient and sustained TGF-β1 treatments regulated THBS1 and FMOD expression in a similar manner. Furthermore, both treatments induced sustained activation of phosphorylated Akt (Ser473), implying that sustained stimulation is not essential for regulation of the system by TGF-β1, and that transient stimulation can reproduce the regulation. The regulation of THBS1 and Akt phosphorylation by transient and sustained stimulation was further confirmed with even shorter time-point washes (i.e., 15 min, 30 min, 1 h, 4 h, 12 h, 24 h, and 48 h) (Figure 3.1.10C). These results indicated an irreversible nature of THBS1 upregulation and FMOD downregulation by TGF-β1 treatment, suggesting the presence of a binary switch.

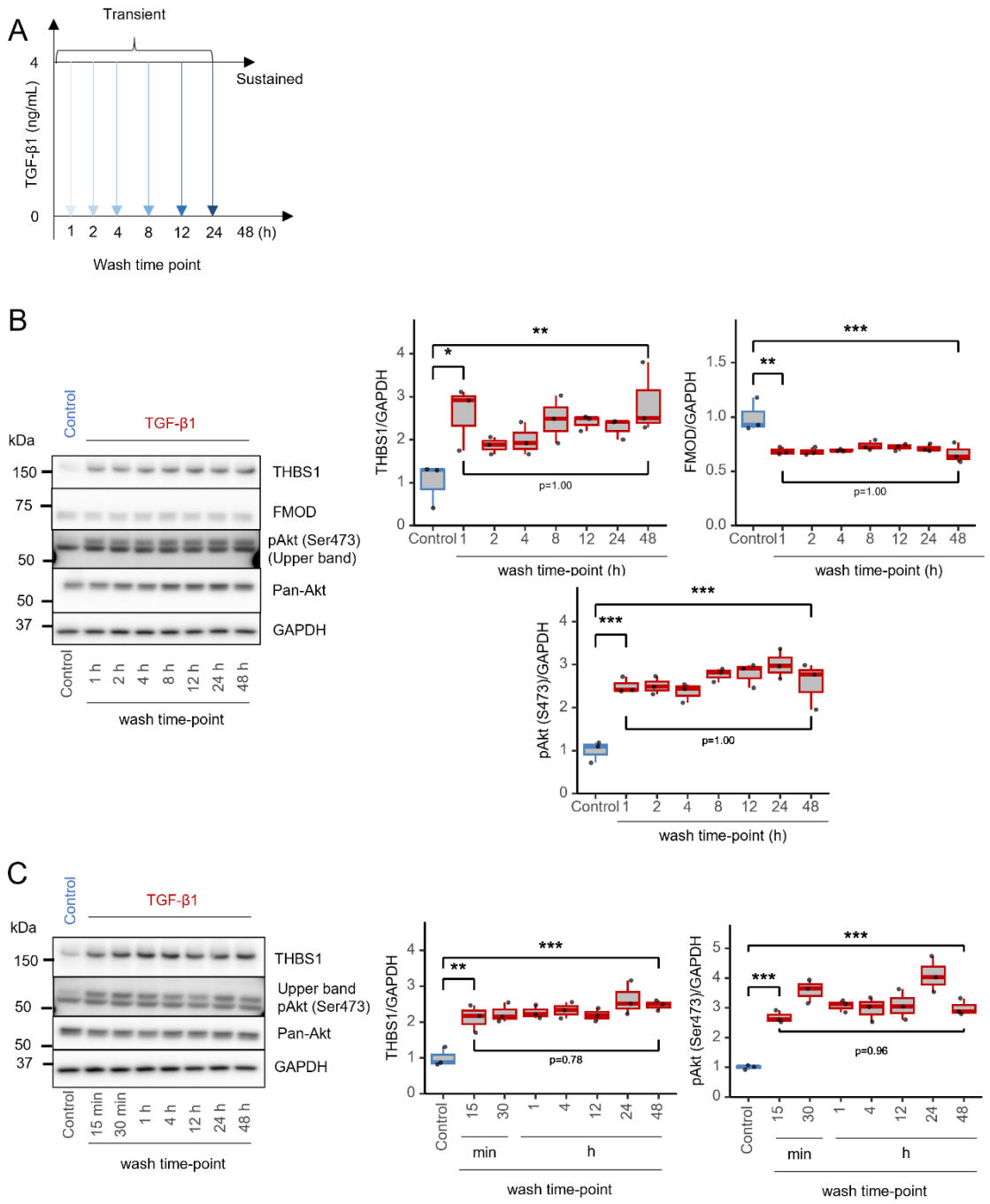


**Figure 3.1.10**: Irreversibility of THBS1 in dermal senescence [76].

A) Schematic representation of TGF-β1 washout experiment. The x- and y-axes represent the washout time-points and concentration dynamics of TGF-β1, respectively.

B) WB analysis of time-course TGF-β1 washout experiment using HFF-1 cells. Cells were treated with 4 ng/mL TGF-β1, washed with PBS at each time-point (1 h, 2 h, 4 h, 8 h, 12 h, 24 h, and 48 h), and lysates were collected at 48 h. (Left panel) Representative image. (Right panel) Quantification of THBS1, FMOD, and phosphorylated Akt (Ser473); N=3,

*p<0.05, **p<0.01, ***p<0.001 (Tukey's multiple comparisons).

C) WB analysis of TGF-β1 washout experiment using HFF-1 cells. Cells were treated with TGF-β1, washed with PBS at each time-point (15 min, 30 min, 1 h, 4 h, 12 h, 24 h, and 48 h), and lysates were collected at 48 h. (Left panel) Representative image. (Upper right panel) Quantification of THBS1; N=3, **p<0.01, ***p<0.001 (Tukey's multiple comparisons). (Bottom right panel) Quantification of phosphorylated Akt (Ser473); N=3, ***p<0.001 (Tukey's multiple comparisons).

### 3.1.11 Role of Endogenous TGF-β in Regulating THBS1 and FMOD Expression

Secondly, the effects of endogenous TGF-β signaling on THBS1, FMOD, and phosphorylated Akt (Ser473) expressions were confirmed through LY364947 treatment—a TGF-βRI/TGF-βRII inhibitor—performed during progressive passage-induced senescence at each PDL (Figure 3.1.11A) [76]. Inhibition of endogenous TGF-β signaling downregulated THBS1, but did not affect FMOD expression or the activation of phosphorylated Akt (Ser473). To further validate my *in vitro* findings with model simulations, I simulated the effect of TGF-βR inhibitor using the endogenous core model, by incorporating changes in the signaling pathways as the model parameter. Our stochastic simulations also showed that lowering the parameter γ for endogenous TGF-β1 production results in a decrease in THBS1 expression, while FMOD expression remains largely unchanged (see details in the STAR Methods section) (Figure 3.1.11B). These results indicate that when endogenous TGF-β signaling is inhibited, THBS1 is more likely to undergo a change of state, whereas FMOD remains barely sensitive.

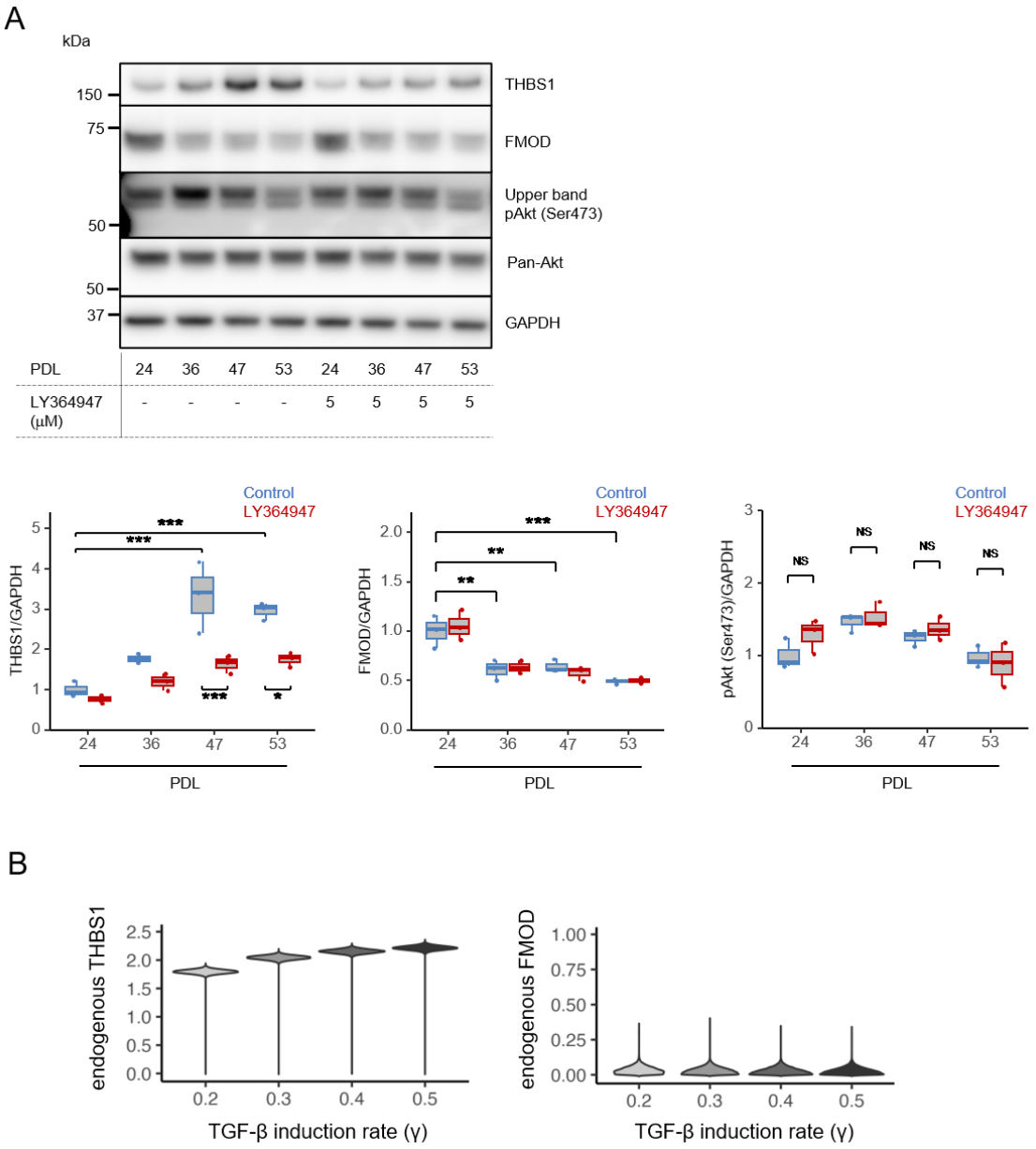


**Figure 3.1.11**: Role of endogenous TGF-β in regulating THBS1 and FMOD expression [76].

A) WB analysis of RS-induced HFF-1 cells treated with the TGF-βR inhibitor. Cells of each PDL (PDL 24, PDL 36, PDL 47, PDL 53) were treated with 5 μM LY364947 for 48 h and the lysates were analyzed. (Upper panel) Representative image. (Bottom left panel) Quantification of THBS1; N=3, *p<0.05, ***p<0.001 (Tukey's multiple comparisons). (Bottom middle panel) Quantification of FMOD; N=3, **p<0.01, ***p<0.001 (Tukey's multiple comparisons). (Bottom right panel) Quantification of phosphorylated Akt (Ser473); N=3, NS: not significant (Tukey's multiple comparisons).

B) Probability distributions for the expression levels of endogenous THBS1 (left panel) and FMOD (right panel) with respect to endogenous TGF-β1 production rate γ, as computed

using a stochastic model with endogenous parameters and 10,000 independent simulations.

### 3.1.12 Bimodality of THBS1 in Dermal Senescence

Thirdly, to further validate the presence of a binary high-/low-TGF-β1 switch, I examined the bistability of THBS1 expression using immunofluorescence imaging (Figure 3.1.12) [76]. Quantification of integral intensity of each image revealed that THBS1 expression was significantly upregulated by TGF-β1 in a concentration-dependent manner (Figure 3.1.12), which was consistent with the results obtained through western blot (Figure 3.1.6A). Additionally, a comparison of the mean intensities of each individual immunostained image showed that THBS1 expression was significantly upregulated by TGF-β1 (control vs. 0.2 ng/mL TGF-β1: $p < 0.05$), while bimodal distribution of THBS1 expression was also observed in the control group (Silverman test [105]; unimodal: $p = 0.19$, bimodal: $p = 0.028$). This result also demonstrated that the population of low-THBS1 cells (low TGF-β1) was reduced, whereas the population of high-THBS1 cells (high TGF-β1) increased by 0.2 ng/mL TGF-β1 (Silverman test; unimodal: $p = 0.11$, bimodal: $p = 0.92$). Overall, a distinct population of low-THBS1 cells remained present, although reduced by the effect of TGF-β1. A bimodal to unimodal shift in THBS1 expression by TGF-β1 was suggested based on the simulations of bifurcation analysis (Figure 3.1.9D). These findings support the existence of a binary high-/low-TGF-β1 switch in the network consisting of TGF-β1, THBS1, and FMOD.

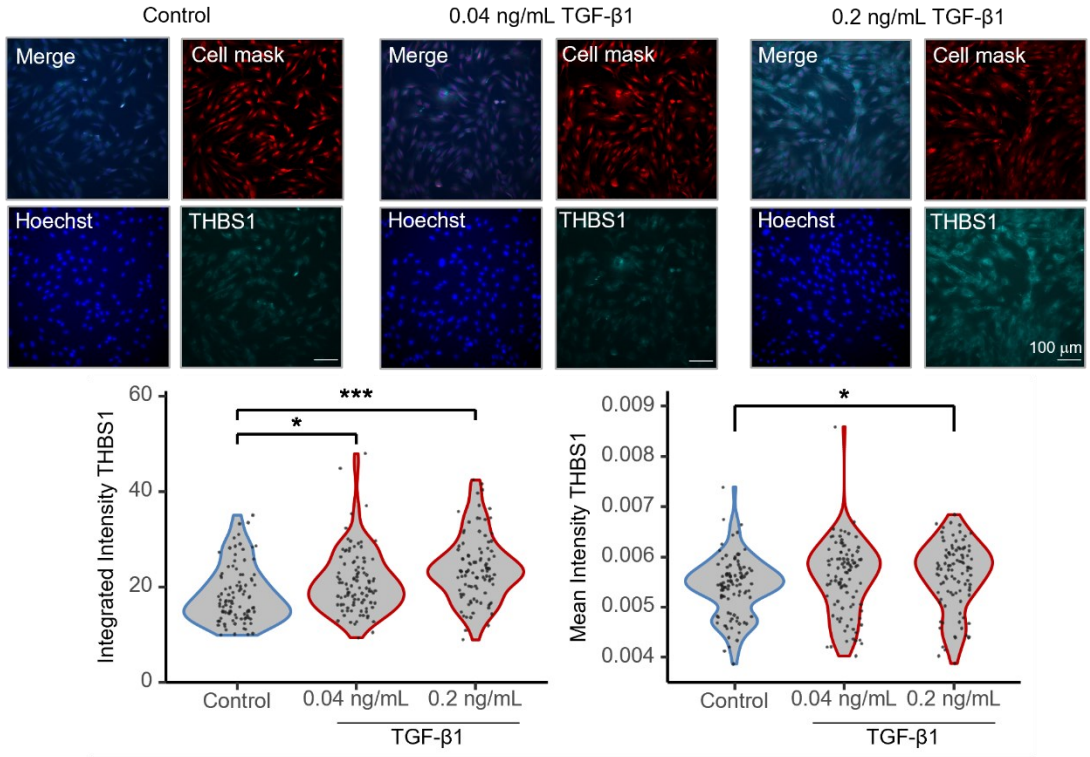


**Figure 3.1.12**: Bimodality of THBS1 in dermal senescence [76].

Distribution of THBS1 expression by immunofluorescence imaging using HFF-1 cells. Cells were treated with TGF-β1 for 48 h and fixed for immunofluorescence imaging. (Upper panel) Representative images; scale bars: 100 μm. (Bottom left panel) Quantification of integrated intensity of THBS1 of each image; 16 images per well from six wells were analyzed (total 96 images/condition); *p < 0.05, ***p < 0.001 (Dunnett's test). (Bottom right panel) Quantification of mean intensity of THBS1 of each image; 16 images per well from six wells were analyzed (total 96 images/condition); *p < 0.05 (Dunnett's test).

### 3.1.13 Mechanistic Mathematical Model of Skin Aging

Because of the limitations in explaining the molecular mechanisms using the above-mentioned model near equilibrium state, I further constructed a comprehensive ODE model of the TGF-β and VEGF receptor signaling network to quantitatively understand the dynamics of skin aging regulated by THBS1 and FMOD (Figure 2.3.3) [76]. The integrated model included latent TGF-β1 activation by THBS1 [79], inhibition by FMOD [80–82], SMAD-AP1 complex formation [102–104], a negative feedback by SMAD7 [106], positive feedback of THBS1 [79,107–109], VEGFR and Raf-ERK cascade [68,88], and PI3K-Akt crosstalk between the TGF-β and VEGF pathways. The model was constructed using parameters trained with time-course data (i.e., 0 min,

15 min, 30 min, 60 min, 120 min, 8 h, 24 h, and 48 h) of protein phosphorylation or expression (i.e., phosphorylated SMAD3, c-Fos, THBS1, phosphorylated Akt, and FMOD) in HFF-1 cells stimulated with or without TGF-β1 (Figure 3.1.13A). I obtained 30 well-fitting parameter sets (Figure 2.3.4) that reproduced the experimental data (see details in the Methods section). The traces of 30 optimization runs and distribution of the objective function, i.e., sum of residual squares between simulation and experimental values, showed a uniform distribution, indicating robust parameter estimation results (Figure 2.3.5). The resulting model had 79 rate equations, 83 species, and 194 parameters. To validate the model and assess the reproducibility of the model dynamics, I used phosphor-SMAD2 data, which was not used as training data (Figure 3.1.13B). Finally, I obtained a model that could successfully reproduce most of the experimental results for HFF-1 cells.

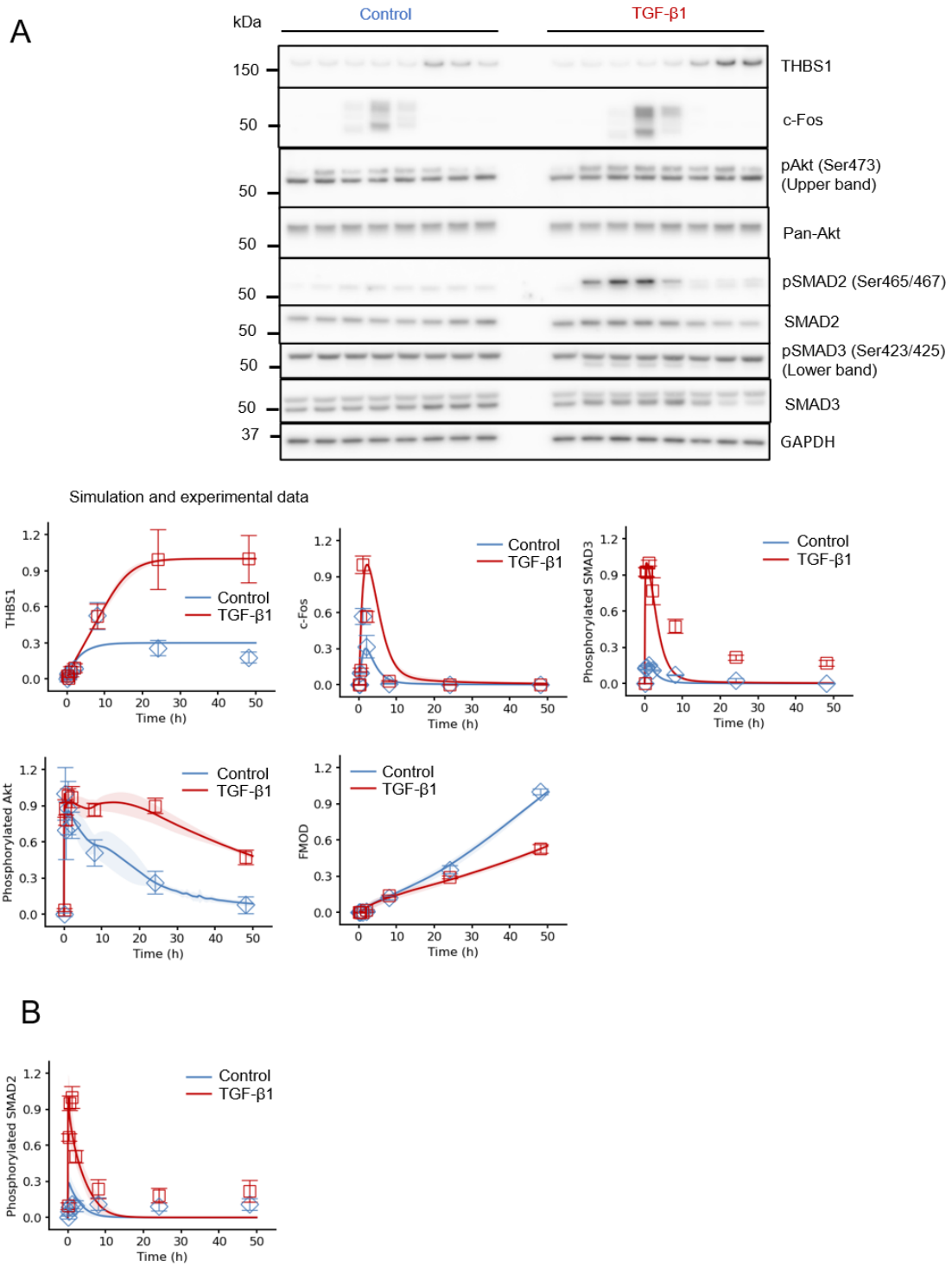


**Figure 3.1.13**: Mechanistic mathematical model of skin aging [76].

A) Experimental time-course WB image with/without TGF-β1 treatment in HFF-1 cells. HFF-1 was stimulated with/without TGF-β1 and the lysates were collected at 0 min, 15 min, 30 min, 60 min, 120 min, 8 h, 24 h, and 48 h. Model parameters for the integrated TGF-β–VEGF model were trained on time-course phosphorylated SMAD3, c-Fos,

THBS1, phosphorylated Akt (Ser473), and FMOD protein levels. (Upper panel) Representative image (Bottom panel) The points (control: blue squares, TGF-β1: red squares) indicate experimental data, solid lines indicate the average simulation of 30 parameter sets, and shade areas indicate SD. Error bar represents SD; n = 3, mean ± SD.

B) Validation of mechanistic model using phosphorylated SMAD2. The model reproduced phosphorylated SMAD2 dynamics. The points (control: blue squares; 4 ng/mL TGF-β1: red squares) indicate experimental data, solid lines indicate the average simulation of 30 parameter sets, and shaded areas indicate SD; N=3, mean ± SD.

### 3.1.14 Late inhibition of PI3K-Akt is crucial for FMOD downregulation by TGF-β1

As TGF-β1 and VEGF expression is known to increase during cellular senescence [110,111] and in HFF-1 cells with higher PDL (Figure 3.1.4A, 3.1.14A), numerical simulations were conducted with the generated comprehensive ODE model to mimic these changes [76]. In these simulations, the initial concentrations of TGF-β1 and VEGF were increased to represent a state of senescence (Fig 3.1.14B). The input increased, the levels of phosphorylated SMAD3 and activated Ras (Ras-GTP) gradually increased. Interestingly, as senescence progressed, THBS1 gradually increased until 24 h, while FMOD started to decrease from the 24 h time-point, as compared to the control. I also observed that while the basal condition induced transient activation (blue line) of phosphorylated Akt at early phase, higher initial values resulted in sustained Akt activation (red line). This is likely because as cellular senescence progresses, Akt activation switches from transient to sustained, and sustained Akt activation suppresses FMOD expression in the later stages of the dynamics. Based on the simulation of FMOD expression, the 24 h time-point (black arrow) was identified as the breakpoint of FMOD inhibition by transient and sustained Akt activation. This suggests that the Akt activation observed in early phase does not affect FMOD expression, and that FMOD recovery may be achieved by selectively inhibiting persistent Akt activity in the late phase.

To verify this difference in Akt activation, I examined FMOD recovery in TGF-β1-treated HFF-1 cells by adding LY294002 (or Akt inhibitor VIII) at specific time-points to suppress Akt phosphorylation (3.1.14C) [76]. While FMOD expression was significantly reduced by TGF-β1 treatment alone, co-treatment with LY294002 (or Akt inhibitor VIII) from start to end (indicated as 0 h) restored FMOD expression. When the inhibitor was added at 8 h or 24 h, FMOD recovered to the same level as observed at 0 h. However, no recovery was observed after 32 h, which exceeds the 24 h breakpoint where FMOD begins to decrease. Thus, using model simulations and their validation, I have demonstrated that the sustained dynamics of Akt activity are critical for the negative regulation of FMOD expression in the progression of cellular senescence.

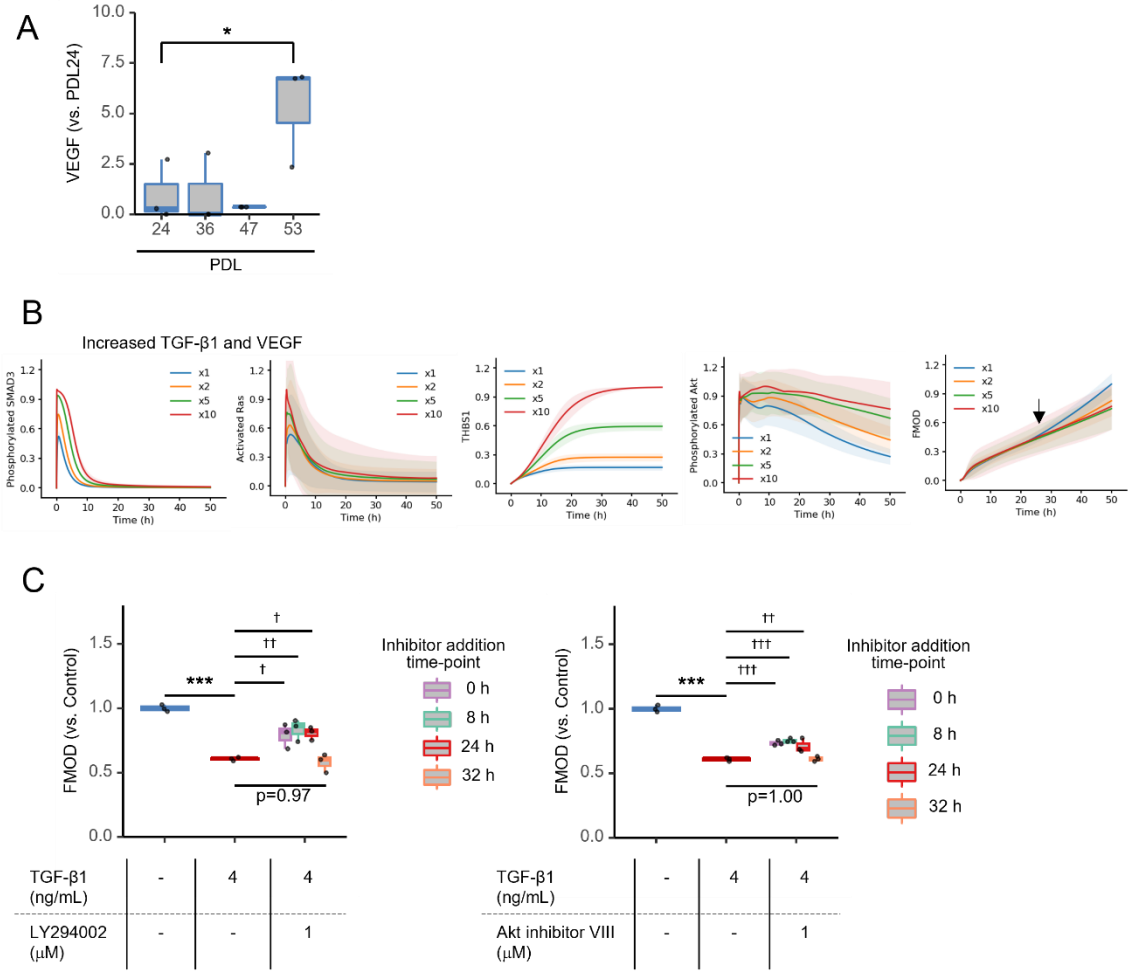


**Figure 3.1.14**: Late inhibition of PI3K-Akt is crucial for FMOD downregulation by TGF-β1 [76].

A) VEGF ELISA in RS-induced HFF-1 cells. Cells of each PDL (PDL 24, PDL 36, PDL 47, PDL 53) were cultured for 48 h, and supernatants were analyzed by VEGF ELISA; N=3, *p<0.05 (Dunnett's test).

B) Simulation of phosphorylated SMAD3, activated Ras (Ras-GTP), THBS1, FMOD, and phosphorylated Akt levels using integrated TGF-β–VEGF mathematical model. Initial values of both TGF-β1 and VEGF were increased, as indicated by the color code (from ×1 to ×10). Solid lines indicate the average simulation of 30 parameter sets, and shade areas indicate SD. The black arrow indicates breakpoint of FMOD inhibition.

C) Quantification of FMOD in LY294002- (left panel) or Akt inhibitor viii- (right panel) treated HFF-1 cells by ELISA. Cells were initially treated with 4 ng/mL TGF-β1, 1 μM LY294002 or 1 μM Akt inhibitor viii was added at certain time-points (0 h, purple; 8 h, green; 24 h, bright red; 32 h, orange), and supernatants were collected at 48 h. The relative expression to the control (blue) is shown. TGF-β1 conditions that were not treated with inhibitors are indicated in dark red. n = 3, ***p < 0.01 (vs. control, Student's *t*-test), † p

< 0.05, †† p < 0.01, ††† p < 0.01 (vs. TGF-β1, Dunnett's test).

### 3.1.15 THBS1 is a sensitive factor, FMOD is a robust factor, and SMAD2/3/4 formation is effective in suppressing THBS1 expression

Finally, I aimed to identify the target molecule regulating the rate of cellular senescence. My findings thus far point to two possible targets: THBS1 can be downregulated or FMOD can be upregulated. To determined which target is more suitable for manipulation, I simulated THBS1 and FMOD expression as model outputs by increasing the input of TGF-β1 and VEGF, respectively (Figure 3.1.15A) [76]. Interestingly, the simulation showed that THBS1 expression was sensitive to TGF-β1 input, whereas FMOD was minimally affected by VEGF input. This prediction for VEGF was confirmed in an *in vitro* experiment with HFF-1 cells (Figure 3.1.8C). Indeed, the expression of FMOD was significantly increased with increasing VEGF concentrations, but the rate of increase was much lower than that for THBS1 induced by TGF-β1 (Figure 3.1.6A). These results suggest that THBS1 is a sensitive factor, while FMOD is a more robust factor in cell senescence.

To further identify the molecular factors regulating THBS1 activity, I performed a sensitivity analysis [112] to determine the bottleneck of the TGF-β signaling network with THBS1 as output (Figure 3.1.15B) [76]. A reaction involving SMAD2–SMAD3–SMAD4 complex formation (V13, black arrow) was shown to be more sensitive than reactions involving SMAD2 and SMAD3 alone. This finding suggests that inhibition of the SMAD4 reaction can effectively suppress THBS1 production. This simulation was validated by monitoring TGF-β1-induced THBS1 expression after siRNA KD of SMAD2, SMAD3, and SMAD4 in HFF-1 cells (Figure 3.1.15C). As suggested by the model, SMAD4 KD had the greatest effect on THBS1 expression compared to that of SMAD2 and SMAD3. Combinations of SMAD2–SMAD4, SMAD3–SMAD4, or SMAD2–SMAD3–SMAD4 KDs did not show synergistic or additive effects compared to SMAD4 KD alone. After KD of each SMAD, I found that SMAD4 KD significantly suppressed the induction of TGF-β1-induced SA-β-gal positivity compared to that by SMAD2 and SMAD3 KDs (Figure 3.1.15D). I also checked the effect of each SMAD KD on Lamin-B1—which was reduced by TGF-β1 treatment—to determine if SMAD4 KD is effective against other aging markers (Figure 3.1.15E). I found that SMAD4 ($p < 0.01$) KD significantly restored Lamin-B1 expression, whereas SMAD2 ($p=0.79$) and SMAD3 ($p=0.72$) did not. These results suggested that SMAD4 is essential for THBS1 induction and is a critical target for controlling cellular senescence.

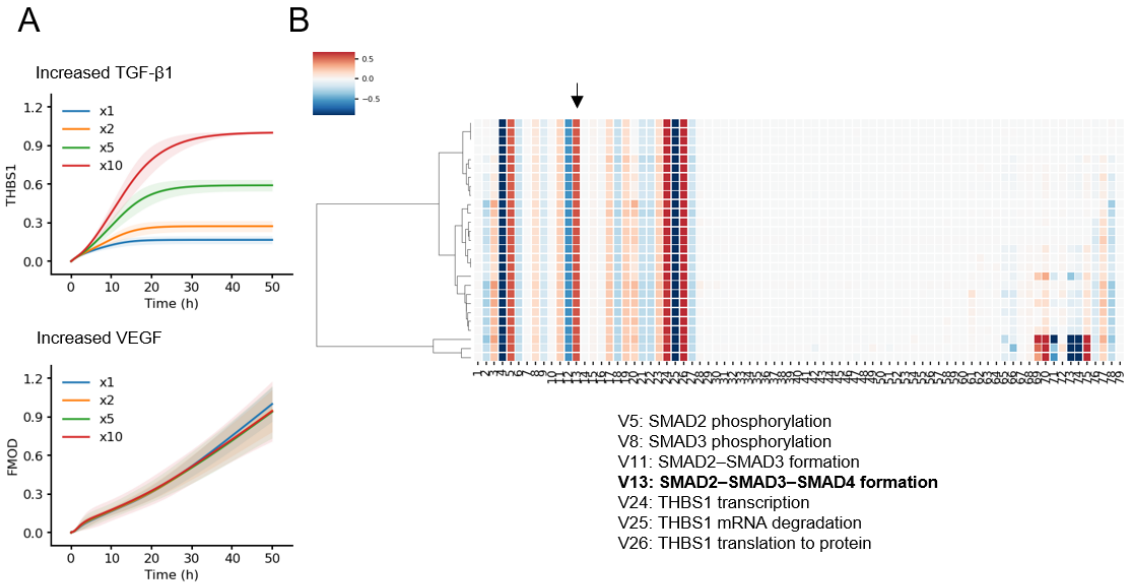
A
Increased TGF-β1
THBS1
x1
x2
x5
x10
Time (h)
Increased VEGF
FMOD
B
V5: SMAD2 phosphorylation
V8: SMAD3 phosphorylation
V11: SMAD2–SMAD3 formation
V13: SMAD2–SMAD3–SMAD4 formation
V24: THBS1 transcription
V25: THBS1 mRNA degradation
V26: THBS1 translation to protein

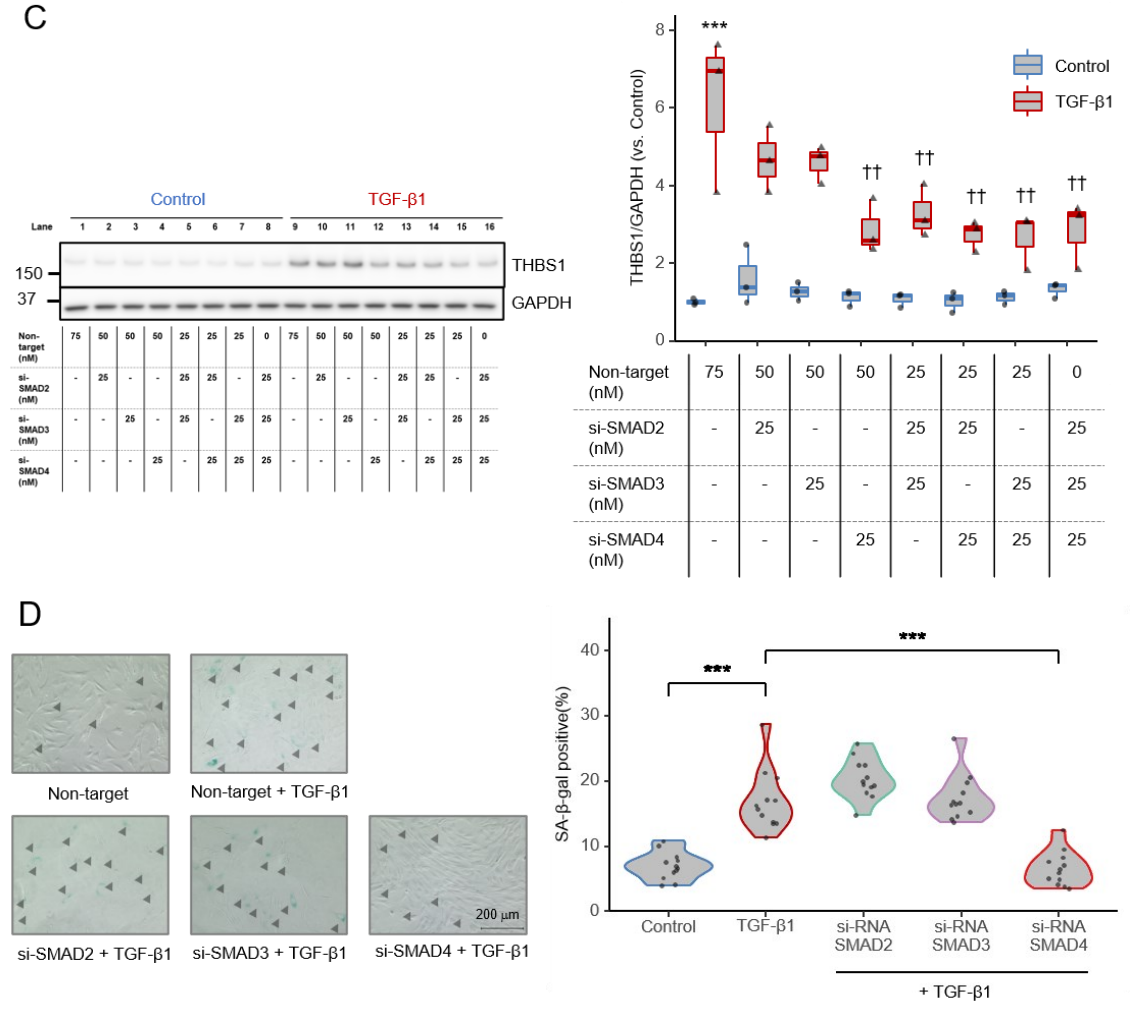
C
Control
TGF-β1
Lane
150
37
THBS1
GAPDH
THBS1/GAPDH (vs. Control)
Non-target (nM)
si-SMAD2 (nM)
si-SMAD3 (nM)
si-SMAD4 (nM)
D
Non-target
Non-target + TGF-β1
si-SMAD2 + TGF-β1
si-SMAD3 + TGF-β1
si-SMAD4 + TGF-β1
200 μm
SA-β-gal positive(%)
Control
TGF-β1
si-RNA SMAD2
si-RNA SMAD3
si-RNA SMAD4
+ TGF-β1

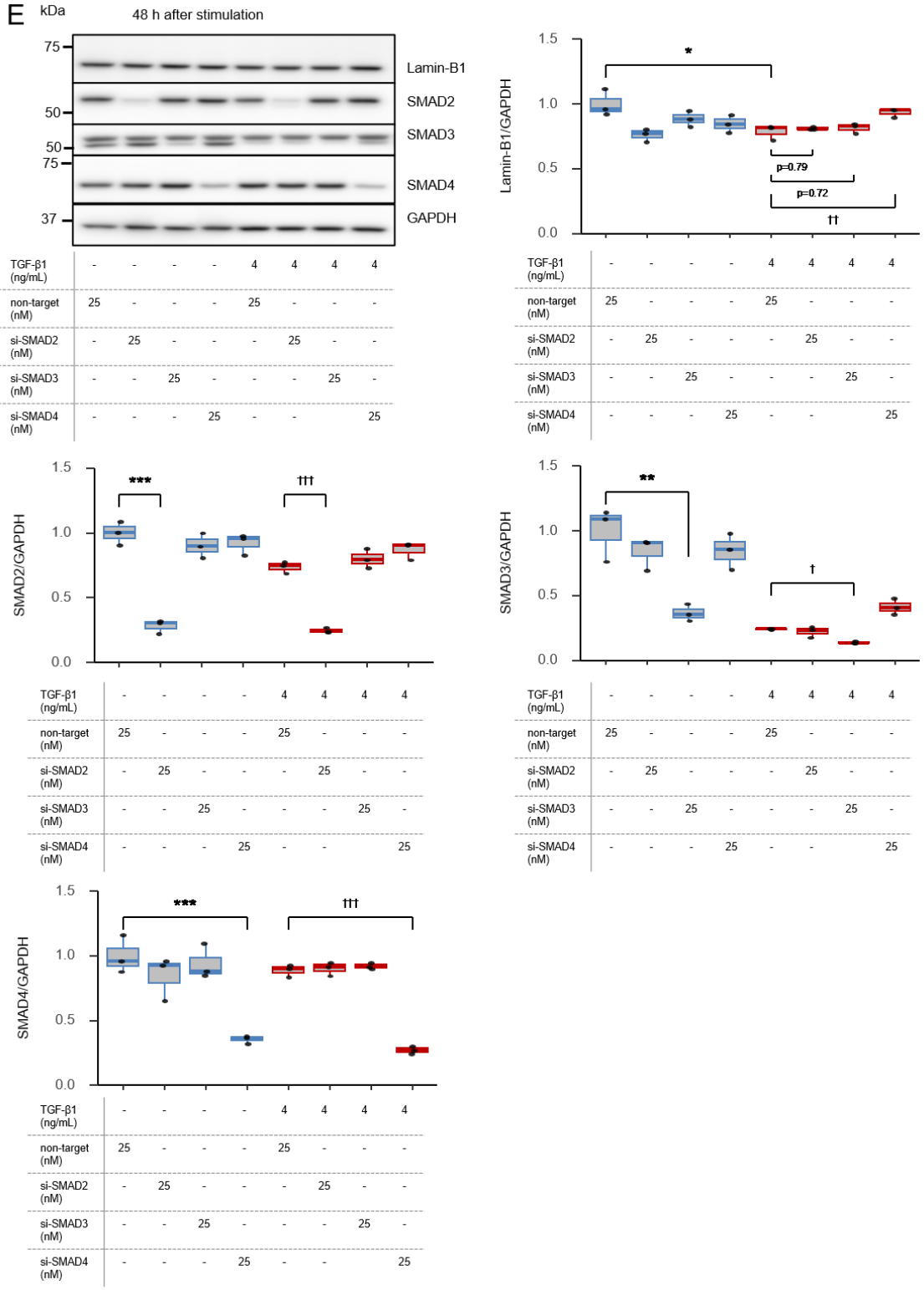


**Figure 3.1.14**: Late inhibition of PI3K-Akt is crucial for FMOD downregulation by TGF-β1 [76].

A) Simulation of THBS1 and FMOD using developed mathematical model. The initial value of TGF-β1 for THBS1 or VEGF for FMOD were increased, as indicated by the color code

(From ×1 to ×10). Solid lines indicate the average simulation of 30 parameter sets, and shade areas indicate SD.

B) Sensitivity analysis of TGF-β1-induced THBS1 for 30 parameter sets. Negative coefficients (blue) indicate that the quantity of the response metric decreases as species increase, while positive coefficients (red) indicate that the quantity of the metric increases. The black arrow indicates V13, SMAD2–SMAD3–SMAD4 formation.

C) Validation of the sensitivity analysis by WB analysis of THBS1 following siRNA KD of SMADs in HFF-1 cells. Lysates were collected 48 h after pretreatment with each SMAD siRNA alone or in combination for 24 h prior to stimulation with or without 4 ng/mL TGF-β1. (Left panel) Representative image. (Right panel) Quantification of THBS1 with SMADs KD; n = 3, ***$p < 0.001$ (vs. non-target control treatment, Student's *t*-test), $^{\dagger\dagger}p < 0.01$ (vs. non-target TGF-β1 treatment, Dunnett's test).

D) Effect of siRNA KD of SMADs on SA-β-gal activity. HFF-1 cells were pretreated with each 25 nM siRNA and stimulated with or without 4 ng/mL TGF-β1. (Left panel) Representative images. SA-β-gal-positive cells are indicated with the arrowhead (black). Scale bars, 200 μm. See Figure S13A for processed images. (Right panel) Quantification of SA-β-gal: SA-β-gal-positive rate (%) =SA-β-gal-positive cells / total number of cells × 100. Four images per well were randomly analyzed from three wells (total 12 images/condition), ***$p < 0.001$ (Tukey's multiple comparisons).

E) WB analysis of Lamin-B1 and SMADs following siRNA KD of SMADs in HFF-1 cells. Cells were pretreated with each siRNA (25 nM) and collected 48 h after control (blue) or 4 ng/mL TGF-β1 (red) treatment. (Left panel) Representative image. (Upper right panel) Quantification of Lamin-B1; N=3, *$p<0.05$ (Student's *t*-test), $^{\dagger\dagger}p<0.01$ (Dunnett's test). (Middle left panel) Quantification of SMAD2; N=3, ***$p<0.001$ (Dunnett's test), $^{\dagger\dagger\dagger}p<0.001$ (Dunnett's test). (Middle right panel) Quantification of SMAD3; N=3, **$p<0.01$ (Dunnett's test), $^{\dagger}p<0.05$ (Dunnett's test). (Bottom left panel) Quantification of SMAD4; N=3, ***$p<0.001$ (Dunnett's test), $^{\dagger\dagger\dagger}p<0.001$ (Dunnett's test).

## 3.2 Identification of Potent THBS1 Suppressor and its Mechanism Toward Senescence

### 3.2.1 ATRA Suppresses THBS1 by Nuclear Transcriptional Regulation

As THBS1 was identified as a key promoter of skin aging, I decided to search for an effective molecule to suppress THBS1.To manipulate cellular senescence via THBS1, I screened a natural product library and identified compounds that efficiently suppressed TGF-β1-induced THBS1 expression (Figure 3.2.1A). Among the 268 screened compounds, isotretinoin (13-*cis*-retinoic acid) was the most potent suppressor of THBS1. Consequently, I assessed other retinoic acid-related compounds such as retinol and ATRA (Figure 3.2.1B). TGF-β1-induced THBS1 was suppressed after treatment with LY364947, a TGF-βRI/TGF-βRII inhibitor ($p < 0.001$, TGF-β1 vs. 5 μM LY364947 + TGF-β1). Retinol showed no effect on THBS1 suppression at a concentration of 0.5 μM ($p > 0.05$, TGF-β1 vs. 0.5 μM Retinol + TGF-β1); however, it suppressed THBS1 at a concentration of 5 μM ($p < 0.001$, TGF-β1 vs. 5 μM Retinol + TGF-β1). Additionally, ATRA more potently inhibited THBS1 than retinol at the same concentration ($p < 0.01$, 5 μM Retinol + TGF-β1 vs. 5 μM ATRA + TGF-β1). As retinol is metabolized in the body and converted to ATRA [113], I further investigated using ATRA.

Herein, immunostaining for SMAD4, which translocates to the nucleus upon TGF-β1 stimulation, was performed to elucidate the regulatory mechanism by which ATRA suppresses THBS1 (Figure 3.2.1C). Treatment with TGF-β1 localized SMAD4 in the nucleus ($p < 0.001$, control vs. TGF-β1), whereas treatment with LY364947 and TGF-β1 combination prevented SMAD4 from entering the nucleus and restricted it to the cytoplasm ($p < 0.001$, TGF-β1 vs. LY364947 + TGF-β1). Treatment with the ATRA and TGF-β1 combination did not inhibit the nuclear localization of SMAD4, thus allowing it to enter the nucleus ($p > 0.05$, TGF-β1 vs. ATRA + TGF-β1). This result indicates that TGF-β1-induced THBS1 suppression by ATRA is not a regulation that occurs outside the nucleus, but rather inside the nucleus.

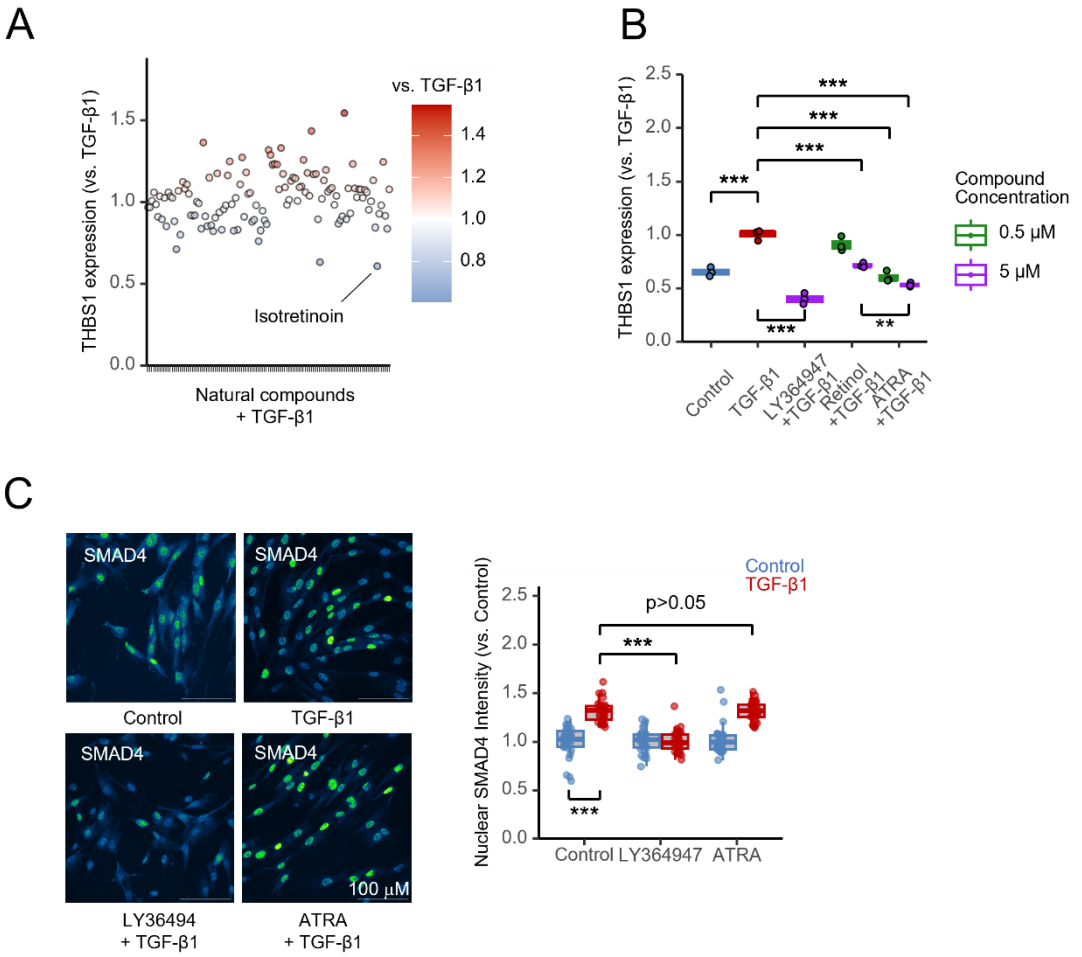


**Figure 3.2.1**: ATRA suppresses THBS1 by nuclear transcriptional regulation.

A) Natural compound screening for THBS1 downregulation. Each compound was combined with TGF-β1, and 119 compounds showing >80% cell viability were used for THBS1 ELISA (n = 1). Relative levels are indicated in accordance with the TGF-β1 (1) value.

B) THBS1 ELISA in compound-treated HFF-1 cell supernatants. The cells were cultured with control (DMEM with 2% fetal bovine serum and 0.1% DMSO vehicle), 4 ng/mL TGF-β1, 5 μM LY36494 with or without 4 ng/mL TGF-β1, 0.5 μM/5 μM retinol with or without 4 ng/mL TGF-β1, or 0.5 μM/5 μM ATRA with or without 4 ng/mL TGF-β1 for 48 h, and supernatants were analyzed; n = 3, **p < 0.01, ***p < 0.001 (Tukey's multiple comparisons).

C) Nuclear localization of SMAD4 by immunofluorescence imaging using HFF-1 cells. The cells were treated with LY36494 or ATRA in combination with or without 4 ng/mL TGF-β1 for 48 h and fixed for immunofluorescence imaging. (Left panel) Representative images; scale bars: 100 μm. (Right panel) Quantification of nuclear SMAD4 intensity in each treatment; In total, 30 images per treatment were randomly analyzed, ***p < 0.001

(Tukey's multiple comparisons).

### 3.2.2 Mutual Inhibition Identified Between TGF-β1 and ATRA

To elucidate nuclear TF regulation by ATRA, I identified the TF network from the DEGs that were upregulated or downregulated in response to treatment with ATRA using the RNA-seq data analyzed by Lisa [94] (Figure 3.2.2A). The TF network analysis identified SMAD3 as a related TF in the ATRA-treated RNA-seq DEGs. Next, I determined the relationship between SMAD and ATRA based on TF activity predicted from RNA-seq using DoRothEA [90] and found that SMAD activity (SMAD3 and SMAD4) decreased after ATRA treatment, whereas ATRA activity (retinoic acid receptors [RARs] and retinoid X receptors [RXRs]) decreased after TGF-β1 treatment (Figure 3.2.2B). These results indicate a mutual inhibitory relationship between ATRA and SMAD signaling. To determine how these TFs are regulated after treatment with ATRA, I examined the binding sites of RARA and RXRA using ChIP-Atlas [114,115], a public TF database that integrates publicly available ChIP-seq data, allowing users to analyze binding sites of specific TFs and epigenetic modifications (Figure 3.2.2C). ATRA binds to RARA and RXRA to form heterodimers to regulate gene transcription [116]; thus, genes commonly annotated in RARA and RXRA ChIP peaks were extracted. The associated genes were identified by annotating neighboring genes at each binding region, and the gene group was divided into two clusters according to the number of peaks present as follows; cluster 1: peak count of 3 or fewer and cluster 2: peak count greater than 3. The KEGG analyses of each cluster revealed that the gene group with many RARA/RXRA binding sites, especially cluster 2, was associated with Hippo signaling, TGF-β signaling, and cellular senescence. These results are consistent with the findings obtained for Yes-associated protein (YAP)1–TEAD1, the major transcriptional mediators of the Hippo pathway [117,118], and SMAD3, an important TF of gene regulation in ATRA treatment (Figure 3.2.2A). These results indicate the possibility that TGF-β signaling- and cellular senescence-related genes are regulated by RARA/RXRA via YAP–TEAD when treated with ATRA. Therefore, I decided to investigate this aspect in detail.

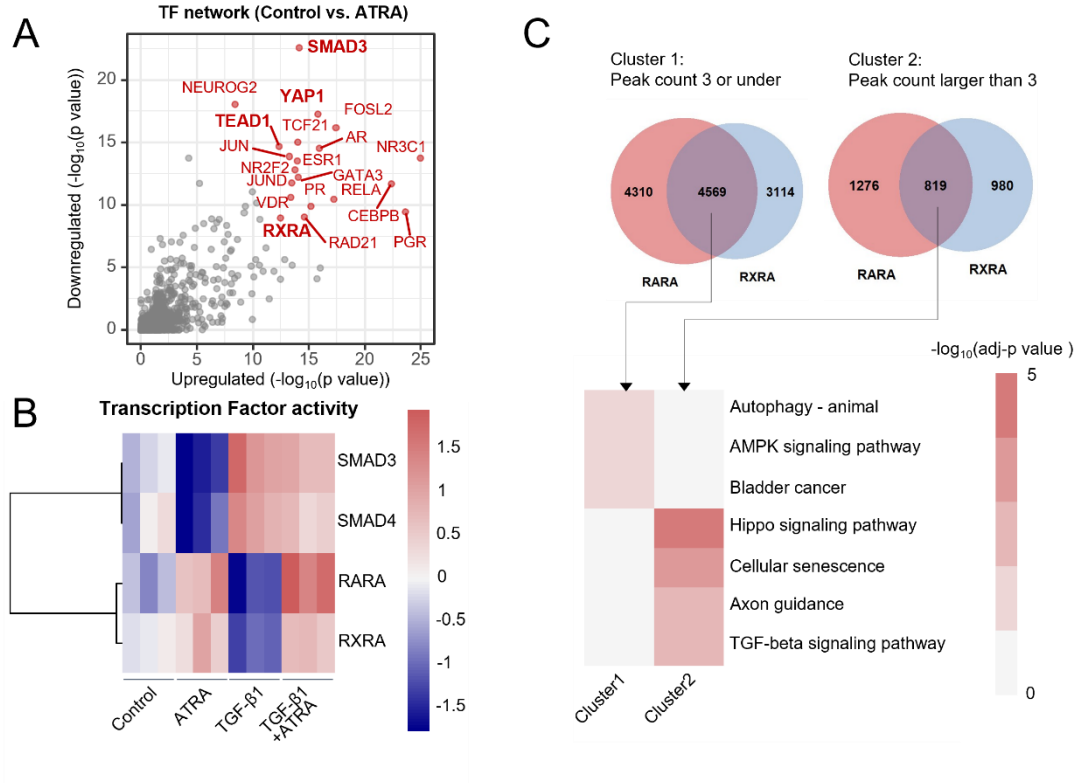


**Figure 3.2.2**: Mutual inhibition identified between TGF-β1 and ATRA.

A) TF network analysis of RNA-seq data derived DEGs (control vs. 5 μM ATRA, |FC| > 1.2, adj-p<0.01) using Lisa. The top 20 TFs are highlighted in red.

B) TF enrichment analysis of RNA-seq data derived from control, 4 ng/mL TGF-β1, or 5 μM ATRA with/without 4 ng/mL TGF-β1-treated HFF-1 cells, focusing on SMAD3, SMAD4, RARA, and RXRA (details in the Methods section). The heatmap shows the normalized TF enrichment scores calculated using DoRothEA analysis.

C) (Upper panel) Venn diagram showing genes near the binding sites of RARA and RXRA using ChIP-Atlas (Cluster 1: peak count 3 or fewer, Cluster 2: peak count greater than 3). (Lower panel) Heatmap showing pathways annotated in the KEGG pathway enrichment analysis. The adj-p was calculated using the BH method with the "compareCluster" function of clusterProfiler.

### 3.2.3 TEAD Family Is Associated with THBS1 Regulation in TGF-β1 and ATRA Stimulation

To identify TFs crucial for the transcriptional regulation of THBS1, I used ATAC-seq data to identify DNA regions with fluctuating peak intensities near THBS1 (Figure 3.2.3A). Open chromatin regions around THBS1 that increased with TGF-β1 treatment and decreased with the combination of TGF-β1 and ATRA were identified. These DNA regions also fluctuated with both

TGF-β1 and ATRA treatments, revealing that a common TF may regulate THBS1 in response to both stimuli. Therefore, I extracted TFs with binding sites near THBS1 that fluctuated with TGF-β1 or ATRA stimulation from ATAC-seq data using ChIP-Atlas (Figure 3.2.3B). I found TEAD4 binding in both conditions. The TF network involved in ATRA-treated DEGs includes TEAD1 and its upstream factor, YAP1, suggesting that YAP-TEAD may play a crucial role in regulating THBS1 (Figure 3.2.2A). To identify TFs associated with THBS1, I constructed a network of TFs involved in TGF-β1-stimulated DEGs using Lisa (Figure 3.2.3C). The graphs show 45 TFs common to the 269 TFs annotated as THBS1-related in "The Signaling Pathway Project" [119], a public dataset summarizing TFs near each gene, and the top 100 TFs associated with genes upregulated by TGF-β1 stimulation. Results suggest that TEAD1, similar to that in ATRA stimulation, is involved in regulating TGF-β1-stimulated DEGs. RXRA is also enriched by TGF-β1 alone, and a binding site is present for RXRA near THBS1, suggesting that retinoic acid suppresses THBS1 expression by transcriptionally regulating it through RXRA. In Figure 2C, gene cluster 2, which contains many RARA/RXRA binding sites, is highly enriched in the Hippo signaling pathway, where TEAD functions as a key TF. To summarize, the RXR/SMAD/TEAD TF network plays a critical role in regulating THBS1.

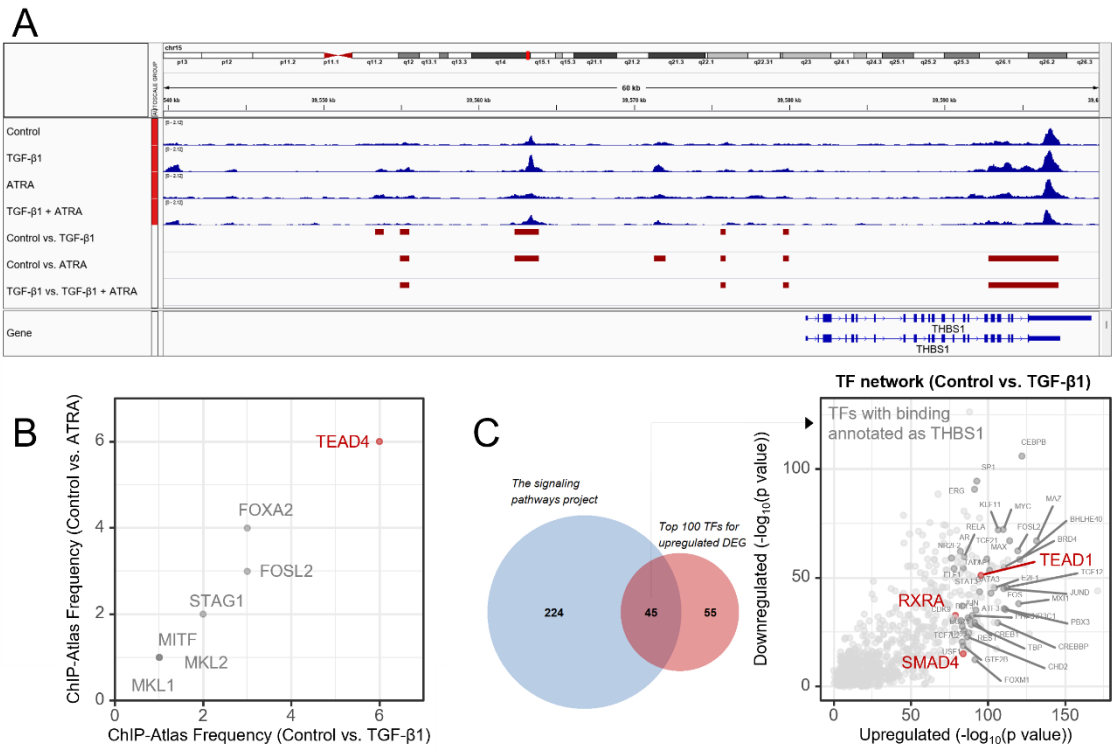


**Figure 3.2.3**: The TF network of retinoid X receptor (RXR)/SMAD/transcriptional enhanced associate domain (TEAD) is associated with stimulation of both TGF-β1 and ATRA.

A) DNA regions with fluctuating ATAC-seq peak intensities near THBS1. IGV traces of ATAC-seq peak intensities for each control, 4 ng/mL TGF-β1, or 5 μM ATRA with/without 4 ng/mL TGF-β1 (blue) are shown, along with DNA regions with fluctuating ATAC-seq peaks (red; |FC| > 1.2). The upper THBS1 ID indicates NM_003246.4, whereas the lower THBS1 ID indicates XM_011521971.3.

B) Extraction of TFs with binding sites near THBS1 using ChIP-Atlas. The fluctuating DNA region derived from ATAC-seq for each TGF-β1 (horizontal axis) and ATRA (vertical axis) treatment was used to determine the frequency of each TF.

C) (Left panel) Venn diagram showing common TFs between THBS1-related TFs from "The Signaling Pathway Project" and the top 100 TFs identified from upregulated DEGs (control vs. 4 ng/mL TGF-β1, FC > 1.2, adj-p<0.01) using Lisa. (Right panel) TF network analysis of RNA-seq data-derived DEGs (control vs. 4 ng/mL TGF-β1, |FC| > 1.2, adj-p < 0.01) using Lisa. RXRA, SMAD4, and TEAD1 are highlighted in red. In total, 45 TFs were identified from the Venn diagram. Except for RXRA, SMAD4, and TEAD1, the other TFs are shown in dark grey.

### 3.2.4 TEAD Is Activated with Senescence of Dermal Fibroblasts

TEAD protein is a major transcriptional mediator of the Hippo pathway, regulating gene expression crucial for development, cell proliferation, regeneration, and tissue homeostasis [117,118]. The transcriptional activity of TEAD is facilitated by its interaction with the co-activators YAP/TAZ, which are regulated in the cytoplasm by phosphorylation via the Hippo pathway. When the Hippo pathway is activated, YAP/TAZ is degraded in the cytoplasm via phosphorylation and TEAD cannot interact with YAP/TAZ [117,118]. In contrast, when the Hippo pathway is inactivated, unphosphorylated YAP/TAZ translocates to the nucleus and interacts with TEAD, forming complexes with TEAD family TFs [120].

Based on the involvement of the RXR/SMAD/TEAD network in TGF-β1 and ATRA treatments, I investigated how these TF activities change during cellular senescence. I calculated TF enrichment scores from the gene expression of each PDL using DoRothEA [90] (Figure 3.2.4A). As shown in previous section 3.1.2, SMAD3 and SMAD4 were found to be activated with increasing PDL. TEAD1 and TEAD4 were also found to be activated with increasing PDL, whereas RARA and RXRA showed attenuated activity with increasing PDL. The upstream analysis of DEGs associated with increased PDL also revealed that TEAD1 and TEAD4 are crucial for the transcriptional regulation of cellular senescence (Figure 3.1.2B). Additionally, ATAC-seq was used to explore the TF binding motifs present in DNA open chromatin regions, which were peaked by increased PDL and TEADs showed strong enrichment (Figure 3.2.4B). I also identified the AP1 family as senescence-associated motifs, including the Jun family (JunB

and Jun-AP1), Fos family (Fos), Fra family (Fra1 and Fra2), and ATF family (Atf3). These results suggest that TEAD-regulated gene expression increases with cellular senescence in dermal fibroblasts, and AP1-TEAD binding motifs are enriched in open chromatin regions.

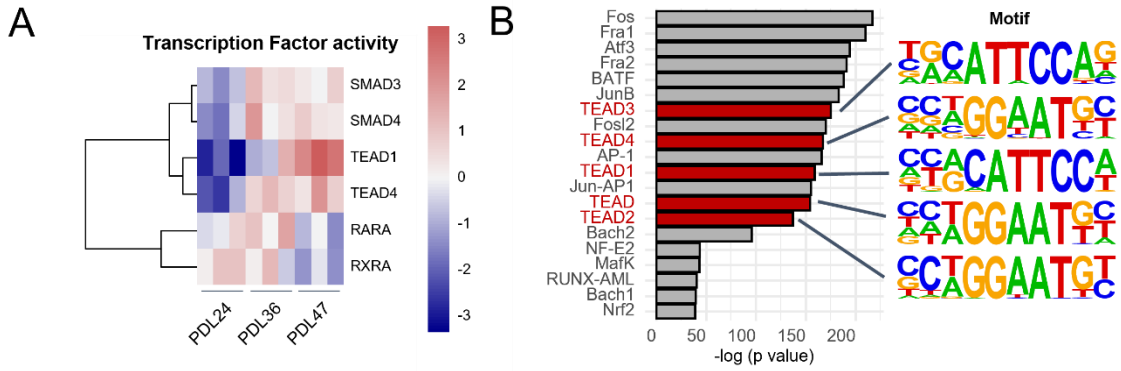


**Figure 3.2.4**: TEAD is activated with senescence of dermal fibroblasts.

A) TF enrichment analysis of RNA-seq data derived from RS-induced HFF-1 cells for SMAD3, SMAD4, TEAD1, TEAD4, RARA, and RXRA. The heatmap shows the normalized TF enrichment scores calculated using DoRothEA analysis.

B) Enriched motifs in the gained ATAC-seq peaks with increasing PDL. The log(adj-p value) and proportion of target sequences with motif were calculated using the "findMotifsGenome.pl" function of HOMER. TEAD motifs are highlighted in red.

### 3.2.5 TEAD Inhibits Senescence of Dermal Fibroblasts

I determined the effect of TEAD inhibition on the regulation of THBS1 expression and SA-β-gal activity as an in vitro senescence marker. Notably, THBS1 expression was upregulated by K-975, a TEAD inhibitor [121], and the combination of K-975 and ATRA resulted in expression levels comparable to those of the controls (Figure 4A). These findings suggest that TEAD functions in a repressive manner on the transcriptional regulation of THBS1. Additionally, ATRA treatment suppresses THBS1 expression by promoting TEAD activity. Lamin-B1 expression, a marker of cellular senescence, was also confirmed and suppressed by K-975. The downregulation of Lamin-B1 expression suggests that TEAD inhibition may promote cellular senescence. When SA-β-gal staining with a TEAD inhibitor was performed using young PDL 24 HFF-1 cells, the number of SA-β-gal-positive cells increased ($p < 0.001$, control vs. K-975) and the expression of SA-β-gal returned to the same level as in the controls with the combination of K-975 and ATRA (Figure 4B). When SA-β-gal staining was performed using senescent PDL 47 HFF-1 cells, ATRA treatment decreased the number of SA-β-gal-positive cells ($p < 0.001$, control vs. ATRA) (Figure 4C). These results indicate that TEAD has an inhibitory role against cellular senescence and that ATRA improves the function of TEAD.

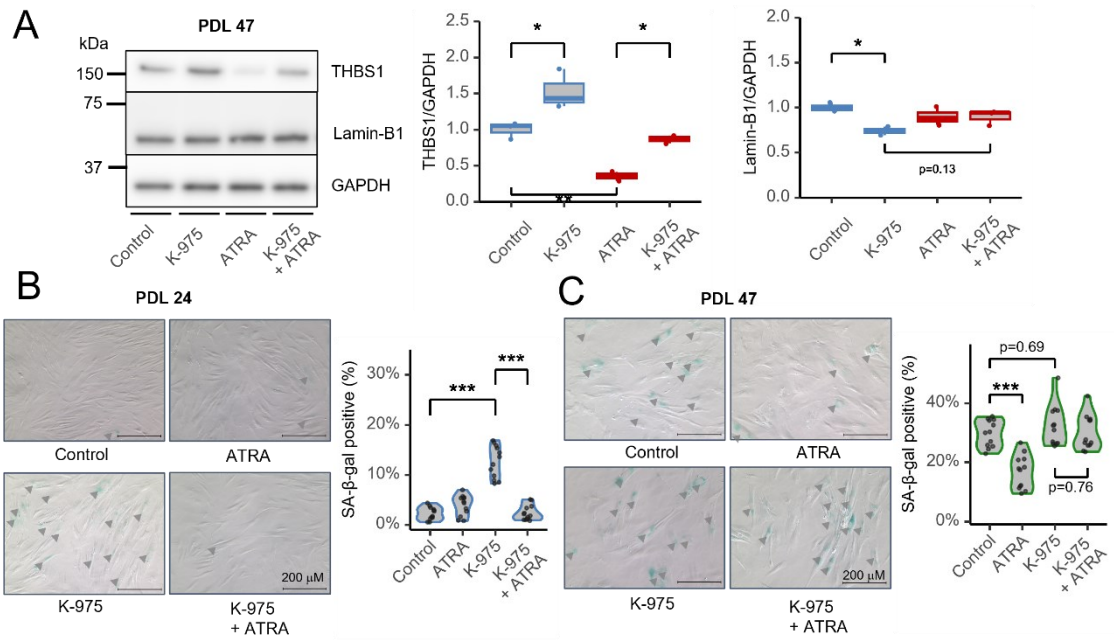


**Figure 3.2.5**: TEAD inhibits the senescence of dermal fibroblasts.

A) Western blotting of THBS1 and Lamin-B1 in K-975 and ATRA stimulated HFF-1 cells (PDL 47). Cells were treated with 1 μM K-975 with or without 5 μM ATRA, cultured for 48 h, and lysates were analyzed. (Left panel) Representative images. (Middle panel) Quantification of THBS1 expression; n = 3, *p < 0.05, **p < 0.01 (Tukey's multiple comparisons). (Right panel) Quantification of Lamin-B1 expression; n = 3, *p < 0.05 (Tukey's multiple comparisons).

B) (Left panel) SA-β-gal staining of 1 μM K-975 with or without 5 μM ATRA stimulated PDL 24 HFF-1 cells. Representative images. SA-β-gal-positive cells are shown by black arrowheads. Scale bar: 200 μm. (Right panel) Quantification of SA-β-gal: SA-β-gal-positive rate (%) = number of SA-β-gal-positive cells/total number of cells × 100. In total, 12 images per treatment were randomly analyzed, ***p < 0.001 (Tukey's multiple comparisons).

C) (Left panel) SA-β-gal staining of control (DMEM with 2% FBS and 0.1% DMSO vehicle), 5 μM ATRA, or 1 μM K-975 with or without 5 μM ATRA stimulated PDL 47 HFF-1 cells. Representative images. SA-β-gal-positive cells are shown by black arrowheads; scale bar: 200 μm. (Right panel) Quantification of SA-β-gal: SA-β-gal-positive rate (%) = (number of SA-β-gal-positive cells/total number of cells) × 100. In total, 12 images per treatment were randomly analyzed, ***p < 0.001 (Tukey's multiple comparisons).

### 3.2.6 Mechanical Stress regulates Senescence of Dermal Fibroblasts

Mechanical stress from extracellular matrix (ECM) stiffness can regulate YAP/TAZ; hence, the Hippo signaling pathway involving TEAD is closely associated with adhesion in the surrounding environment [122,123]. While most cultured plastic plates are very stiff, with elastic moduli ranging from 0.2 to 5.0 GPa [124], a non-negligible difference is found in the human skin dermis at 35 kPa [125]. Additionally, the surrounding environment should be brought closer to skin tissue to determine the role of cellular senescence in TEAD activity. Hence, I examined SA-β-gal activity in senescent human dermal fibroblasts (PDL 47) grown on collagen-coated silicone gel of different stiffness elastic modulus ranging from 0.5 to 32 kPa (Figure 3.2.6). I found that culturing senescent cells on a soft substrate significantly decreases the number of SA-β-gal-positive cells ($p < 0.001$, 2 kPa vs. 32 kPa). Although skin aging decreases the ability to produce collagen and other ECMs [20], my results indicate that the environment surrounding the cells may affect cellular senescence. Furthermore, the effects of ATRA and K-975 on SA-β-gal staining were confirmed at different substrate stiffnesses (2 kPa and 32 kPa). Under 2 kPa conditions, no changes were found with ATRA. However, I found that TEAD inhibition with K-975 increased SA-β-gal positivity ($p < 0.001$, control vs. K-975). In contrast, at 32 kPa, ATRA decreased SA-β-gal positivity, whereas K-975 showed no significant effect ($p = 0.49$, control vs. K-975). These results indicate that TEAD inhibition increases SA-β-gal positivity when initial SA-β-gal levels are low, whereas ATRA has no effect (Figures 3.2.5B). When initial SA-β-gal levels are high, TEAD inhibition does not significantly change SA-β-gal positivity, but ATRA can suppress it (Figures 3.2.5C).

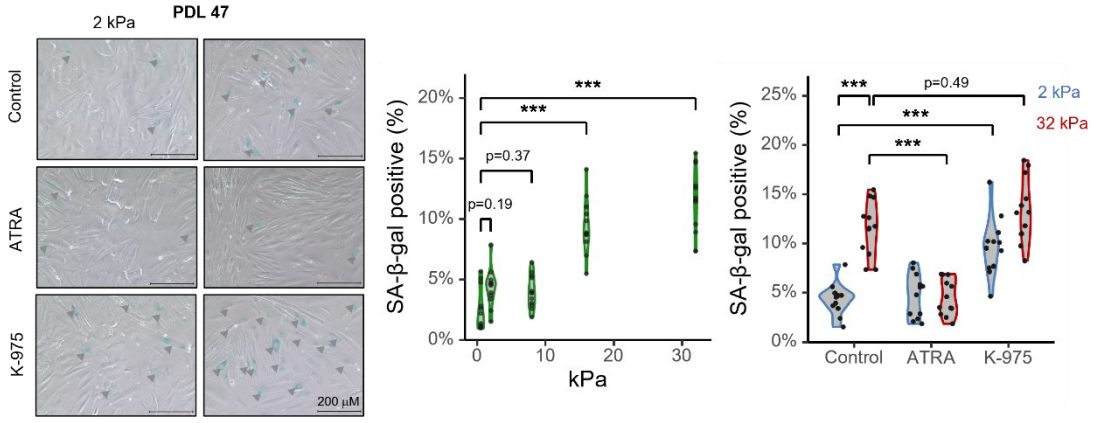


**Figure 3.2.6**: Mechanical stress regulates senescence of dermal fibroblasts.

(Left panel) SA-β-gal staining of control (DMEM with 2% FBS and 0.1% DMSO vehicle), 5 μM ATRA, or 1 μM K-975 stimulated PDL 47 HFF-1 cells cultured on substrates with elastic moduli of 2 kPa or 32 kPa. Representative images. SA-β-gal-positive cells are shown by black arrowheads; scale bar: 200 μm. (Middle panel) Quantification of SA-β-gal under control (DMEM with 2% FBS and 0.1% DMSO vehicle) conditions at various elastic moduli of 0.5, 2, 8, 16, and 32 kPa for PDL 47 HFF-

1 cells. In total, 12 images per treatment were randomly analyzed, ***$p < 0.001$ (Tukey's multiple comparisons). (Right panel) Quantification of SA-β-gal staining of control (DMEM with 2% FBS and 0.1% DMSO vehicle), 5 μM ATRA, or 1 μM K-975 stimulated PDL 47 HFF-1 cells cultured on substrates with elastic moduli of 2 kPa or 32 kPa. In total, 12 images per treatment were randomly analyzed, ***$p < 0.001$ (Tukey's multiple comparisons).

# 4. DISCUSSION

In this study, I investigate the regulatory network in skin aging using multi-omics and mechanistic modeling approaches. Inflammation and fibrosis have been shown to characterize senescence in *in vivo* [126]. Multi-omics analysis revealed the roles of the TGF-β and YAP-TEAD signaling pathways in the senescence of dermal fibroblasts. TGF-β signaling pathway regulates fibrosis and the activation of YAP and TAZ, transcriptional coactivators of TEAD, which contribute to pulmonary fibrosis by activating the profibrotic functions of lung fibroblasts [127]. Studies have shown the involvement of the TGF-β signaling pathway in cellular senescence. TGF-β pathway activation can cause senescence in surrounding cells through the TGF-β1 protein [111,128]. Transcription of p21 can be activated by the TGF-β pathway [129]. Multi-omics analysis of RS-senescent WI-38 cells (human lung fibroblasts) showed activation of the TGF-β pathway and YAP-TEAD activity [130]. The transcriptome analysis of aged mouse skin highlights the TGF-β pathway as a regulator [131]. Together with my findings, these results support that the TGF-β pathway is a major signaling pathway and TEAD is involved in human skin aging. On contrary, previous papers reported TGF-β signaling pathway decline with human skin aging [20,132]. TβRII mRNA levels are reported to be reduced in aged (80+ years) compared to young (20-30 years) dermis, along with photoaged human skin, as determined by laser capture microdissection coupled with quantitative real-time RT-PCR [133]. Therefore, prior studies have concluded a decrease in TGF-β signaling from a macroscopic perspective using skin tissue in response to skin aging, while I have concluded an increase in TGF-β signaling from a microscopic examination using a cellular aging model of dermal fibroblasts. This contradiction highlights the complexity of skin aging, suggests that the role of TGF-β signaling in skin aging may vary depending on the context and scale of the analysis.

The association between aging and Hippo signaling is well-documented [134,135]. Previous study has shown that YAP and TAZ activities decrease with aging, protecting the skin from premature aging in mouse dermal fibroblasts [136]. A whole-genome CRISPR knockout screen showed that the YAP–TEAD pathway affects cell viability in senescent cells [137]. Another study performed a multi-omics analysis of the RS model in mouse fibroblasts and identified AP-1 and TEAD1 as key regulatory TFs [138]. Other studies have reported that AP-1 directly interacts with TEAD [139,140]. In human dermal fibroblasts, decreased YAP/TAZ levels activate AP-1, which suppresses the TGF-β pathway via the induction of SMAD7 [141]. In my analysis, I found that the AP-1 family, including the Jun family (e.g., JUN, JUND), Fos family (e.g., FOS), and ATF family (e.g., ATF3), is enriched with the increase in PDL, indicating the involvement of AP-1 in TEAD regulation in dermal fibroblast senescence. A previous study showed that *Tead1* knockdown in mouse dermal fibroblasts attenuates SA-β-gal activity [138].

However, the knockdown of YAP and TEAD1/3/4 increased SA-β-gal activity in IMR90 cells (human lung fibroblasts) [142]. My results showed that TEAD inhibitor treatment promotes SA-β-gal activity. The association between YAP-TEAD and senescence indicates that even identical fibroblasts can play different roles in aging based on their species and organs of origin. Nevertheless, these results should be confirmed in human skin-derived cells to determine the role of YAP-TEAD in human skin aging.

In addition, my analysis identified an age-related enrichment of estrogen receptor 2 (ESR2). Knockout of the human *ESR2* gene reduced the expression of human *THBS1* mRNA [143] and its ligand 17β-estradiol induced *THBS1* mRNA expression [144]. 17β-estradiol decreased *Fmod* mRNA expression in the frontal cortex of rats [145]. These results suggest that ESR2 may also be involved in the regulation of THBS1 and FMOD in dermal senescence. Furthermore, USP11 has been reported to stabilize p21 levels in a p53-independent manner [89]. As p53 expression did not decrease with increasing PDL in my study, it is possible that changes in USP11 are responsible for the downregulation of p21 in the late PDL.

In previous reports, the analysis of human dermal fibroblast mRNA suggested that *THBS1* expression increased with age [146]. Among 998 proteins that showed an age-dependent secretion pattern, THBS1 was upregulated with skin aging [147]. These reports implicated THBS1 as a biomarker of skin aging but did not directly demonstrate its function. Collectively, my findings and previous findings suggest that THBS1 expression plays a vital role as a universal phenotype in skin aging. In addition, THBS1 was reported to promote senescence in endothelial cells [148,149]. Given the strong relationship between THBS1 and age-associated diseases [98], my current findings on THBS1 have potential applications beyond skin aging.

In contrast, the expression of FMOD seems to be heterogeneous among reports of skin aging. I found that the expression of FMOD decreased with the senescence of dermal fibroblasts. Proteomic analysis of human skin punch biopsies showed that FMOD protein expression decreased with age [150]. In contrast, an earlier analysis of skin-fibroblast mRNA also suggested that FMOD increases with age [146]. FMOD expression was upregulated with increasing age and senescence in the public RNA-seq dataset, which contradicts my validation. A possible explanation for this difference in the senescence tendency of FMODs in the same HFF-1 cell line could be the variation in culture conditions, such as the medium glucose level. Inconsistencies in reports on FMOD regulation may also be due to the differences between proteomic and transcriptomic data in aging, suggesting that their expressions are poorly correlated and that mRNA profiling alone does not provide the complete picture [151].

My findings suggest that both SMAD activation and c-Fos/c-Jun binding to DNA are required to regulate THBS1 expression in dermal fibroblasts. In earlier studies, THBS1 was regulated by the SMAD3 binding site of the THBS1 promoter [109]; c-Jun, but not c-Fos, was involved in AP-

1 activity at the AP-1 binding site of the THBS1 promoter in human hepatocarcinoma cell lines [152]. Various TFs (e.g., NF-κB, USF, E2F1, AP-1, EGR1, and SP1) have been reported to bind to the promoter region of THBS1 [153]; therefore, the TFs associated with THBS1 may vary among cell lines. In addition, I found that TEAD is involved in the transcriptional regulation of THBS1 in dermal fibroblasts. A bioinformatics analysis using MCF7 cells (breast cancer) identified THBS1 as a direct transcriptional target of YAP-TEAD [154]. WI-38 and HFF-1 cells show TGF-β and TEAD activation with RS; however, TEAD inhibition decreases THBS1 in WI-38 cells [130]. However, my TEAD inhibition experiment with dermal fibroblasts increased THBS1. My findings indicate that while TEAD acts as a repressor of THBS1 in dermal fibroblasts, it may function differently in other cell types, including WI-38 and HFF-1 cells, highlighting the complexity of the Hippo signaling pathway and its context-dependent roles in cellular senescence and aging. Subsequent investigations into the molecular interactions among TEAD, THBS1, and other regulatory factors in various cell types can provide deeper insights into the tissue-specific functions of TEAD and its implications in skin aging and potential therapeutic interventions.

Meanwhile, FMOD expression in dermal fibroblasts was found to be regulated by the VEGF–Raf–ERK pathway. Previous reports have indicated that FMOD was regulated by the Wnt/β-catenin pathway in human breast cancer cell lines [155], MAPK/AP-1 pathway in human pancreatic stellate cells [156], and TGF-β2 in rat pericytes [157]. These results suggest that FMOD regulation may vary in different cells, tissues or environments.

Our bifurcation analysis of TGF-β1, THBS1, and FMOD network indicated that a binary high-/low-TGF-β1 switch. Earlier studies identified a bistable switch that regulates TGF-β1 activation in liver fibrosis [158] and asthmatic airways [159]. In addition to these diseases, the bifurcation analysis may be useful in qualitatively capturing other phenomena of senescence.

Several mathematical models have been reported for the TGF-β signaling pathway [86,160,161]. Nevertheless, my model is invaluable because it reflects unbiased data-driven insights into the gene regulatory network of skin aging, combined with the previous models. Computational simulation of skin aging showed that THBS1 responded sensitively while FMOD was robustly regulated with any input. These results suggest that THBS1 is a more promising drug target than FMOD. The sensitivity analysis further confirmed that the model-predicted sensitive response, i.e., the complex formation by SMAD4, was conserved across 30 independent parameter sets, suggesting that parameter identifiability does not affect the uncertainty of model outputs. In the siRNA-based SMADs KD experiments, knockdown of the SMAD2–SMAD3 combination (besides SMAD4) significantly reduced THBS1, which may indicate a functional redundancy of SMAD2 and SMAD3. On the contrary, when considering practical applications in drug development, focusing on a single target (SMAD4) is more suitable than developing drugs for two alternative targets, SMAD2 and SMAD3. Experimental evidence has shown that inhibition

of SMAD4 complex formation has a restorative effect on the aging phenotype (i.e., SA-β-gal and Lamin-B1), and that its effects go beyond THBS1 regulation. This approach of targeting THBS1 by inhibiting SMAD4 complex formation will open new avenues for skin aging research.

ATRA, also known as tretinoin, is considered the clinical gold standard for addressing skin aging-related concerns due to its ability to reduce fine lines, coarse wrinkles, and pigmentation, and improve skin texture [162]. ATRA influences the photodamage of the skin by promoting the production of collagen I, an ECM protein that provides structure and elasticity to the skin [163]. Furthermore, it plays a role in regulating epidermal thickening, proliferation, and differentiation, thereby maintaining the health of the epithelium and preventing skin aging [163,164]. Immunohistochemistry assay showed a significant increase in the number of RAR-expressing epidermal keratinocytes in aged photo-protected human skin compared to young skin [165]. Nevertheless, no change was found in RAR expression in dermal fibroblasts [165]. Retinoic acid inhibits collagenase and gelatinase expression in human dermal fibroblasts [166]. A TF network between retinoid receptors and the AP-1 family has been reported [167]. AP-1, which binds to the promoter region of matrix metalloproteinases collagenase and gelatinase and is triggered by UVB irradiation, is repressed by nuclear retinoid receptors [168,169]. Despite these findings, the mechanisms underlying the transcriptional regulation of RARs and RXRs in skin aging have yet to be elucidated.

My results revealed mutual inhibition between SMAD activity and RARA/RXRA activities. I found that ATRA downregulates THBS1 via the regulation of the RXR/SMAD/TEAD TF network. Previous study has reported that retinoic acids exhibit anti-fibrotic activity in scleroderma fibroblasts where retinoic acids downregulated TGF-β1 expression [170]. In human tendon fibroblasts, ATRA inhibits SMAD2 and SMAD3 phosphorylation induced by TGF-β1 [171]. In this study, immunostaining results showed that ATRA does not affect the nuclear influx of SMAD4 induced by TGF-β1, indicating that multiple pathways may be present for the suppression of TGF-β1 by ATRA. However, retinoids have been reported to increase TGF-β activity [172]. Regarding the regulation of THBS1, a previous study reported that some cell lines upregulate or downregulate THBS1 expression in response to retinoic acid [173]. These findings suggest that crosstalk between TGF-β signaling and the retinoic acid signaling pathway is context-dependent, sometimes promoting and other times inhibiting the pathway.

Tissue cells sense and respond to the stiffness of their substrate [174]. Regarding the effect of substrate stiffness on senescence, soft substrates can delay senescence and maintain the proliferation of human mesenchymal stem cells during long-term expansion [175]. A previous study reported that senescent mesenchymal stromal cells showed reduced markers of the senescence-associated secretory phenotype (SASP) when cultured on soft substrates compared with those in cells cultured on tissue culture plastic [176]. In premature senescence-induced

dermal fibroblasts, cells cultured on soft substrates (0.5 kPa) did not express p21 and p16 compared with those in cells cultured on stiff substrates (4 GPa) [177]. These findings suggest that the stiffness of the culture substrate may also affect cellular senescence induced by the RS model in dermal fibroblasts. My findings on SA-β-gal activity in human dermal fibroblasts grown in environments with different stiffness suggest that senescent human dermal fibroblasts induced by the RS model, when cultured on a soft substrate, can significantly decrease the number of SA-β-gal-positive cells due to the involvement of TEAD activity. Previous studies [177] have not elucidated the mechanisms underlying how dermal senescent cells sense and respond to mechanical stimuli. Another study suggests a link between reduction of mechanical force, downregulation of the TGF-β signaling pathway and skin aging, but does not show the regulatory mechanism behind it [178]. Nevertheless, my findings suggest that substrate stiffness affects the senescence phenotype via TEAD regulation. The involvement of the retinoic acid receptor and TEAD in dermal fibroblast senescence provides an important background for therapeutic intervention in this field.

Big data is increasingly being used to study real-world diseases and disorders. In this regard, the present study represents a major advancement in the study of skin aging and the regulatory mechanisms of retinoic acid.

# 5. CONCLUSION

My findings indicate that the TGF-β1-SMAD axis is crucial for regulating cellular senescence in human dermal fibroblasts. I found that TGF-β1 is the most enriched upstream regulator of senescence-related genes. Additionally, activation of this pathway, accompanied by epigenetic changes, is induced by RS. Furthermore, multi-omics analysis revealed THBS1 as a major gene in skin aging and cellular senescence, with ATRA effectively suppressing THBS1 through nuclear transcriptional regulation. Suppression of THBS1 by ATRA occurs through a mutual inhibitory relationship between ATRA and SMAD signaling, involving the RXR/SMAD/TEAD transcription factor network. Moreover, I found that TEAD, a transcription factor enriched in senescence-associated chromatin regions and increased by ATRA, inhibits cellular senescence. Importantly, senescent human dermal fibroblasts grown on a soft substrate significantly decreased the number of SA-β-gal-positive cells through the involvement of TEAD activity. My findings provide valuable insights into the potential therapeutic targets for age-related skin issues and highlight the importance of the Hippo signaling pathway in regulating dermal fibroblast senescence.

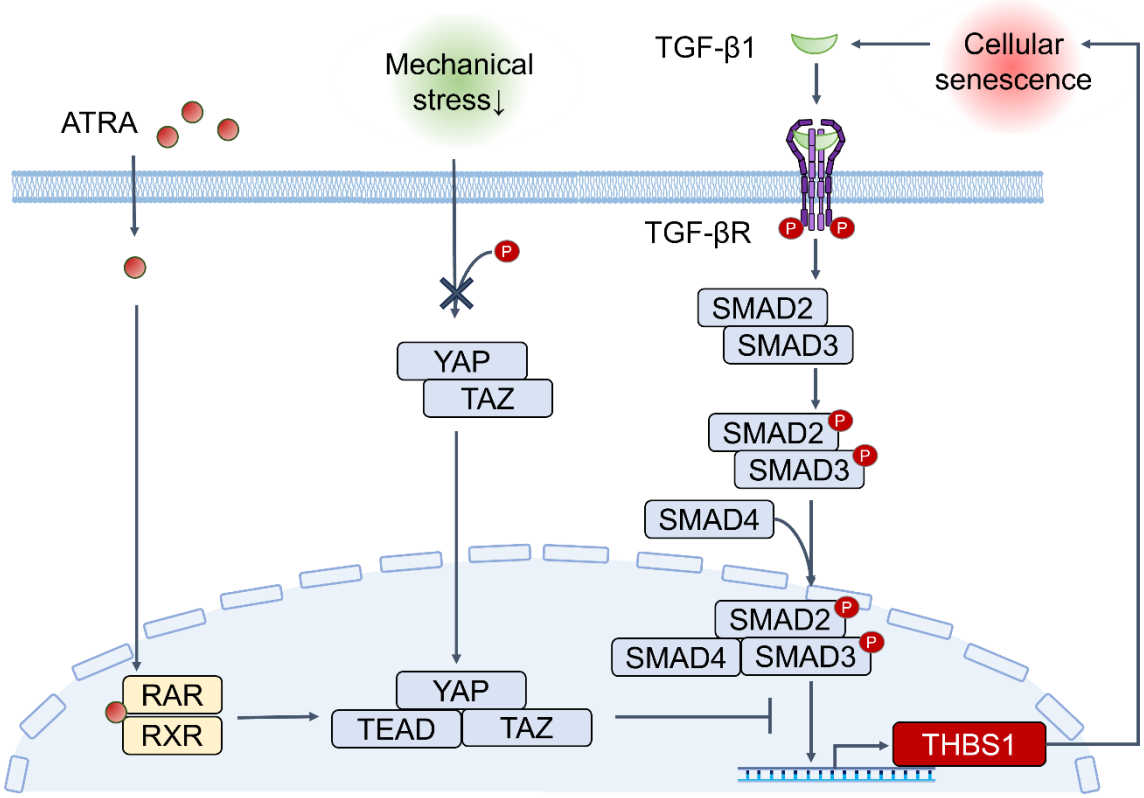


**Figure 5**: Schematic of the transcription factor network of RXR, SMAD, and TEAD in THBS1 regulation in dermal fibroblasts senescence.

# 6. LIMITATIONS OF THE STUDY

The mechanisms regulating FMOD expression in the dermal fibroblasts remain unclear. Although the involvement of VEGF pathway was demonstrated, this study does not rule out the possibility that FMOD expression may also be regulated by other ligands. Additionally, I used an anonymous transcription factor for FMOD in our mathematical model. Furthermore, the role of endogenous TGF-β signaling in senescent transcripts is yet to be elucidated.

Further research is necessary to elucidate the factors regulating FMOD in skin aging, especially because the regulation of FMOD may vary in different cells and tissues, or in different environments.

Although the involvement of mechanical stress in the senescence of dermal fibroblasts has been indicated, further validation with other markers of cellular senescence is required. Moreover, while the RXR/SMAD/TEAD transcription factor network has been implicated in dermal fibroblast senescence and THBS1 regulation, the mechanism of TEAD activation by ATRA remains unclear and warrants further investigation.

# 7. KEY RESOURSE TABLE

**Table 7.1**: Detailed Information on Materials Used in This Study

| **REAGENT or RESOURCE** | **SOURCE** | **IDENTIFIER** |
|---|---|---|
| Antibodies | | |
| Anti-THBS1 | Cell Signaling Technology | Cat# 37879; RRID: AB_2799123 |
| Anti-THBS1 | Abcam | Cat# ab85762, RRID: AB_10674322 |
| Anti-FMOD | ProteinTech | Cat# 60108-1-Ig; RRID: AB_2105538 |
| Anti-Lamin B1 | ProteinTech | Cat# 12987-1-AP; RRID: AB_2136290 |
| Anti-p53 | Cell Signaling Technology | Cat# 2524; RRID: AB_331743 |
| Anti-p21 | Cell Signaling Technology | Cat# 2946; RRID: AB_2260325 |
| Anti-c-Fos | Cell Signaling Technology | Cat# 2250; RRID: AB_2247211 |
| Anti-c-Jun | Cell Signaling Technology | Cat# 9165; RRID: AB_2130165 |
| Anti-SMAD2 | Cell Signaling Technology | Cat# 5339; RRID: AB_10626777 |
| Anti-phosphorylated SMAD2 (Ser465/467) | Cell Signaling Technology | Cat# 3108; RRID: AB_490941 |
| Anti-SMAD3 | Cell Signaling Technology | Cat# 9523; RRID: AB_2193182 |
| Anti-phosphorylated SMAD3 (Ser423/425) | Cell Signaling Technology | Cat# 9520; RRID: AB_2193207 |

| | | |
|---|---|---|
| Anti-SMAD4 | Cell Signaling Technology | Cat# 46535; RRID: AB_2736998 |
| Anti-phosphorylated Akt (Ser473) | Cell Signaling Technology | Cat# 9271; RRID: AB_329825 |
| Anti-pan Akt | Cell Signaling Technology | Cat# 2920; RRID: AB_1147620 |
| Anti-USP11 | Abcam | Cat# ab109232; RRID: AB_10862711 |
| Anti-GAPDH | Medical & Biological Laboratories | Cat# M171-3; RRID: AB_10597731 |
| Anti-GAPDH | ProteinTech | Cat# 10494-1-Ap; RRID: AB_2263076 |
| Anti-H3K27Ac | Abcam | Cat# ab177178; RRID: AB_2828007 |
| Anti-IgG (H+L chain) (Mouse) pAb-HRP | Medical & Biological Laboratories | Cat# 330; RRID:AB_2650507 |
| Anti-IgG (H+L chain) (Rabbit) pAb-HRP | Medical & Biological Laboratories | Cat# 458; RRID:AB_2827722 |
| Goat Anti-Rabbit IgG H&L (Alexa Fluor® 594) | Abcam | Cat# ab150080, RRID:AB_2650602 |
| Goat Anti-Rabbit IgG H&L (Alexa Fluor™ Plus 488) | Thermo Fisher Scientific | Cat# A32731, RRID: AB_2633280 |
| Chemicals, Peptides, and Recombinant Proteins | | |
| D-PBS (-) (1X) | Nacalai Tesque | Cat# 14249-24 |
| HBSS | Thermo Fisher Scientific | Cat# 14025092 |
| Dulbecco's modified Eagle's medium | ATCC | Cat# 30-2002 |
| Fetal bovine serum | Corning | Cat# 35-010-CV |

| | | |
|---|---|---|
| Goat serum | Thermo Fisher Scientific | Cat# 16210–064 |
| Antibiotic–antimycotic | Thermo Fisher Scientific | Cat# 15240062 |
| Trypsin/EDTA | ATCC | Cat# 30-2101 |
| BAMBANKER® | NIPPON Genetics | Cat# CS-04-001 |
| RIPA Buffer | Thermo Fisher Scientific | Cat# 89900 |
| Halt™ Protease and Phosphatase inhibitor | Thermo Fisher Scientific | Cat# 78442 |
| Trypan blue | Thermo Fisher Scientific | Cat# 15250-061 |
| Cell counter | WakenBtech | Cat# WC2-100 |
| Hoechst® 33342 | DOJINDO | Cat# 346-07951 |
| Opti-MEM™ I | Thermo Fisher Scientific | Cat# 31985-070 |
| Lipofectamine RNAiMax | Thermo Fisher Scientific | Cat# 13778150 |
| Precast gel 7.5–15% | Nacalai Tesque | Cat# 13066-44 |
| Wide Precast Gel 7.5–15% | Biocraft | Cat# MDG-287 |
| Tris/Glycine/SDS Buffer | Bio-Rad | Cat# 1610732 |
| 4× Laemmli sample buffer | Bio-Rad | Cat# 1610747 |
| 2-Mercaptoethanol | Bio-Rad | Cat# 1610710 |
| Precision Plus Protein IsternC blotting standard | Bio-Rad | Cat# 1610376 |

| | | |
|---|---|---|
| Clarity Istern ECL Substrate | Bio-Rad | Cat# 1705060 |
| Clarity Max Istern ECL Substrate | Bio-Rad | Cat# 1705062 |
| Blocking buffer | Bio-Rad | Cat# 12010020 |
| iBlot®2 PVDF | Thermo Fisher Scientific | Cat# IB24001 |
| Reconstitution buffer (0.1% BSA in 4 mM HCl PBS) | R&D Systems | Cat# RB04 |
| Recombinant human TGF-β1 | R&D Systems | Cat# 7754-BH-005 |
| Recombinant human TGF-β2 | ProteinTech | Cat# HZ-1092 |
| Recombinant human TGF-β3 | ProteinTech | Cat# HZ-1090 |
| Recombinant human EGF | PeproTech | Cat# AF-100-15 |
| Recombinant human b-FGF | R&D Systems | Cat# 233-FB-025 |
| Recombinant human PDGF-BB | ProteinTech | Cat# HZ-1308 |
| Recombinant human THBS1 | R&D Systems | Cat# 3074-TH-050 |
| Recombinant human FMOD | Abcam | Cat# ab152392 |
| Recombinant human VEGF165 | ProteinTech | Cat# HZ-1038 |
| Dimethyl sulfoxide | Fujifilm | Cat# 041-29351 |
| all-*trans*-retinoic acid | Selleck Chemicals | Cat# S1653 |
| Retinol | LKT Labs | Cat# R1876 |
| LY364947 | Fujifilm | Cat# 123-05981 |
| Akt inhibitor VIII | Cayman | Cat# 14870 |

| | | |
|---|---|---|
| | Chemical | |
| LY294002 | Calbiochem | Cat# 440202 |
| T-5224 | Selleck Chemicals | Cat# S8966 |
| Tocriscreen Kinase Inhibitor Toolbox | Tocris Bioscience | Cat# 3514 |
| ZM306416HCl | Tocris Bioscience | Cat# 3514-2499 |
| Ki8751 | Tocris Bioscience | Cat# 3514-2542 |
| GW5074 | Tocris Bioscience | Cat# 3514-1381 |
| U0126 | Tocris Bioscience | Cat# 3514-1144 |
| SB 431542 | Tocris Bioscience | Cat# 3514-1614 |
| K-975 | Selleck Chemicals | Cat# E1329 |
| Formaldehyde | Thermo Fisher Scientific | Cat# 28908 |
| Paraformaldehyde | Electron Microscopy Science | Cat # 15710 |
| HCS CellMask™ Stains | Thermo Fisher Scientific | Cat# H32721 |
| Triton® X-100 | NACALAI TESQUE | Cat# 35501-15 |
| Proteinase K | Thermo Fisher Scientific | Cat# 26160 |
| Dispase® II | Roche | Cat# 04942078001 |
| PureCol Atelocollagen Solution | Advanced BioMatrix | Cat#5005-100ML |
| Critical Commercial | | |

| Assays | | |
|---|---|---|
| Pierce™ BCA Protein Assay Kit | Thermo Fisher Scientific | Cat# 23227 |
| NucleoSpin® RNA kit | Macherey-Nagel GmbH & Co. | Cat# 740955 |
| ReverTra Ace® qPCR RT Master Mix | Toyobo Life Science | Cat# FSQ-201 |
| KOD SYBR® qPCR kit | Toyobo Life Science | Cat# QKD-201 |
| SimpleChIP® Enzymatic Chromatin IP kit | Cell Signaling Technology | Cat# 9003 |
| iDeal ChIP-seq kit for Histones | Diagenode | Cat# C01010171 |
| MinElute® PCR Purification Kit | Qiagen | Cat# 28004 |
| Bioanalyzer Agilent High-Sensibility DNA Kit | Agilent | Cat# 5067-4626 |
| NEBNext® Poly(A) mRNA Magnetic Isolation Module | New England Biolabs | Cat# E7490 |
| NEBNext® Ultra™ ll Directional RNA Library Prep Kit | New England Biolabs | Cat# E7760 |
| ATAC-Seq Kit | Active Motif | Cat# 53150 |
| NEBNext® Ultra II DNA Library Prep Kit for Illumina | New England Biolabs | Cat# 7645 |
| Cell Counting Kit-8 | DOJINDO | Cat# 343-07623 |
| SA-β-gal Detection Kit | BioVision | Cat# K320-250 |
| SA-β-gal Detection Kit | Abcam | Cat# ab65351 |

| | | |
|---|---|---|
| CycLex® Cellular BrdU ELISA Kit Ver.2 | Medical & Biological Laboratories | Cat# CY-1142V2 |
| CytoSoft® 6-well plates | Advanced BioMatrix | Cat# 5190-7EA |
| THBS1 ELISA Kit | R&D Systems | Cat# DTSP10 |
| FMOD ELISA Kit | Abcam | Cat# ab275895 |
| TGF-β1 ELISA Kit | R&D Systems | Cat# DB100B |
| VEGF ELISA Kit | R&D Systems | Cat# DVE00 |
| SMAD2 ELISA Kit | Abcam | Cat# ab260065 |
| SMAD3 ELISA Kit | Abcam | Cat# ab264624 |
| SMAD4 ELISA Kit | Abcam | Cat# ab253211 |
| IL-6 ELISA Kit | R&D Systems | Cat# D6050 |
| IL-8 ELISA Kit | Abcam | Cat# ab214030 |
| Deposited Data | | |
| RNA-seq: HFF-1 (PDL 24, PDL 36, PDL 47) Treatment: Control | This Paper | Submission: DRA016119 BioProject: PRJDB15707 |
| RNA-seq: HFF-1 (PDL 24, PDL 36, PDL 47) Treatment: 4 ng/mL TGF-β1 | This Paper | Submission: DRA017188 BioProject: PRJDB15707 |
| ChIP-seq: H3K27Ac HFF-1 (PDL 24, PDL 36, PDL 47); Input HFF-1 (PDL 24, PDL 36, PDL 47) Treatment: Control | This Paper | Submission: DRA016119 BioProject: PRJDB15707 |
| ATAC-seq: HFF-1 (PDL 24, PDL 36, PDL 47) Treatment: Control | This Paper | Submission: DRA016119 BioProject: PRJDB15707 |
| ATAC-seq: HFF-1 (PDL | This Paper | Submission: DRA017188 |

| | | |
|---|---|---|
| 24)<br>Treatment: 4 ng/mL TGF-β1 | | BioProject: PRJDB15707 |
| RNA-seq: HFF-1 (PDL 24) initial condition | This Paper | Submission: DRA016119<br>BioProject: PRJDB15707 |
| The code for bioinformatics analysis and mathematical modeling | This Paper | https://github.com/okadalabipr/Haga2023 |
| Experimental models: Cell lines | | |
| Human dermal fibroblast HFF-1 | ATCC | Cat# SCRC-1041; RRID: CVCL_3285 |
| Human dermal fibroblast BJ | ATCC | Cat# CRL-2522; RRID: CVCL_3653 |
| Experimental models: Organisms/Strains | | |
| Frozen human full thickness skin | Biopredic International | Cat# TRA1FTR0, TRA1FTR2 |
| Oligonucleotides | | |
| qRT-PCR forward primer: *THBS1* 5′-TCCCCATCCAAAGCGTCTTC-3′ | This paper | N/A |
| qRT-PCR reverse primer: *THBS1* 5′-ACCACGTTGTTGTCAAGGGT-3′ | This paper | N/A |
| qRT-PCR forward primer: *FMOD* 5′-GGACGTGGTCACTCTCTGAA-3′ | This paper | N/A |
| qRT-PCR reverse primer: *FMOD* 5′-GGCTCGTAGGTCTCATACGG-3′ | This paper | N/A |

| | | |
|---|---|---|
| qRT-PCR forward primer: *GAPDH* 5′-GTCTCCTCTGACTTCAACAGCG-3′ | OriGene | Cat# HP205798 |
| qRT-PCR reverse primer: *GAPDH* 5′-ACCACCCTGTTGCTGTAGCCAA-3′ | OriGene | Cat# HP205798 |
| ON-TARGET plus Non-targeting siRNA | Dharmacon | Cat# D-001810-02-20 |
| ON-TARGET plus Human c-Fos siRNA – SMARTpool | Dharmacon | Cat# L-003265-00-0010 |
| ON-TARGET plus Human c-Jun siRNA – SMARTpool | Dharmacon | Cat# L-003268-00-0010 |
| ON-TARGET plus Human SMAD2 siRNA – SMARTpool | Dharmacon | Cat# L-003561-00-0020 |
| ON-TARGET plus Human SMAD3 siRNA – SMARTpool | Dharmacon | Cat# L-020067-00-0020 |
| ON-TARGET plus Human SMAD4 siRNA – SMARTpool | Dharmacon | Cat# L-003902-00-0020 |
| Software and Algorithms | | |
| CellProfiler ver. 4.2.1 | Stirling et al. [179] | https://cellprofiler.org/ RRID: SCR_007358 |
| ImageJ Fiji version 1.52p | Schindelin et al. [180] | http://fiji.sc RRID: SCR_002285 |
| Biomass version 0.5.2 | Imoto et al. [68,88] | https://github.com/biomass-dev/biomass RRID: N/A |
| Gnuplot vesion 5.4 | Williams et al. [181] | http://www.gnuplot.info/ RRID: SCR_008619 |
| R version 4.2.1 | The R Foundation | https://r-project.org RRID: SCR_001905 |

| | | |
|---|---|---|
| QIAGEN Ingenuity Pathway Analysis version 81348237 | Krämer et al. [182] | https://digitalinsights.qiagen.com/products-overview/discovery-insights-portfolio/analysis-and-visualization/qiagen-ipa/ RRID: SCR_008653 |
| Nextflow version 21.10.6 | Tommaso et al. [183] | https://github.com/nextflow-io/nextflow RRID: SCR_024135 |
| nfcore/chipseq version 1.2.2 | Ewels et al. [184] | https://nf-co.re/chipseq/1.2.2 https://zenodo.org/record/7139814#.Y4lJDXbP1aQ RRID: N/A |
| nfcore/atacseq version 1.2.1 | Ewels et al. [184] | https://nf-co.re/atacseq/1.2.1 https://zenodo.org/record/7384115#.Y4lJv3bP1aQ RRID: N/A |
| Trim Galore! Version 0.6.6 | The Babraham Institute | http://www.bioinformatics.babraham.ac.uk/projects/trim_galore/ RRID: SCR_011847 |
| hisat2 version 2.2.1 | Kim et al. [185] | http://ccb.jhu.edu/software/hisat2/index.shtml RRID: SCR_015530 |
| Samtools version 1.9 | Danecek et al. [186] | https://github.com/samtools/samtools RRID: SCR_002105 |
| Subread version 2.0.1 | Liao et al. [187] | https://subread.sourceforge.net/ RRID: SCR_009803 |
| BEDTools version 2.30.0 | Quinlan et al. [188] | https://github.com/arq5x/bedtools2 RRID: SCR_006646 |
| HOMER version 4.11 | Heinz et al. [96] | http://homer.ucsd.edu/homer/ RRID: SCR_010881 |
| DoRothEA version 1.8.0 | Garcia-Alonso et al. [90] | https://saezlab.github.io/dorothea/ RRID: N/A |
| clusterProfiler version 4.4.4 | Wu et al. [189] | https://bioconductor.org/packages/release/bioc/html/clusterProfiler.html RRID: SCR_016884 |
| DESeq2 version 1.36.0 | Love et al. [190] | https://bioconductor.org/packages/release/bioc/html/DESeq2.html RRID: SCR_015687 |
| ChIPseeker version | Yu et al. | https://bioconductor.org/packages/release/bioc/ht |

| | | |
|---|---|---|
| 1.32.1 | [191] | ml/ChIPseeker.html<br>RRID: SCR_021322 |
| rrcov version 1.5.2 | Hubert et al. [192] | https://cran.r-project.org/package=rrcov<br>RRID: N/A |
| ChIP-Atlas | Oki et al. [114]<br>Zou et al. [115] | http://chip-atlas.org/<br>RRID: SCR_015511 |
| The Signaling Pathways Project | Ochsner et al. [119] | https://signalingpathways.org<br>RRID: SCR_018412 |

# ACKNOWLEDGEMENTS

First, I would like to thank my supervisor, Dr. Mariko Okada, for accepting me into the lab and giving me this valuable opportunity. Special thanks to Dr. Keita Iida, who contributed to the bifurcation analyses. Without his assistance, I could not have completed this work.

I would also like to thank all the current and former members of the Laboratory of Cell Systems at Osaka University for their helpful advice and support during this study. I am grateful to Mr. Johannes Nicolaus Wibisana (Okinawa Institute of Science and Technology) for his guidance on bioinformatics analysis, and to Dr. Hiroaki Imoto (University College Dublin) and Mr. Ken Murakami (Osaka University) for their assistance with the mathematical analysis.

I especially thank Dr. Kohei Miyazono (The University of Tokyo) and Dr. Sho Tabata (National Cancer Center Japan) for their insightful discussions regarding this study.

I would like to thank Dr. Kenji Mizuguchi and Dr. Tohru Ishitani for critically reviewing this dissertation and for their valuable feedback.

Lastly, for their understanding and support of my research activities, I would like to thank my family, especially my wife and our sons.

# REFERENCES


1. Niccoli, T., and Partridge, L. (2012). Ageing as a risk factor for disease. **Curr. Biol.** *22*, R741-52. https://doi.org/10.1016/j.cub.2012.07.024.

2. Albert, A., Knoll, M.A., Conti, J.A., and Zbar, R.I.S. (2019). Non-Melanoma Skin Cancers in the Older Patient. **Curr. Oncol. Rep.** *21*, 79. https://doi.org/10.1007/s11912-019-0828-9.

3. Rabheru, K., Byles, J.E., and Kalache, A. (2022). How "old age" was withdrawn as a diagnosis from ICD-11. **lancet. Heal. Longev.** *3*, e457–e459. https://doi.org/10.1016/S2666-7568(22)00102-7.

4. Ritchie, H., Rodés-Guirao, L., Mathieu, E., Gerber, M., Ortiz-Ospina, E., Hasell, J., and Roser, M. (2023). Population Growth. **Our World Data**. https://ourworldindata.org/population-growth.

5. Ministry of Health, L. and W. (2023). Health Japan 21: the third phase [Japanese]. https://www.mhlw.go.jp/content/001102474.pdf.

6. Nishi, N., Ikeda, N., Sugiyama, T., Kurotani, K., and Miyachi, M. (2020). Simulating the Impact of Long-Term Care Prevention Among Older Japanese People on Healthcare Costs From 2020 to 2040 Using System Dynamics Modeling. **Front. Public Heal.** *8*, 1–7. https://doi.org/10.3389/fpubh.2020.592471.

7. Wong, Q.Y.A., and Chew, F.T. (2021). Defining skin aging and its risk factors: a systematic review and meta-analysis. **Sci. Rep.** *11*, 1–13. https://doi.org/10.1038/s41598-021-01573-z.

8. de Bengy, A.F., Lamartine, J., Sigaudo-Roussel, D., and Fromy, B. (2022). Newborn and elderly skin: two fragile skins at higher risk of pressure injury. **Biol. Rev.** *97*, 874–895. https://doi.org/10.1111/brv.12827.

9. Jaeger, B., Wagemans, F.M.A., Evans, A.M., and van Beest, I. (2018). Effects of Facial Skin Smoothness and Blemishes on Trait Impressions. **Perception** *47*, 608–625. https://doi.org/10.1177/0301006618767258.

10. Ikeda, H., Saheki, Y., Sakano, Y., Wada, A., Ando, H., and Tagai, K. (2021). Facial radiance influences facial attractiveness and affective impressions of faces. **Int. J. Cosmet. Sci.** *43*, 144–157. https://doi.org/10.1111/ics.12673.

11. Fink, B., Grammer, K., and Matts, P.J. (2006). Visible skin color distribution plays a role

in the perception of age, attractiveness, and health in female faces. **Evol. Hum. Behav.** *27*, 433–442. https://doi.org/10.1016/j.evolhumbehav.2006.08.007.

12. Tan, K.W., Tiddeman, B., and Stephen, I.D. (2018). Skin texture and colour predict perceived health in Asian faces. **Evol. Hum. Behav.** *39*, 320–335. https://doi.org/10.1016/j.evolhumbehav.2018.02.003.

13. Gupta, M.A., and Gilchrest, B.A. (2005). Psychosocial aspects of aging skin. **Dermatol. Clin.** *23*, 643–648. https://doi.org/10.1016/j.det.2005.05.012.

14. Mosteller, R.D. (1987). Simplified calculation of body-surface area. **N. Engl. J. Med**. 317, 1098. https://doi.org/10.1056/NEJM198710223171717.

15. Arda, O., Göksügür, N., and Tüzün, Y. (2014). Basic histological structure and functions of facial skin. **Clin. Dermatol.** *32*, 3–13. https://doi.org/10.1016/j.clindermatol.2013.05.021.

16. Fore, J. (2006). A review of skin and the effects of aging on skin structure and function. **Ostomy. Wound. Manage.** *52*, 24–27.

17. Fenske, N.A., and Lober, C.W. (1986). Structural and functional changes of normal aging skin. **J. Am. Acad. Dermatol.** *15*, 571–585. https://doi.org/10.1016/s0190-9622(86)70208-9.

18. Brun, C., Jean-Louis, F., Oddos, T., Bagot, M., Bensussan, A., and Michel, L. (2016). Phenotypic and functional changes in dermal primary fibroblasts isolated from intrinsically aged human skin. **Exp. Dermatol.** *25*, 113–119. https://doi.org/10.1111/exd.12874.

19. Montagna, W., and Carlisle, K. (1990). Structural changes in ageing skin. **Br. J. Dermatol.** *122 Suppl*, 61–70. https://doi.org/10.1111/j.1365-2133.1990.tb16127.x.

20. Quan, T. (2023). Molecular insights of human skin epidermal and dermal aging. **J. Dermatol. Sci.** *112*, 48–53. https://doi.org/10.1016/j.jdermsci.2023.08.006.

21. Ashcroft, G.S., Mills, S.J., and Ashworth, J.J. (2002). Ageing and wound healing. **Biogerontology** *3*, 337–345. https://doi.org/10.1023/a:1021399228395.

22. Thomas, D.R. (2001). Age-related changes in wound healing. **Drugs Aging** *18*, 607–620. https://doi.org/10.2165/00002512-200118080-00005.

23. Krutmann, J., Bouloc, A., Sore, G., Bernard, B.A., and Passeron, T. (2017). The skin aging exposome. **J. Dermatol. Sci.** *85*, 152–161.

https://doi.org/10.1016/j.jdermsci.2016.09.015.

24. Costello, L., Dicolandrea, T., Tasseff, R., Isfort, R., Bascom, C., von Zglinicki, T., and Przyborski, S. (2022). Tissue engineering strategies to bioengineer the ageing skin phenotype in vitro. **Aging Cell** *21*, e13550. https://doi.org/10.1111/acel.13550.

25. Jin, S., Li, K., Zong, X., Eun, S., Morimoto, N., and Guo, S. (2023). Hallmarks of Skin Aging: Update. **Aging Dis.** *14*, 2167–2176. https://doi.org/10.14336/AD.2023.0321.

26. Shin, S.H., Lee, Y.H., Rho, N.K., and Park, K.Y. (2023). Skin aging from mechanisms to interventions: focusing on dermal aging. **Front. Physiol.** *14*, 1–10. https://doi.org/10.3389/fphys.2023.1195272.

27. Low, E., Alimohammadiha, G., Smith, L.A., Costello, L.F., Przyborski, S.A., von Zglinicki, T., and Miwa, S. (2021). How good is the evidence that cellular senescence causes skin ageing? **Ageing Res. Rev.** 71, 101456. https://doi.org/10.1016/j.arr.2021.101456.

28. López-Otín, C., Blasco, M.A., Partridge, L., Serrano, M., and Kroemer, G. (2023). Hallmarks of aging: An expanding universe. **Cell** *186*, 243–278. https://doi.org/10.1016/j.cell.2022.11.001.

29. Krishnamurthy, J., Torrice, C., Ramsey, M.R., Kovalev, G.I., Al-Regaiey, K., Su, L., and Sharpless, N.E. (2004). Ink4a/Arf expression is a biomarker of aging. **J. Clin. Invest.** *114*, 1299–1307. https://doi.org/10.1172/JCI22475.

30. Hayflick, L., and Moorhead, P.S. (1961). The serial cultivation of human diploid cell strains. **Exp. Cell Res.** *25*, 585–621. https://doi.org/10.1016/0014-4827(61)90192-6.

31. Bodnar, A.G., Ouellette, M., Frolkis, M., Holt, S.E., Chiu, C.P., Morin, G.B., Harley, C.B., Shay, J.W., Lichtsteiner, S., and Wright, W.E. (1998). Extension of life-span by introduction of telomerase into normal human cells. **Science** (80-. ). *279*, 349–352. https://doi.org/10.1126/science.279.5349.349.

32. Petrova, N. V., Velichko, A.K., Razin, S. V., and Kantidze, O.L. (2016). Small molecule compounds that induce cellular senescence. **Aging Cell** *15*, 999–1017. https://doi.org/10.1111/acel.12518.

33. Roger, L., Tomas, F., and Gire, V. (2021). Mechanisms and regulation of cellular senescence. **Int. J. Mol. Sci.** *22*, 1–42. https://doi.org/10.3390/ijms222313173.

34. Lee, Y.I., Choi, S., Roh, W.S., Lee, J.H., and Kim, T.G. (2021). Cellular senescence and

inflammaging in the skin microenvironment. **Int. J. Mol. Sci.** 22, 3849. https://doi.org/10.3390/ijms22083849.

35. Ho, C.Y., and Dreesen, O. (2021). Faces of cellular senescence in skin aging. **Mech. Ageing Dev.** *198*. https://doi.org/10.1016/j.mad.2021.111525.

36. Dreesen, O., Chojnowski, A., Ong, P.F., Zhao, T.Y., Common, J.E., Lunny, D., Lane, E.B., Lee, S.J., Vardy, L.A., Stewart, C.L., et al. (2013). Lamin B1 fluctuations have differential effects on cellular proliferation and senescence. **J. Cell Biol.** *200*, 605–617. https://doi.org/10.1083/jcb.201206121.

37. Wang, A.S., Ong, P.F., Chojnowski, A., Clavel, C., and Dreesen, O. (2017). Loss of lamin B1 is a biomarker to quantify cellular senescence in photoaged skin. **Sci. Rep.** *7*, 15678. https://doi.org/10.1038/s41598-017-15901-9.

38. Dimri, G.P., Lee, X., Basile, G., Acosta, M., Scott, G., Roskelley, C., Medrano, E.E., Linskens, M., Rubelj, I., and Pereira-Smith, O. (1995). A biomarker that identifies senescent human cells in culture and in aging skin in vivo. **Proc. Natl. Acad. Sci. U. S. A.** *92*, 9363–9367. https://doi.org/10.1073/pnas.92.20.9363.

39. Yamakoshi, K., Takahashi, A., Hirota, F., Nakayama, R., Ishimaru, N., Kubo, Y., Mann, D.J., Ohmura, M., Hirao, A., Saya, H., et al. (2009). Real-time in vivo imaging of p16Ink4a reveals cross talk with p53. **J. Cell Biol.** *186*, 393–407. https://doi.org/10.1083/jcb.200904105.

40. Omori, S., Wang, T.-W., Johmura, Y., Kanai, T., Nakano, Y., Kido, T., Susaki, E.A., Nakajima, T., Shichino, S., Ueha, S., et al. (2020). Generation of a p16 Reporter Mouse and Its Use to Characterize and Target p16(high) Cells In Vivo. **Cell Metab.** *32*, 814-828.e6. https://doi.org/10.1016/j.cmet.2020.09.006.

41. Baker, D.J., Wijshake, T., Tchkonia, T., Lebrasseur, N.K., Childs, B.G., Van De Sluis, B., Kirkland, J.L., and Van Deursen, J.M. (2011). Clearance of p16 Ink4a-positive senescent cells delays ageing-associated disorders. **Nature** *479*, 232–236. https://doi.org/10.1038/nature10600.

42. Baker, D.J., Childs, B.G., Durik, M., Wijers, M.E., Sieben, C.J., Zhong, J., A. Saltness, R., Jeganathan, K.B., Verzosa, G.C., Pezeshki, A., et al. (2016). Naturally occurring p16 Ink4a-positive cells shorten healthy lifespan. **Nature** *530*, 184–189. https://doi.org/10.1038/nature16932.

43. Wyles, S.P., Carruthers, J.D., Dashti, P., Yu, G., Yap, J.Q., Gingery, A., Tchkonia, T.,

and Kirkland, J. (2024). Cellular Senescence in Human Skin Aging: Leveraging Senotherapeutics. **Gerontology** *70*, 7–14. https://doi.org/10.1159/000534756.

44. Hickson, L.J., Langhi Prata, L.G.P., Bobart, S.A., Evans, T.K., Giorgadze, N., Hashmi, S.K., Herrmann, S.M., Jensen, M.D., Jia, Q., Jordan, K.L., et al. (2019). Senolytics decrease senescent cells in humans: Preliminary report from a clinical trial of Dasatinib plus Quercetin in individuals with diabetic kidney disease. **EBioMedicine** *47*, 446–456. https://doi.org/10.1016/j.ebiom.2019.08.069.

45. Kim, H., Jang, J., Song, M.J., Kim, G., Park, C.-H., Lee, D.H., Lee, S.-H., and Chung, J.H. (2022). Attenuation of intrinsic ageing of the skin via elimination of senescent dermal fibroblasts with senolytic drugs. **J. Eur. Acad. Dermatol. Venereol.** *36*, 1125–1135. https://doi.org/10.1111/jdv.18051.

46. Waaijer, M.E.C., Gunn, D.A., Adams, P.D., Pawlikowski, J.S., Griffiths, C.E.M., Van Heemst, D., Slagboom, P.E., Westendorp, R.G.J., and Maier, A.B. (2016). P16INK4a Positive Cells in Human Skin Are Indicative of Local Elastic Fiber Morphology, Facial Wrinkling, and Perceived Age. **Journals Gerontol. - Ser. A Biol. Sci. Med. Sci.** *71*, 1022–1028. https://doi.org/10.1093/gerona/glv114.

47. Ogata, Y., Yamada, T., Hasegawa, S., Sugiura, K., and Akamatsu, H. (2023). Changes of senescent cell accumulation and removal in skin tissue with ageing. **Exp. Dermatol**. 32, 1159–1161. https://doi.org/10.1111/exd.14818 https://doi.org/10.1111/exd.14818.

48. Jevtić, M., Löwa, A., Nováčková, A., Kováčik, A., Kaessmeyer, S., Erdmann, G., Vávrová, K., and Hedtrich, S. (2020). Impact of intercellular crosstalk between epidermal keratinocytes and dermal fibroblasts on skin homeostasis. **Biochim. Biophys. Acta - Mol. Cell Res.** *1867*, 118722. https://doi.org/10.1016/j.bbamcr.2020.118722.

49. Janson, D., Rietveld, M., Willemze, R., and El Ghalbzouri, A. (2013). Effects of serially passaged fibroblasts on dermal and epidermal morphogenesis in human skin equivalents. **Biogerontology** *14*, 131–140. https://doi.org/10.1007/s10522-013-9416-9.

50. Weinmüllner, R., Zbiral, B., Becirovic, A., Stelzer, E.M., Nagelreiter, F., Schosserer, M., Lämmermann, I., Liendl, L., Lang, M., Terlecki-Zaniewicz, L., et al. (2020). Organotypic human skin culture models constructed with senescent fibroblasts show hallmarks of skin aging. **npj Aging Mech. Dis.** *6*. https://doi.org/10.1038/s41514-020-0042-x.

51. Van Deursen, J.M. (2014). The role of senescent cells in ageing. **Nature** *509*, 439–446. https://doi.org/10.1038/nature13193.

52. Kumari, R., and Jat, P. (2021). Mechanisms of Cellular Senescence: Cell Cycle Arrest and Senescence Associated Secretory Phenotype. **Front. Cell Dev. Biol.** *9*, 1–24. https://doi.org/10.3389/fcell.2021.645593.

53. García-García, V.A., Alameda, J.P., Page, A., and Casanova, M.L. (2021). Role of nf-κb in ageing and age-related diseases: Lessons from genetically modified mouse models. **Cells** *10*, 1–29. https://doi.org/10.3390/cells10081906.

54. Jung, M., Jin, S.G., Zhang, X., Xiong, W., Gogoshin, G., Rodin, A.S., and Pfeifer, G.P. (2015). Longitudinal epigenetic and gene expression profiles analyzed by three-component analysis reveal down-regulation of genes involved in protein translation in human aging. **Nucleic Acids Res.** *43*, 1–14. https://doi.org/10.1093/nar/gkv473.

55. Köhler, F., Bormann, F., Raddatz, G., Gutekunst, J., Corless, S., Musch, T., Lonsdorf, A.S., Erhardt, S., Lyko, F., and Rodríguez-Paredes, M. (2020). Epigenetic deregulation of lamina-associated domains in Hutchinson-Gilford progeria syndrome. **Genome Med.** *12*. https://doi.org/10.1186/s13073-020-00749-y.

56. Solé-Boldo, L., Raddatz, G., Schütz, S., Mallm, J.P., Rippe, K., Lonsdorf, A.S., Rodríguez-Paredes, M., and Lyko, F. (2020). Single-cell transcriptomes of the human skin reveal age-related loss of fibroblast priming. **Commun. Biol.** *3*, 1–12. https://doi.org/10.1038/s42003-020-0922-4.

57. Zou, Z., Long, X., Zhao, Q., Zheng, Y., Song, M., Ma, S., Jing, Y., Wang, S., He, Y., Esteban, C.R., et al. (2021). A Single-Cell Transcriptomic Atlas of Human Skin Aging. **Dev. Cell** *56*, 383-397.e8. https://doi.org/10.1016/j.devcel.2020.11.002.

58. Tanaka, R.J., and Ono, M. (2013). Skin disease modeling from a mathematical perspective. **J. Invest. Dermatol.** *133*, 1472–1478. https://doi.org/10.1038/jid.2013.69.

59. Paysan, P. (2010). Statistical modeling of facial aging based on 3D scans. Doctoral Thesis, University of Basel, Faculty of Science. https://doi.org/10.5451/unibas-005318344.

60. Pitanguy, I., Pamplona, D., Weber, H.I., Leta, F., Salgado, F., and Radwanski, H.N. (1998). Numerical modeling of facial aging. **Plast. Reconstr. Surg.** *102*, 200–204. https://doi.org/10.1097/00006534-199807000-00033.

61. van Logtestijn, M.D.A., Domínguez-Hüttinger, E., Stamatas, G.N., and Tanaka, R.J. (2015). Resistance to water diffusion in the stratum corneum is depth-dependent. **PLoS One** *10*, e0117292. https://doi.org/10.1371/journal.pone.0117292.

62. Narisu, N., Rothwell, R., Vrtačnik, P., Rodríguez, S., Didion, J., Zöllner, S., Erdos, M.R., Collins, F.S., and Eriksson, M. (2019). Analysis of somatic mutations identifies signs of selection during in vitro aging of primary dermal fibroblasts. **Aging Cell** *18*, e13010. https://doi.org/10.1111/acel.13010.

63. Galvis, D., Walsh, D., Harries, L.W., Latorre, E., and Rankin, J. (2019). A dynamical systems model for the measurement of cellular senescence. **J. R. Soc. Interface** *16*, 20190311. https://doi.org/10.1098/rsif.2019.0311.

64. Eberly, L.E. (2007). Correlation and simple linear regression. **Methods Mol. Biol.** *404*, 143–164. https://doi.org/10.1007/978-1-59745-530-5_8.

65. Haga, M., and Okada, M. (2022). Systems approaches to investigate the role of NF-κB signaling in aging. **Biochem. J.** *479*, 161–183. https://doi.org/10.1042/BCJ20210547.

66. Domínguez-Hüttinger, E., Christodoulides, P., Miyauchi, K., Irvine, A.D., Okada-Hatakeyama, M., Kubo, M., and Tanaka, R.J. (2017). Mathematical modeling of atopic dermatitis reveals "double-switch" mechanisms underlying 4 common disease phenotypes. **J. Allergy Clin. Immunol.** *139*, 1861-1872.e7. https://doi.org/10.1016/j.jaci.2016.10.026.

67. Fey, D., Halasz, M., Dreidax, D., Kennedy, S.P., Hastings, J.F., Rauch, N., Munoz, A.G., Pilkington, R., Fischer, M., Westermann, F., et al. (2015). Signaling pathway models as biomarkers: Patient-specific simulations of JNK activity predict the survival of neuroblastoma patients. **Sci. Signal.** *8*, 1–16. https://doi.org/10.1126/scisignal.aab0990.

68. Imoto, H., Yamashiro, S., and Okada, M. (2022). A text-based computational framework for patient -specific modeling for classification of cancers. **iScience** *25*, 103944. https://doi.org/10.1016/j.isci.2022.103944.

69. Union, P. (2009). Regulation (EC) no 1223/2009 of the European Parliament and of the council. **Off. J. Eur. Union** 59, L342.

70. Westont, A.D., and Hood, L. (2004). Systems Biology, Proteomics, and the Future of Health Care: Toward Predictive, Preventative, and Personalized Medicine. **J. Proteome Res.** *3*, 179–196. https://doi.org/10.1021/pr0499693.

71. Gunawardena, J. (2014). Models in biology: 'accurate descriptions of our pathetic thinking.' **BMC Biol.** *12*, 29. https://doi.org/10.1186/1741-7007-12-29.

72. Kestler, H.A., Wawra, C., Kracher, B., and Kühl, M. (2008). Network modeling of

signal transduction: Establishing the global view. **BioEssays** *30*, 1110–1125. https://doi.org/10.1002/bies.20834.

73. Yang, B., and Chen, Y. (2020). Overview of Gene Regulatory Network Inference Based on Differential Equation Models. **Curr. Protein Pept. Sci.** *21*, 1054–1059. https://doi.org/10.2174/1389203721666200213103350.

74. Lebl, J. (2013). Ordinary Differential Equations. In Computational Toxicology: Volume II, B. Reisfeld and A. N. Mayeno, eds. **Humana Press.** pp. 475–498. https://doi.org/10.1007/978-1-62703-059-5_20.

75. Chen, W.W., Niepel, M., and Sorger, P.K. (2010). Classic and contemporary approaches to modeling biochemical reactions. **Genes Dev.** *24*, 1861–1875. https://doi.org/10.1101/gad.1945410.

76. Haga, M., Iida, K., and Okada, M. (2024). Positive and negative feedback regulation of the TGF-β1 explains two equilibrium states in skin aging. **iScience** *27*, 109708. https://doi.org/10.1016/j.isci.2024.109708.

77. Marthandan, S., Baumgart, M., Priebe, S., Groth, M., Schaer, J., Kaether, C., Guthke, R., Cellerino, A., Platzer, M., Diekmann, S., et al. (2016). Conserved senescence associated genes and pathways in primary human fibroblasts detected by RNA-seq. **PLoS One** *11*, 1–31. https://doi.org/10.1371/journal.pone.0154531.

78. Fleischer, J.G., Schulte, R., Tsai, H.H., Tyagi, S., Ibarra, A., Shokhirev, M.N., Huang, L., Hetzer, M.W., and Navlakha, S. (2018). Predicting age from the transcriptome of human dermal fibroblasts. **Genome Biol.** *19*, 1–8. https://doi.org/10.1186/s13059-018-1599-6.

79. Murphy-Ullrich, J.E., and Suto, M.J. (2018). Thrombospondin-1 regulation of latent TGF-β activation: A therapeutic target for fibrotic disease. **Matrix Biol.** *68–69*, 28–43. https://doi.org/10.1016/j.matbio.2017.12.009.

80. Hildebrand, A., Romaris, M., Rasmussen, M., Heinegard, D., Twardzik, D.R., Border, W.A., and Ruoslahti, E. (1994). Interaction of the small interstitial proteoglycans biglycan, decorin and fibromodulin with transforming growth factor β. **Biochem. J.** *302*, 527–534. https://doi.org/10.1042/bj3020527.

81. Embree, M.C., Kilts, T.M., Ono, M., Inkson, C.A., Syed-Picard, F., Karsdal, M.A., Oldberg, Å., Bi, Y., and Young, M.F. (2010). Biglycan and fibromodulin have essential roles in regulating chondrogenesis and extracellular matrix turnover in

temporomandibular joint osteoarthritis. **Am. J. Pathol.** *176*, 812–826. https://doi.org/10.2353/ajpath.2010.090450.

82. Pang, X., Dong, N., and Zheng, Z. (2020). Small leucine-rich proteoglycans in skin wound healing. **Front. Pharmacol.** *10*, 1–18. https://doi.org/10.3389/fphar.2019.01649.

83. Team BC, M.B. (2019). TxDb.Hsapiens.UCSC.hg38.knownGene: Annotation package for TxDb object(s). R Packag. version 3.4.6. https://doi.org/10.18129/B9.bioc.TxDb.Hsapiens.UCSC.hg38.knownGene.

84. Henrot, P., Laurent, P., Levionnois, E., Leleu, D., Pain, C., Truchetet, M.E., and Cario, M. (2020). A Method for Isolating and Culturing Skin Cells: Application to Endothelial Cells, Fibroblasts, Keratinocytes, and Melanocytes From Punch Biopsies in Systemic Sclerosis Skin. **Front. Immunol.** *11*, 1–12. https://doi.org/10.3389/fimmu.2020.566607.

85. Shahrezaei, V., Ollivier, J.F., and Swain, P.S. (2008). Colored extrinsic fluctuations and stochastic gene expression. **Mol. Syst. Biol.** *4*, 1–9. https://doi.org/10.1038/msb.2008.31.

86. Lucarelli, P., Schilling, M., Kreutz, C., Vlasov, A., Boehm, M.E., Iwamoto, N., Steiert, B., Lattermann, S., Wäsch, M., Stepath, M., et al. (2018). Resolving the Combinatorial Complexity of Smad Protein Complex Formation and Its Link to Gene Expression. **Cell Syst.** *6*, 75-89.e11. https://doi.org/10.1016/j.cels.2017.11.010.

87. Storn, R., and Price, K. (1997). Differential Evolution – A Simple and Efficient Heuristic for global Optimization over Continuous Spaces. **J. Glob. Optim.** *11*, 341–359. https://doi.org/10.1023/A:1008202821328.

88. Imoto, H., Zhang, S., and Okada, M. (2020). A computational framework for prediction and analysis of cancer signaling dynamics from rna sequencing data—application to the erbb receptor signaling pathway. **Cancers (Basel).** *12*, 1–13. https://doi.org/10.3390/cancers12102878.

89. Deng, T., Yan, G., Song, X., Xie, L., Zhou, Y., Li, J., Hu, X., Li, Z., Hu, J., Zhang, Y., et al. (2018). Deubiquitylation and stabilization of p21 by USP11 is critical for cell-cycle progression and DNA damage responses. **Proc. Natl. Acad. Sci. U. S. A.** *115*, 4678–4683. https://doi.org/10.1073/pnas.1714938115.

90. Garcia-Alonso, L., Holland, C.H., Ibrahim, M.M., Turei, D., and Saez-Rodriguez, J. (2019). Benchmark and integration of resources for the estimation of human transcription factor activities. **Genome Res.** *29*, 1363–1375. https://doi.org/10.1101/gr.240663.118.

91. Wang, Y., Liu, L., Song, Y., Yu, X., and Deng, H. (2022). Unveiling E2F4, TEAD1 and AP-1 as regulatory transcription factors of the replicative senescence program by multi-omics analysis. **Protein Cell** *13*, 742–759. https://doi.org/10.1007/s13238-021-00894-z.

92. Jiao, H., Walczak, B.E., Lee, M.S., Lemieux, M.E., and Li, W.J. (2021). GATA6 regulates aging of human mesenchymal stem/stromal cells. **Stem Cells** *39*, 62–77. https://doi.org/10.1002/stem.3297.

93. Mijit, M., Caracciolo, V., Melillo, A., Amicarelli, F., and Giordano, A. (2020). Role of p53 in the regulation of cellular senescence. **Biomolecules** 10. https://doi.org/10.3390/biom10030420.

94. Qin, Q., Fan, J., Zheng, R., Wan, C., Mei, S., Wu, Q., Sun, H., Brown, M., Zhang, J., Meyer, C.A., et al. (2020). Lisa: inferring transcriptional regulators through integrative modeling of public chromatin accessibility and ChIP-seq data. **Genome Biol.** *21*. https://doi.org/10.1186/s13059-020-1934-6.

95. Shi, Y., and Massagué, J. (2003). Mechanisms of TGF-signaling from cell membrane to the nucleus, **Cell**, 113, 685-700. https://doi.org/10.1016/s0092-8674(03)00432-x.

96. Heinz, S., Benner, C., Spann, N., Bertolino, E., Lin, Y.C., Laslo, P., Cheng, J.X., Murre, C., Singh, H., and Glass, C.K. (2010). Simple Combinations of Lineage-Determining Transcription Factors Prime cis-Regulatory Elements Required for Macrophage and B Cell Identities. **Mol. Cell** *38*, 576–589. https://doi.org/10.1016/j.molcel.2010.05.004.

97. Kanehisa, M., and Goto, S. (2000). KEGG: kyoto encyclopedia of genes and genomes. **Nucleic Acids Res.** *28*, 27–30. https://doi.org/10.1093/nar/28.1.27.

98. Isenberg, J.S., and Roberts, D.D. (2020). Thrombospondin-1 in maladaptive aging responses: A concept whose time has come. **Am. J. Physiol. - Cell Physiol.** *318*, C45–C63. https://doi.org/10.1152/ajpcell.00089.2020.

99. Kalamajski, S., Bihan, D., Bonna, A., Rubin, K., and Farndale, R.W. (2016). Fibromodulin interacts with collagen cross-linking sites and activates lysyl oxidase. **J. Biol. Chem.** *291*, 7951–7960. https://doi.org/10.1074/jbc.M115.693408.

100. Gunin, A.G., and Golubtzova, N.N. (2019). Transforming Growth Factor-β (TGF-β) in Human Skin during Aging. **Adv. Gerontol.** *9*, 267–273. https://doi.org/10.1134/S2079057019030068.

101. Guo, F., Hutchenreuther, J., Carter, D.E., and Leask, A. (2013). TAK1 is required for dermal wound healing and homeostasis. **J. Invest. Dermatol.** *133*, 1646–1654.

https://doi.org/10.1038/jid.2013.28.

102. Zhang, Y., Feng, X.H., and Derynck, R. (1998). Smad3 and Smad4 cooperate with c-Jun/c-Fos to mediate TGF-beta-induced transcription. **Nature** *394*, 909–913. https://doi.org/10.1038/29814.

103. Liberati, N.T., Datto, M.B., Frederick, J.P., Shen, X., Wong, C., Rougier-Chapman, E.M., and Wang, X.F. (1999). Smads bind directly to the Jun family of AP-1 transcription factors. **Proc. Natl. Acad. Sci. U. S. A.** *96*, 4844–4849. https://doi.org/10.1073/pnas.96.9.4844.

104. Budi, E.H., Schaub, J.R., Decaris, M., Turner, S., and Derynck, R. (2021). TGF-β as a driver of fibrosis: physiological roles and therapeutic opportunities. **J. Pathol.** *254*, 358–373. https://doi.org/10.1002/path.5680.

105. Silverman, B.W. (1981). Using Kernel Density Estimates to Investigate Multimodality. **J. R. Stat. Soc. B** *43*, 97–99. http://www.jstor.org/stable/2985156.

106. Hu, H.-H., Chen, D.-Q., Wang, Y.-N., Feng, Y.-L., Cao, G., Vaziri, N.D., and Zhao, Y.-Y. (2018). New insights into TGF-β/Smad signaling in tissue fibrosis. **Chem. Biol. Interact.** *292*, 76–83. https://doi.org/10.1016/j.cbi.2018.07.008.

107. Sobel, K., Menyhart, K., Killer, N., Renault, B., Bauer, Y., Studer, R., Steiner, B., Bolli, M.H., Nayler, O., and Gatfield, J. (2013). Sphingosine 1-Phosphate (S1P) receptor agonists mediate pro-fibrotic responses in normal human lung fibroblasts via S1P2and S1P 3 receptors and smad-independent signaling. **J. Biol. Chem.** *288*, 14839–14851. https://doi.org/10.1074/jbc.M112.426726.

108. Flügel-Koch, C., Ohlmann, A., Fuchshofer, R., Welge-Lüssen, U., and Tamm, E.R. (2004). Thrombospondin-1 in the trabecular meshwork: Localization in normal and glaucomatous eyes, and induction by TGF-β1 and dexamethasone in vitro. **Exp. Eye Res.** *79*, 649–663. https://doi.org/10.1016/j.exer.2004.07.005.

109. Daubon, T., Léon, C., Clarke, K., Andrique, L., Salabert, L., Darbo, E., Pineau, R., Guérit, S., Maitre, M., Dedieu, S., et al. (2019). Deciphering the complex role of thrombospondin-1 in glioblastoma development. **Nat. Commun.** *10*. https://doi.org/10.1038/s41467-019-08480-y.

110. Coppe, J.P., Kauser, K., Campisi, J., and Beauséjour, C.M. (2006). Secretion of vascular endothelial growth factor by primary human fibroblasts at senescence. **J. Biol. Chem.** *281*, 29568–29574. https://doi.org/10.1074/jbc.M603307200.

111. Acosta, J.C., Banito, A., Wuestefeld, T., Georgilis, A., Janich, P., Morton, J.P., Athineos, D., Kang, T.W., Lasitschka, F., Andrulis, M., et al. (2013). A complex secretory program orchestrated by the inflammasome controls paracrine senescence. **Nat. Cell Biol.** *15*, 978–990. https://doi.org/10.1038/ncb2784.

112. Schoeberl, B., Pace, E.A., Fitzgerald, J.B., Harms, B.D., Xu, L., Nie, L., Linggi, B., Kalra, A., Paragas, V., Bukhalid, R., et al. (2009). Therapeutically targeting ErbB3: A key node in ligand-induced activation of the ErbB receptor-PI3K axis. **Sci. Signal.** *2*, 1–15. https://doi.org/10.1126/scisignal.2000352.

113. Noy, N. (2000). Retinoid-binding proteins: Mediators of retinoid action. **Biochem. J.** *348*, 481–495. https://doi.org/10.1042/0264-6021:3480481.

114. Oki, S., Ohta, T., Shioi, G., Hatanaka, H., Ogasawara, O., Okuda, Y., Kawaji, H., Nakaki, R., Sese, J., and Meno, C. (2018). Ch IP -Atlas: a data-mining suite powered by full integration of public Ch IP -seq data . **EMBO Rep.** *19*, 1–10. https://doi.org/10.15252/embr.201846255.

115. Zou, Z., Ohta, T., Miura, F., and Oki, S. (2022). ChIP-Atlas 2021 update: a data-mining suite for exploring epigenomic landscapes by fully integrating ChIP-seq, ATAC-seq and Bisulfite-seq data. **Nucleic Acids Res.** *50*, W175–W182. https://doi.org/10.1093/nar/gkac199.

116. Hosoda, K., Sato, M., and Yanai, K. (2015). Identification and Characterization of Human Genomic Binding Sites for Retinoic Acid Receptor/Retinoid X Receptor Heterodimers. **Adv. Biol. Chem.** *05*, 58–72. https://doi.org/10.4236/abc.2015.52006.

117. Lin, K.C., Park, H.W., and Guan, K.L. (2017). Regulation of the Hippo Pathway Transcription Factor TEAD. **Trends Biochem. Sci.** *42*, 862–872. https://doi.org/10.1016/j.tibs.2017.09.003.

118. Huh, H.D., Kim, D.H., Jeong, H.-S.S., and Park, H.W. (2019). Regulation of TEAD Transcription Factors in Cancer Biology. **Cells** *8*. https://doi.org/10.3390/cells8060600.

119. Ochsner, S.A., Abraham, D., Martin, K., Ding, W., McOwiti, A., Kankanamge, W., Wang, Z., Andreano, K., Hamilton, R.A., Chen, Y., et al. (2019). The Signaling Pathways Project, an integrated 'omics knowledgebase for mammalian cellular signaling pathways. **Sci. data** *6*, 252. https://doi.org/10.1038/s41597-019-0193-4.

120. Zhao, B., Ye, X., Yu, J., Li, L., Li, W., Li, S., Yu, J., Lin, J.D., Wang, C.-Y., Chinnaiyan, A.M., et al. (2008). TEAD mediates YAP-dependent gene induction and

growth control. **Genes Dev.** *22*, 1962–1971. https://doi.org/10.1101/gad.1664408.

121. Kaneda, A., Seike, T., Danjo, T., Nakajima, T., Otsubo, N., Yamaguchi, D., Tsuji, Y., Hamaguchi, K., Yasunaga, M., Nishiya, Y., et al. (2020). The novel potent TEAD inhibitor, K-975, inhibits YAP1/ TAZ-TEAD protein-protein interactions and exerts an anti-tumor effect on malignant pleural mesothelioma. **Am J Cancer Res**. 10(12):4399-4415.

122. Dupont, S., Morsut, L., Aragona, M., Enzo, E., Giulitti, S., Cordenonsi, M., Zanconato, F., Le Digabel, J., Forcato, M., Bicciato, S., et al. (2011). Role of YAP/TAZ in mechanotransduction. **Nature** *474*, 179–184. https://doi.org/10.1038/nature10137.

123. Lv, H., and Ai, D. (2022). Hippo/yes-associated protein signaling functions as a mechanotransducer in regulating vascular homeostasis. **J. Mol. Cell. Cardiol.** *162*, 158–165. https://doi.org/10.1016/j.yjmcc.2021.09.007.

124. Guimarães, C.F., Gasperini, L., Marques, A.P., and Reis, R.L. (2020). The stiffness of living tissues and its implications for tissue engineering. **Nat. Rev. Mater.** *5*, 351–370. https://doi.org/10.1038/s41578-019-0169-1.

125. Pailler-Mattei, C., Bec, S., and Zahouani, H. (2008). In vivo measurements of the elastic mechanical properties of human skin by indentation tests. **Med. Eng. Phys.** *30*, 599–606. https://doi.org/10.1016/j.medengphy.2007.06.011.

126. Moiseeva, V., Cisneros, A., Sica, V., Deryagin, O., Lai, Y., Jung, S., Andrés, E., An, J., Segalés, J., Ortet, L., et al. (2022). Senescence atlas reveals an aged-like inflamed niche that blunts muscle regeneration. **Nature** *613*. https://doi.org/10.1038/s41586-022-05535-x.

127. Noguchi, S., Saito, A., and Nagase, T. (2018). YAP/TAZ signaling as a molecular link between fibrosis and cancer. **Int. J. Mol. Sci.** *19*. https://doi.org/10.3390/ijms19113674.

128. Minagawa, S., Araya, J., Numata, T., Nojiri, S., Hara, H., Yumino, Y., Kawaishi, M., Odaka, M., Morikawa, T., Nishimura, S.L., et al. (2011). Accelerated epithelial cell senescence in IPF and the inhibitory role of SIRT6 in TGF-β-induced senescence of human bronchial epithelial cells. **Am. J. Physiol. - Lung Cell. Mol. Physiol.** *300*, 391–401. https://doi.org/10.1152/ajplung.00097.2010.

129. Datto, M.B., Li, Y., Panus, J.F., Howe, D.J., Xiong, Y., and Wang, X.F. (1995). Transforming growth factor β induces the cyclin-dependent kinase inhibitor p21 through a p53-independent mechanism. **Proc. Natl. Acad. Sci. U. S. A.** *92*, 5545–5549.

https://doi.org/10.1073/pnas.92.12.5545.

130. Chan, M., Yuan, H., Soifer, I., Maile, T.M., Wang, R.Y., Ireland, A., O'Brien, J., Goudeau, J., Chan, L., Vijay, T., et al. (2022). Novel Insights from a Multiomics Dissection of the Hayflick Limit. **Elife** *11*. https://doi.org/10.7554/ELIFE.70283.

131. Zhang, L. juan, Chen, S.X., Guerrero-Juarez, C.F., Li, F., Tong, Y., Liang, Y., Liggins, M., Chen, X., Chen, H., Li, M., et al. (2019). Age-Related Loss of Innate Immune Antimicrobial Function of Dermal Fat Is Mediated by Transforming Growth Factor Beta. **Immunity** *50*, 121-136.e5. https://doi.org/10.1016/j.immuni.2018.11.003.

132. Quan, T., and Fisher, G.J. (2015). Role of Age-Associated Alterations of the Dermal Extracellular Matrix Microenvironment in Human Skin Aging: A Mini-Review. **Gerontology** *61*, 427–434. https://doi.org/10.1159/000371708.

133. Quan, T., He, T., Shao, Y., Lin, L., Kang, S., Voorhees, J.J., and Fisher, G.J. (2006). Elevated cysteine-rich 61 mediates aberrant collagen homeostasis in chronologically aged and photoaged human skin. **Am. J. Pathol.** *169*, 482–490. https://doi.org/10.2353/ajpath.2006.060128.

134. Elster, D., and von Eyss, B. (2020). Hippo signaling in regeneration and aging. **Mech. Ageing Dev.** *189*, 111280. https://doi.org/10.1016/j.mad.2020.111280.

135. Yeung, Y.T., Guerrero-Castilla, A., Cano, M., Muñoz, M.F., Ayala, A., and Argüelles, S. (2019). Dysregulation of the Hippo pathway signaling in aging and cancer. **Pharmacol. Res.** *143*, 151–165. https://doi.org/10.1016/j.phrs.2019.03.018.

136. Sladitschek-Martens, H.L., Guarnieri, A., Brumana, G., Zanconato, F., Battilana, G., Xiccato, R.L., Panciera, T., Forcato, M., Bicciato, S., Guzzardo, V., et al. (2022). YAP/TAZ activity in stromal cells prevents ageing by controlling cGAS–STING. **Nature** *607*, 790–798. https://doi.org/10.1038/s41586-022-04924-6.

137. Anerillas, C., Mazan-Mamczarz, K., Herman, A.B., Munk, R., Lam, K.W.G., Calvo-Rubio, M., Garrido, A., Tsitsipatis, D., Martindale, J.L., Altés, G., et al. (2023). The YAP–TEAD complex promotes senescent cell survival by lowering endoplasmic reticulum stress. **Nat. Aging** *3*, 1237–1250. https://doi.org/10.1038/s43587-023-00480-4.

138. Wang, Y., Liu, L., Song, Y., Yu, X., and Deng, H. (2022). Unveiling E2F4, TEAD1 and AP-1 as regulatory transcription factors of the replicative senescence program by multi-omics analysis. **Protein Cell** *13*, 742–759. https://doi.org/10.1007/s13238-021-00894-z.

139. Liu, X., Li, H., Rajurkar, M., Li, Q., Cotton, J.L., Ou, J., Zhu, L.J., Goel, H.L., Mercurio, A.M., Park, J.S., et al. (2016). Tead and AP1 Coordinate Transcription and Motility. **Cell Rep.** *14*, 1169–1180. https://doi.org/10.1016/j.celrep.2015.12.104.

140. Zanconato, F., Forcato, M., Battilana, G., Azzolin, L., Quaranta, E., Bodega, B., Rosato, A., Bicciato, S., Cordenonsi, M., and Piccolo, S. (2015). Genome-wide association between YAP/TAZ/TEAD and AP-1 at enhancers drives oncogenic growth. **Nat. Cell Biol.** *17*, 1218–1227. https://doi.org/10.1038/ncb3216.

141. Qin, Z., Xia, W., Fisher, G.J., Voorhees, J.J., and Quan, T. (2018). YAP/TAZ regulates TGF-β/Smad3 signaling by induction of Smad7 via AP-1 in human skin dermal fibroblasts. **Cell Commun. Signal.** *16*, 18. https://doi.org/10.1186/s12964-018-0232-3.

142. Xie, Q., Chen, J., Feng, H., Peng, S., Adams, U., Bai, Y., Huang, L., Li, J., Huang, J., Meng, S., et al. (2013). YAP/TEAD-mediated transcription controls cellular senescence. **Cancer Res.** *73*, 3615–3624. https://doi.org/10.1158/0008-5472.CAN-12-3793.

143. Thomas, C., Karagounis, I. V., Srivastava, R.K., Vrettos, N., Nikolos, F., Francois, N., Huang, M., Gong, S., Long, Q., Kumar, S., et al. (2021). Estrogen receptor b-mediated inhibition of actin-based cell migration suppresses metastasis of inflammatory breast cancer. **Cancer Res.** *81*, 2399–2414. https://doi.org/10.1158/0008-5472.CAN-20-2743.

144. Mazur, E.C., Vasquez, Y.M., Li, X., Kommagani, R., Jiang, L., Chen, R., Lanz, R.B., Kovanci, E., Gibbons, W.E., and DeMayo, F.J. (2015). Progesterone receptor transcriptome and cistrome in decidualized human endometrial stromal cells. **Endocrinology** *156*, 2239–2253. https://doi.org/10.1210/en.2014-1566.

145. Sárvári, M., Kalló, I., Hrabovszky, E., Solymosi, N., Tóth, K., Likó, I., Molnár, B., Tihanyi, K., and Liposits, Z. (2010). Estradiol replacement alters expression of genes related to neurotransmission and immune surveillance in the frontal cortex of middle-aged, ovariectomized rats. **Endocrinology** *151*, 3847–3862. https://doi.org/10.1210/en.2010-0375.

146. Ly, D.H., Lockhart, D.J., Lerner, R.A., and Schultz, P.G. (2000). Mitotic Misregulation and Human Aging. **Science.** *287(5462)*, 2486–2492. https://doi.org/10.1126/science.287.5462.2486.

147. Waldera Lupa, D.M., Kalfalah, F., Safferling, K., Boukamp, P., Poschmann, G., Volpi, E., Götz-Rösch, C., Bernerd, F., Haag, L., Huebenthal, U., et al. (2015). Characterization of Skin Aging-Associated Secreted Proteins (SAASP) Produced by Dermal Fibroblasts Isolated from Intrinsically Aged Human Skin. **J. Invest. Dermatol.** *135*, 1954–1968.

https://doi.org/10.1038/jid.2015.120.

148. Meijles, D.N., Sahoo, S., Al Ghouleh, I., Amaral, J.H., Bienes-Martinez, R., Knupp, H.E., Attaran, S., Sembrat, J.C., Nouraie, S.M., Rojas, M.M., et al. (2017). The matricellular protein TSP1 promotes human and mouse endothelial cell senescence through CD47 and Nox1. **Sci. Signal.** *10*. https://doi.org/10.1126/scisignal.aaj1784.

149. Zhao, W., Shen, B., Cheng, Q., Zhou, Y., and Chen, K. (2023). Roles of TSP1-CD47 signaling pathway in senescence of endothelial cells: cell cycle, inflammation and metabolism. **Mol. Biol. Rep.** *50*, 4579–4585. https://doi.org/10.1007/s11033-023-08357-w.

150. McCabe, M.C., Hill, R.C., Calderone, K., Cui, Y., Yan, Y., Quan, T., Fisher, G.J., and Hansen, K.C. (2020). Alterations in extracellular matrix composition during aging and photoaging of the skin. **Matrix Biol. Plus** *8*, 100041. https://doi.org/10.1016/j.mbplus.2020.100041.

151. Takemon, Y., Chick, J.M., Gyuricza, I.G., Skelly, D.A., Devuyst, O., Gygi, S.P., Churchill, G.A., and Korstanje, R. (2021). Proteomic and transcriptomic profiling reveal different aspects of aging in the kidney. **Elife** *10*. https://doi.org/10.7554/eLife.62585.

152. Kim, S.A., Um, S.J., Kang, J.H., and Hong, K.J. (2001). Expression of thrombospondin-1 in human hepatocarcinoma cell lines and its regulation by transcription factor Jun/AP-1. **Mol. Cell. Biochem.** *216*, 21–29. https://doi.org/10.1023/A:1011022822077.

153. Xu, L., Xu, L., Xu, L., Zhang, Y., Chen, J., and Xu, Y. (2020). Thrombospondin-1: A Key Protein That Induces Fibrosis in Diabetic Complications. **J. Diabetes Res.** *2020*. https://doi.org/10.1155/2020/8043135.

154. Shen, J., Cao, B., Wang, Y., Ma, C., Zeng, Z., Liu, L., Li, X., Tao, D., Gong, J., and Xie, D. (2018). Hippo component YAP promotes focal adhesion and tumour aggressiveness via transcriptionally activating THBS1/FAK signalling in breast cancer. **J. Exp. Clin. Cancer Res.** *37*. https://doi.org/10.1186/s13046-018-0850-z.

155. Khan, F.U., Owusu-Tieku, N.Y.G., Dai, X., Liu, K., Wu, Y., Tsai, H.I., Chen, H., Sun, C., and Huang, L. (2019). Wnt/β-catenin pathway-regulated fibromodulin expression is crucial for breast cancer metastasis and inhibited by aspirin. **Front. Pharmacol.** *10*, 1–17. https://doi.org/10.3389/fphar.2019.01308.

156. An, W., Zhu, J. wei, Jiang, F., Jiang, H., Zhao, J. long, Liu, M. yun, Li, G. xiang, Shi, X. gang, Sun, C., and Li, Z. shen (2020). Fibromodulin is upregulated by oxidative stress

through the MAPK/AP-1 pathway to promote pancreatic stellate cell activation. **Pancreatology** *20*, 278–287. https://doi.org/10.1016/j.pan.2019.09.011.

157. Syaidah, R., Tsukada, T., Azuma, M., Horiguchi, K., Fujiwara, K., Kikuchi, M., and Yashiro, T. (2016). Fibromodulin expression in folliculostellate cells and pericytes is promoted by TGFβ signaling in rat anterior pituitary gland. **Acta Histochem. Cytochem.** *49*, 171–179. https://doi.org/10.1267/ahc.16021.

158. Li, H., Venkatraman, L., Narmada, B.C., White, J.K., Yu, H., and Tucker-Kellogg, L. (2017). Computational analysis reveals the coupling between bistability and the sign of a feedback loop in a TGF-β1 activation model. **BMC Syst. Biol.** *11*. https://doi.org/10.1186/s12918-017-0508-z.

159. Pybus, H.J., O'dea, R.D., and Brook, B.S. (2023). A dynamical model of TGF-β activation in asthmatic airways. **Math. Med. Biol. A J. IMA**, dqad004. https://doi.org/10.1093/imammb/dqad004.

160. Zi, Z., Feng, Z., Chapnick, D.A., Dahl, M., Deng, D., Klipp, E., Moustakas, A., and Liu, X. (2011). Quantitative analysis of transient and sustained transforming growth factor-β signaling dynamics. **Mol. Syst. Biol.** *7*, 1–12. https://doi.org/10.1038/msb.2011.22.

161. Khatibi, S., Zhu, H.J., Wagner, J., Tan, C.W., Manton, J.H., and Burgess, A.W. (2017). Mathematical model of TGF-βsignalling: Feedback coupling is consistent with signal switching. **BMC Syst. Biol.** *11*, 1–15. https://doi.org/10.1186/s12918-017-0421-5.

162. Griffiths, T.W., Watson, R.E.B., and Langton, A.K. (2023). Skin ageing and topical rejuvenation strategies. **Br. J. Dermatol.** *189*, I17–I23. https://doi.org/10.1093/bjd/ljad282.

163. Griffiths, C., Russman, A.N., Majmudar, G., Singer, R.S., Hamilton, T.A., and Voorhees, J.J. (1993). Restoration of Collagen Formation in Photodamaged Human Skin by Tretinoin (Retinoic Acid). **N. Engl. J. Med.** *329*, 530–535. https://doi.org/10.1056/NEJM199308193290803.

164. Masgrau-Peya, E., Salomon, D., Saurat, J.-H., and Meda, P. (1997). In Vivo Modulation of Connexins 43 and 26 of Human Epidermis by Topical Retinoic Acid Treatment. **J Histochem Cytochem**. *45(9),*1207-1215. https://doi.org/10.1177/002215549704500904.

165. Watson, R.E.B., Ratnayaka, J.A., Brooke, R.C.C., Yee-Sit-Yu, S., Ancian, P., and Griffiths, C.E.M. (2004). Retinoic acid receptor α expression and cutaneous ageing. **Mech. Ageing Dev.** *125*, 465–473. https://doi.org/10.1016/j.mad.2004.03.008.

166. Bauer, E.A., Seltzer, J.L., and Eisen, A.Z. (1983). Retinoic acid inhibition of collagenase and gelatinase expression in human skin fibroblast cultures. Evidence for a dual mechanism. **J. Invest. Dermatol.** *81*, 162–169. https://doi.org/10.1111/1523-1747.ep12543590.

167. Fisher, G.J., and Voorhees, J.J. (1996). Molecular mechanisms of retinoid actions in skin. **FASEB J.** *10*, 1002–1013. https://doi.org/10.1096/fasebj.10.9.8801161.

168. Fisher, G.J., Datta, S.C., Talwar, H.S., Wang, Z.Q., Varani, J., Kang, S., and Voorhees, J.J. (1996). Molecular basis of sun-induced premature skin ageing and retinoid antagonism. **Nature** *379*, 335–339. https://doi.org/10.1038/379335a0.

169. Fisher, G.J., Talwar, H.S., Lin, J., Lin, P., McPhillips, F., Wang, Z.Q., Li, X., Wan, Y., Kang, S., and Voorhees, J.J. (1998). Retinoic acid inhibits induction of c-Jun protein by ultraviolet radiation that occurs subsequent to activation of mitogen-activated protein kinase pathways in human skin in vivo. **J. Clin. Invest.** *101*, 1432–1440. https://doi.org/10.1172/JCI2153.

170. Xiao, R., Yoshida, N., Higashi, Y., Lu, Q.J., Fukushige, T., Kanzaki, T., and Kanekura, T. (2011). Retinoic acids exhibit anti-fibrotic activity through the inhibition of 5-lipoxygenase expression in scleroderma fibroblasts. **J. Dermatol.** *38*, 345–353. https://doi.org/10.1111/j.1346-8138.2010.00993.x.

171. Liu, Y., Kimura, K., Orita, T., Teranishi, S., Suzuki, K., and Sonoda, K.H. (2014). Inhibition by all-trans-retinoic acid of transforming growth factor-β-induced collagen gel contraction mediated by human tenon fibroblasts. **Investig. Ophthalmol. Vis. Sci.** *55*, 4199–4205. https://doi.org/10.1167/iovs.13-13572.

172. Xu, Q., and Kopp, J.B. (2012). Retinoid and TGF-β Families: Crosstalk in Development, Neoplasia, Immunity, and Tissue Repair. **Semin. Nephrol.** *32*, 287–294. https://doi.org/10.1016/j.semnephrol.2012.04.008.

173. Kim, S.A., Kang, J.H., Cho, I., Bae, S.W., and Hong, K.J. (2001). Cell-type specific regulation of thrombospondin-1 expression and its promoter activity by regulatory agents. **Exp. Mol. Med.** *33*, 117–123. https://doi.org/10.1038/emm.2001.21.

174. Discher, D.E., Janmey, P., and Wang, Y.L. (2005). Tissue cells feel and respond to the stiffness of their substrate. **Science.** *310*, 1139–1143. https://doi.org/10.1126/science.1116995.

175. Kureel, S.K., Mogha, P., Khadpekar, A., Kumar, V., Joshi, R., Das, S., Bellare, J., and

Majumder, A. (2019). Soft substrate maintains proliferative and adipogenic differentiation potential of human mesenchymal stem cells on long-term expansion by delaying senescence. **Biol. Open** *8*. https://doi.org/10.1242/bio.039453.

176. Gresham, R.C.H., Filler, A.C., Fok, S.W., Czachor, M., Schmier, N., Pearson, C., Bahney, C., and Leach, J.K. (2024). Compliant substrates mitigate the senescence associated phenotype of stress induced mesenchymal stromal cells. **J. Biomed. Mater. Res. - Part A** *112*, 770–780. https://doi.org/10.1002/jbm.a.37657.

177. Starich, B., Yang, F., Tanrioven, D., Kung, H.-C., Baek, J., Nair, P.R., Kamat, P., Macaluso, N., Eoh, J., Han, K.S., et al. (2024). Substrate stiffness modulates the emergence and magnitude of senescence phenotypes. **bioRxiv**, 2024.02.06.579151.

178. Fisher, G.J., Shao, Y., He, T., Qin, Z., Perry, D., Voorhees, J.J., and Quan, T. (2016). Reduction of fibroblast size/mechanical force down-regulates TGF-β type II receptor: implications for human skin aging. **Aging Cell** *15*, 67–76. https://doi.org/10.1111/acel.12410.

179. Stirling, D.R., Swain-Bowden, M.J., Lucas, A.M., Carpenter, A.E., Cimini, B.A., and Goodman, A. (2021). CellProfiler 4: improvements in speed, utility and usability. **BMC Bioinformatics** *22*, 1–11. https://doi.org/10.1186/s12859-021-04344-9.

180. Schindelin, J., Arganda-Carreras, I., Frise, E., Kaynig, V., Longair, M., Pietzsch, T., Preibisch, S., Rueden, C., Saalfeld, S., Schmid, B., et al. (2012). Fiji: an open-source platform for biological-image analysis. **Nat. Methods** *9*, 676–682. https://doi.org/10.1038/nmeth.2019.

181. Williams, T., and Kelley, C. Gnuplot homepage, http://www.gnuplot.info/.

182. Krämer, A., Green, J., Pollard, J.J., and Tugendreich, S. (2014). Causal analysis approaches in Ingenuity Pathway Analysis. **Bioinformatics** *30*, 523–530. https://doi.org/10.1093/bioinformatics/btt703.

183. Di Tommaso, P., Chatzou, M., Floden, E.W., Barja, P.P., Palumbo, E., and Notredame, C. (2017). Nextflow enables reproducible computational workflows. **Nat. Biotechnol**. *35*, 316–319. https://doi.org/10.1038/nbt.3820.

184. Ewels, P.A., Peltzer, A., Fillinger, S., Patel, H., Alneberg, J., Wilm, A., Garcia, M.U., Di Tommaso, P., and Nahnsen, S. (2020). The nf-core framework for community-curated bioinformatics pipelines. **Nat. Biotechnol.** 38, 276–278. https://doi.org/10.1038/s41587-020-0439-x.

185. Kim, D., Paggi, J.M., Park, C., Bennett, C., and Salzberg, S.L. (2019). Graph-based genome alignment and genotyping with HISAT2 and HISAT-genotype. **Nat. Biotechnol.** *37*, 907–915. https://doi.org/10.1038/s41587-019-0201-4.

186. Danecek, P., Bonfield, J.K., Liddle, J., Marshall, J., Ohan, V., Pollard, M.O., Whitwham, A., Keane, T., McCarthy, S.A., Davies, R.M., et al. (2021). Twelve years of SAMtools and BCFtools. **Gigascience** *10*. https://doi.org/10.1093/gigascience/giab008.

187. Liao, Y., Smyth, G.K., and Shi, W. (2014). featureCounts: an efficient general purpose program for assigning sequence reads to genomic features. **Bioinformatics** *30*, 923–930. https://doi.org/10.1093/bioinformatics/btt656.

188. Quinlan, A.R., and Hall, I.M. (2010). BEDTools: a flexible suite of utilities for comparing genomic features. **Bioinformatics** *26*, 841–842. https://doi.org/10.1093/bioinformatics/btq033.

189. Wu, T., Hu, E., Xu, S., Chen, M., Guo, P., Dai, Z., Feng, T., Zhou, L., Tang, W., Zhan, L., et al. (2021). clusterProfiler 4.0: A universal enrichment tool for interpreting omics data. **Innov. (Cambridge)** *2*, 100141. https://doi.org/10.1016/j.xinn.2021.100141.

190. Love, M.I., Huber, W., and Anders, S. (2014). Moderated estimation of fold change and dispersion for RNA-seq data with DESeq2. **Genome Biol.** *15*, 550. https://doi.org/10.1186/s13059-014-0550-8.

191. Yu, G., Wang, L.G., and He, Q.Y. (2015). ChIP seeker: An R/Bioconductor package for ChIP peak annotation, comparison and visualization. **Bioinformatics** *31*, 2382–2383. https://doi.org/10.1093/bioinformatics/btv145.

192. Hubert, M., Rousseeuw, P.J., and Vanden Branden, K. (2005). ROBPCA: A new approach to robust principal component analysis. **Technometrics** *47*, 64–79. https://doi.org/10.1198/004017004000000563.